The Thesis Committee for Justin Daniel Gorhum
Certifies that this is the approved version of the following thesis:

Development of a Pneumatic Infrasound Generator

APPROVED BY

SUPERVISING COMMITTEE:

Co-Supervisors:

Mark F. Hamilton

Thomas G. Muir

Development of a Pneumatic Infrasound Generator

by

Justin Daniel Gorhum, B.S.A.S.E.

Thesis

Presented to the Faculty of the Graduate School of

The University of Texas at Austin

in Partial Fulfillment

of the Requirements

for the Degree of

Master of Science in Engineering

The University of Texas at Austin

May 2014

Dedication

The following thesis is dedicated to the family of the author, who provided constant support, motivation, and love, especially his mother and father, Cheryl and Beauford, brother, Jeffrey, and future wife, Amy.

Acknowledgments

Development of a Pneumatic Infrasound Generator

Justin Daniel Gorhum, M.S.E.

The University of Texas at Austin, 2014

Co-Supervisor: Mark F. Hamilton

Co-Supervisor: Thomas G. Muir

This thesis details the experimental development of a pneumatic infrasound generator, the purpose of which is for calibration, testing, and research. The source was an assembly of an air reservoir, a motor, and a rotor/stator pair, in the context of a siren. A rotating ball valve acted as the rotor/stator and modulated the compressed air from the reservoir as it vented into the atmosphere. The ball valve cross sectional area as a function of time varied as a triangular waveform, which in practice caused the infrasonic waveforms to be effectively sinusoidal. This thesis opens with a brief motivation for the creation of the source, in addition to previously developed infrasound generators and an overview of wind noise. The apparatus construction is then described. A theory is developed that describes the acoustic radiation from the infrasound generator as the superposition of a monopole and a dipole. Flow visualization, propagation, frequency response, reservoir volume, directivity, and jet velocity experimental setups and results are described next. The outcomes of the research are subsequently discussed, including a brief overview of a scaled up model of the infrasound generator.

Table of Contents

List of Figures

xiv

Chapter 1

Introduction

1.1 Motivation

An experimental model of an infrasound generator was designed, built, and tested in order to validate a "ball valve siren" concept for the generation of tonal, low frequency sound. There is a need for such a generator to be used for the calibration of infrasound sensors, performing infrasound tests in the atmosphere, infrasound event monitoring, and for general infrasonic research.

The inclusion of infrasound monitoring as one of the verification methods of the Comprehensive Nuclear-Test-Ban Treaty (CTBT) has created new and widespread research into atmospheric infrasound [1]. Moreover, a global network of infrasound receiver arrays has been under construction and is currently being used to monitor infrasound events on a world wide scale. An overview of the development of these stations in the United States is discussed by Bass et al. [2]. The events that are detected using these receiver arrays include both natural and manmade infrasound. Natural sources of infrasound include, but are not limited to, microbaroms, earthquakes, volcanic eruptions, tornados, convective storms, and meteors. Manmade infrasound sources include ordinance disposal, rocket launches, aircraft, and nuclear explosions, as well as structural events such as large scale accidents and monitoring of oscillations due to bridge defects. Current in situ methods of infrasound sensor calibration use comparison

calibration and longtime averaging of the ambient infrasound noise [3]. Long term noise averaging from natural sources, such as microbaroms, uses a persistent but weak signal, and is made difficult by long testing time periods. Recording the infrasound from controlled ordinance disposal and is done for research and test purposes. Ordinance disposal provides strong signals from a known location at a specified date and time, but happen infrequently and produce impulsive signals, which become predominantly infrasonic with long travel times through the upper atmosphere.

A recently explored source of natural infrasound comes from biology. Animal infrasound is currently a rich topic of research in the field of animal communication, especially in large mammals. Giraffe necks, for example, can be part of a Helmholtz resonator to generate acoustic waves on the order of tens of hertz and used in communication [4]. Likewise elephants have been found to generate frequencies between 14 and 24 hertz for long range communication [5]. A controllable infrasound generator would be useful for research in this field too, as well as a wide variety of other fields. There is therefore a need for an infrasound source which can produce repeatable and frequency controlled signals of desired wave types. This source must also be portable, so it can be taken to different locations for research purposes. Frequencies of interest range from a few tenths of a Hz to around 5 Hz for CTBT applications, and a few Hz to around 20 Hz for biological and structural event monitoring (see comment at end of bibliography).

Infrasound signals are difficult to generate using traditional means of transduction. Sources that operate on the principal of resonances, such as speakers,

horns, etc. scale in size proportional to the wavelength of the signal. Therefore, as frequencies are lowered and the wavelength of the signal increases, resonant transducers must increase in size. For the infrasound frequency range, the size to which electroacoustic speakers scale is prohibitively large. There have been novel ideas for the generation of infrasound, namely rotary fans and loudspeaker arrays. Rotary fans, which generator infrasound by using a fan with pitching blades to blow air in and out of a back volume have been limited by the size of the back volume as well as structural failure of the fan blades. Moreover, the signal strength of the rotary fan is too low below 4 Hz. Loudspeaker arrays are also limited in their frequency response, as they are designed only to operate down to a frequency of 8 Hz. These sources are discussed and referenced below.

The concept of our model source was chosen in order to be portable and unrestricted by resonance dependence. The concept selected was that of a siren, which passes pressurized air through orifices which open and close in order to modulate the airstream into the desired waveform [6]. The orifices are traditionally oriented on the outside of a disc that is rotated by a motor and shaft. This rotating disc operates as part of a rotor/stator pair, where the stator remains stationary. When the rotor and stator are aligned, the orifice is fully open, and when the pair is not aligned, the orifice is fully closed. Typical sirens may operate anywhere from a few hundred hertz to a few kilohertz. The frequency range, rather than being limited by resonance, is limited by the operation of the driving motor. Therefore, it is feasible that a siren could operate at any frequency as long as the motor could drive the shaft and sufficient air could escape from the orifice.

However, at low frequencies, the disc design becomes impractical due to its susceptibility to air leaks at high pressures.

Typically, the orifices of sirens are small (~1 mm radius) and the pressures of operation are low (~5 psi) [7-9]. However, in order to increase the air flow into the atmosphere and create sustained and detectable infrasound signals, the orifice size was increased (~10 mm radius) and the operation pressure was increased (~130 psi). These standards were met by using a rotating ball valve in line with an air reservoir, and letting the ball valve act as the rotor, and its housing act as the stator. The ball valve was linked to a motor and rotated at half the desired frequency, as the ball valve opens fully twice per rotation. Moreover, the open cross-sectional area as a function of time of a rotating ball valve is a triangular waveform, rich in odd harmonics. However, the 3rd harmonic is 18 dB lower than the fundamental frequency so the signal is very close to a sinusoidal signal. This compact and durable "ball valve siren" served as the design for the infrasound generator model study, which will be scaled up to build a full size research grade infrasound generator.

1.2 Previously Developed Infrasound Generators

While there is currently not a standard infrasound generator used in calibration, there have been various attempts to engineer an infrasound generator. The first of these we will discuss was not designed to be used for infrasound sensor calibration, and actually fits the more general description of a low frequency and high intensity sound source. This source, dubbed the "Mother of All Speakers" (MOAS), was developed by

4

The National Center for Physical Acoustics at The University of Mississippi and operates over a frequency range from 8 hertz to hundreds of hertz [10]. While its design intentions and operational purposes are different from our own, it will be enlightening to briefly discuss their method of generating low frequency sound. Another source to be discussed is an array of subwoofer speakers that were designed to calibrate infrasound sources down to a frequency of 8 Hz [11]. Finally, a rotary fan source that was developed in order to calibrate infrasound sensors will be described [12,13]. As their motivation is very similar to ours, an examination of their techniques is interesting.

The MOAS designed by NCPA was designed to be a portable low frequency sound source that utilized a pneumatic loudspeaker coupled to an acoustic horn [10]. The pneumatic speaker made use of a commercially available air-stream modulator (WAS-3000™ developed by the Wylie Laboratories) to control the time series of the compressed air flow, and thus govern the output signal. Two horn options were available to attach to the pneumatic speaker: a 10 Hz exponential horn, 56 feet long, and a 25 Hz horn, 21.7 feet long, which telescoped and were assembled in the field on the bed of a tractor trailer. This system was able to produce acoustic pressure levels of 140 dB re 20 µPa 1 m above 30 Hz. The source was also portable, being mounted on a semi-trailer, with an extendable bed. The system exhibited directivity and a roll off in sound pressure level with decreasing frequency. The pneumatic speaker concept is appealing, as it allows for a larger amount of air to be displaced when compared to a traditional speaker. However, the requirement for a horn coupling becomes problematic at infrasonic frequencies. The length and area of the horn will continue to scale upward as frequency is

5

decreased. The system will soon become much too large to be feasible if the designed frequency of operation is below 10 Hz. This however, was not the designed intent of the MOAS, and as our objectives and requirements are different, we sought an alternative method to generate infrasound.

Walker, et al., utilized a speaker array of 18″ subwoofers and an output generated by M-sequences as a proposed method to calibrate infrasound sensors in situ [11]. The arrays were oriented in three different fashions: an angled square, flat square, and line array. Using the speaker array, they were able to ensonify an MB2000 infrasound sensor, a traditional Bruel and Kjaer™ microphone, and an optical fiber infrasound sensor, all of which are discussed in Ref. 11. While the speaker array provided adequate signal-to-noise to be detected by the infrasound sensors, the lowest frequency of reliable detection the array could provide was 8 Hz. Furthermore, operating the speakers below their roll off frequency (~20 Hz) greatly diminished the speaker pressure output. The power required to drive the speakers would also prove to be a limitation, if higher sound pressure levels were desired. Due to the resonant nature of speaker operation, producing a calibration quality signal far below speaker resonance will be impractical for a portable infrasound source.

A novel infrasound generator characterized as a rotary fan speaker was developed and is discussed in Parks and Robertson, and Parks, Garces, and Thigpen [12,13]. Their concept was to use a fan with variable pitch blades modulated at the infrasound frequency and coupled to a back volume. Infrasound was radiated into the front air medium. The first back volume used was a small room with compliant walls and ceiling. Portable

adaptations fixed the rotary fan speaker into the back of a towed trailer and used its interior space as the operating back volume which was probably compliant as well. The authors and developers theorized that by increasing the particle velocity of the acoustic wave, they have changed the radiation characteristics of the low frequency sound produced. Namely, they have transitioned from typical low frequency mass loading, which is characterized by poor radiation, to fluid-displacement controlled radiation, typically associated with more efficient, high frequency radiation, such as that occurring in jets. While the rotary fan speaker was able to generate detectable infrasound over long distances, it was unable to generate detectable signals below 5 Hz. The operation (frequency response, source strength, etc.) also seems to depend on the size of the back volume provided, which will be limited by the necessity of having a portable system.

1.3 Wind Noise

The presence of wind noise can be very problematic for the detection of infrasound. Even wind at a modest velocity (4-5 m/s) can obscure or mask infrasound signals. Furthermore, ambient infrasound noise from wind tends to increase at decreasing frequencies, making it more difficult to detect lower frequency signals. There are a number of sources for this wind noise, and a number of approaches have been made to reduce it. Overviews of wind noise and wind noise abatement techniques are discussed below. The discussion follows from the monograph on wind noise by K. T. Walker and M. A. H. Hedlin [14] found in the treatise on atmospheric infrasound by Le Pichon et al. [15]. Bowman et al. report the power spectral density of ambient noise in the infrasound

band over a number of different locations, seasons, and times of day [16], and his data are commonly used in infrasound sensor calculations.

Wind is driven primarily by the differences in atmospheric pressure over a given region. Moreover, atmospheric turbulence, closely related to the wind, is caused by convective and mechanical forces. The turbulence that arises from convective forces is produced by thermal instability which drives atmospheric mixing. The turbulence that arises from mechanical forces is caused by interference of the wind with ground topography. The convective turbulence, being generated by thermal gradients, is governed largely by the diurnal meteorological cycle. This leads to a large difference in the wind noise between day and night. Specifically, during the day, an unstable planetary boundary layer (PBL) is developed due to a nonlinear temperature profile as a function of altitude. Solar heating on the earth's surface causes a negative temperature gradient from the surface to the top of the PBL. However, above the PBL, the temperature of the atmosphere begins to rise, resulting in a positive temperature gradient. This instability increases the presence of mechanical and convective turbulence, driving winds and increasing wind noise. At night however, the planet surface is colder than the rest of the PBL and the temperature increases linearly with altitude through, and above, the PBL. This temperature profile results in a stable atmosphere, thus reducing the wind presence and wind noise. Therefore, it is advantageous to take infrasound measurements at night. There are exceptions however, as storms and weather fronts can also drive winds.

There are various types of wind noise recognized, each contributing to the ambient noise level through the wind characteristics and its interactions with its

8

surroundings. The first type of wind noise is the most obvious, and is the wind noise associated with the fluctuation of wind velocity. The next type of wind noise is caused by the physical wind/sensor interaction. When the wind strikes the microphone, a stagnation pressure is applied to the diaphragm. This stagnation pressure can cause noise, especially when the wind velocity is fluctuating, as the stagnation pressure will then fluctuate. The third type of wind noise is generated by the interaction between individual turbules. A turbule can be described as a localized turbulent eddy. This type of noise is known as turbulence-turbulence interaction. The interaction of the turbules causes a pressure disturbance that can be detected by the infrasound sensor. The interaction between turbules and the vertical gradient of the average horizontal wind velocity along the ground also serves as a source of wind noise. This interaction, which can be detected by infrasound sensors and microphones, is more commonly identified as the turbulence-mean shear interaction. Finally, acoustic energy can be generated by the wind itself and contribute to noise. This is most commonly manifested when the wind interacts with topographical features, such as mountains or oceans, or becomes very violent in motion, as is the case in storm systems. A more detailed review of these wind noise sources, including mathematical descriptions of the spectra and turbulence, is provided by Walker and Hedlin [14].

In order to decrease the likelihood of wind noise masking an infrasound signal, a number of wind noise reduction techniques have been employed. Many of these techniques recognize the fact that high frequency wind noise is largely incoherent over short ranges, while the infrasound noise is coherent over large ranges. Thus, by

integrating the incoming signal over ranges large enough so that the turbulence noise is incoherent, wind noise is reduced while the desired infrasound signal is preserved. The simplest example of this is implemented in the Daniels filter, which is a linear series of connected pipes with various diameters, each of which has an inlet into which noise may enter [17]. As sound enters the pipe and travels down the filter, additional sound is added at the next inlet. This process is continued down the pipe until the signal arrives at the sensing instrument. As the wind noise is incoherent and the infrasound wave is coherent over the length scale, the infrasound is preserved and the wind noise is filtered out. However, the Daniels filter response is dependent on the direction of sound propagation. For example, if the wave is traveling co-linearly along the filter from the beginning, towards the instrument, the system response is flat across all frequencies. However, if the infrasound signal approaches the broadside of the filter, the frequency response will be a directivity function described by line array theory.

To overcome the limitations of the Daniels filter, rosette pipe filters were developed [18]. Rosette pipe filters are a series of four or more equally spaced solid pipes that meet at a primary summing manifold where a sensor is located. At the end of each solid pipe is a secondary summing manifold, from which numerous other pipes extend. At the end of these secondary manifold pipes are inlets which let in infrasound. A drawing of the rosette filter, reproduced from Alcoverro and Pichon is shown in Fig. 1.1 [18].
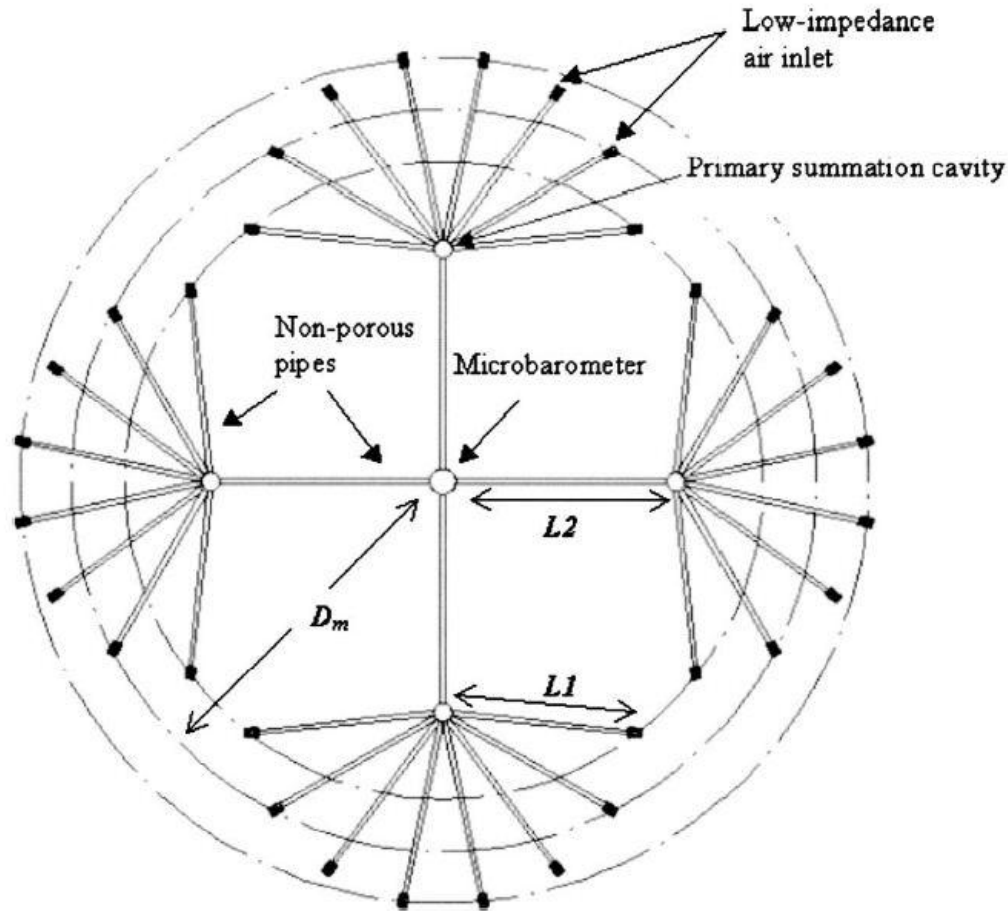
Figure 1.1: Standard rosette filter used at IMS array sites (Alcoverro and Le Pichon [18]).

In practice, the rosettes can be anywhere from 18 to 70 m across and have a variety of inlet numbers. The size of the rosette determines the frequency band of maximum noise reduction, with smaller rosettes attenuating wind noise at higher frequencies, and the larger rosettes attenuating at both high and low frequencies. The rosettes operate on the same idea as the Daniels filter: integrating over a large region to remove incoherent noise. However, the geometrical symmetry of the filter aims to produce a response that is independent of the incoming wave orientation and propagation

11

direction. However, the rosette pipes are susceptible to pipe resonances. To combat this problem, matched impedance capillary plugs can be installed in the pipes to reduce the resonance effect.

Another filter that relies on the spatial integration of the infrasound signal for noise reduction is the microporous hose filter, evolved at the NCPA and elsewhere. The microporous hose filter is essentially a commercial hose that has a porous outside lining that is designed to leak out water slowly, to be used in irrigation. These hoses can be attached to a manifold containing an infrasound sensor in a variety of configurations. For example, a single porous hose can be attached to a sensor similar to the Daniels filter, or multiple hoses can branch out from the sensor manifold similar to a rosette pipe configuration. This filter operates on the same principle as the previous filters; the incoming infrasound signal exerts a pressure through the hose, which is added up over a range longer than the coherence range of the wind noise. The total integrated signal at the manifold retains the infrasound signal but the wind noise has been reduced. An example of our own microporous wind filter connecting to a sensor manifold is shown in Fig. 1.2.

Figure 1.2: Microporous wind filter with microphone in sealed box.

A novel signal integration filter that has been proposed to reduce wind noise is the Optical Fiber Infrasound Sensor (OFIS) [19]. This sensor integrates the pressure incident on the OFIS, as opposed to integrating the pressure passing through ports or pores, along the path in order to filter out wind noise and obtain the infrasound signal. The sensor operates on the principle of interferometry, where the deformation of the OFIS can be sensed by two lasers beamed through optical fibers that travel down the length of the sensor. The OFIS is usually buried in a straight line a small depth under the surface and covered by a porous material that does not attenuate the infrasound, such as gravel. The directivity for the linear oriented OFIS becomes omnidirectional when the infrasonic wavelength is about four times larger than the length of the deployed sensor.

Yet another wind reduction technique does not use spatial acoustic integration, but rather utilizes a dense array of robust sensors with digital signal processing. The dense array of sensors has been dubbed a "distributed sensor" and the infrasound signal can be extracted from the wind noise during post processing. Alternatively, algorithms could be designed so that signal processing occurs during real time and only one set of data is output by the distributed sensor. The sensor elements that make up the dense array have the potential to be cheap, durable, and broadband [20].

Other wind reduction techniques seek to reduce wind noise by isolating the infrasound sensor from the wind. One of these techniques uses porous media to filter out noise from wind and wind generated turbules [21]. This technique is implemented by burying the sensor in a medium that isolates the sensor from the atmosphere but allows infrasound to pass through, such as gravel or sand. While there has been some testing of this technique, much more work needs to be done and it is not widely implemented.

Another technique for isolating sensors from wind noise is to set up wind barriers [22]. There are numerous types of wind barriers, such as fences, set up around rosettes and sensors that are covered with screens and serrations that serve to reduce the generation of turbulence caused by air flow over the barrier. For our experiments, we primarily used a padded cushion that was supported by a central metal frame and rested over our microphone, forming a smooth, dome-like structure. This cushion served to isolate the microphone from higher frequency wind noise while also gradually redirecting the wind over the sensor, preventing the development of turbulence that would occur if

the wind was flowing over sharp edges. A picture of this setup can be seen in Figs. 1.3 and 1.4.

Figure 1.3: Wind cushion filter over microphone.

Figure 1.4: Microphone in foam support under metal frame (blue) to support wind cushion (red).

A typical daytime noise power spectral density (PSD) for our research location is shown below in Fig. 1.5. Shown is the noise PSD in a 1 Hz bandwidth for three different wind reduction setups, as well as the low-noise and medium-noise curve fits from Bowman [15]. The blue curve corresponds to a microphone mounted in an open box with no wind filter. As expected, its PSD is the highest. The green curve corresponds to a microphone with a cushion wind filter (Fig. 1.3), and the red line corresponds to the sealed box-perforated hose (Fig. 1.2) wind filter. While the PSD of the cushion filter and microporous hose/sealed box filter overlap in certain frequency bands, the sealed box-perforated hose is generally better, and it is expected that the cushion noise PSD will increase with higher wind levels, lending further utility to the microporous hose/sealed box method of wind reduction. The Bowman measurement curve fits are shown with the red dashed line for medium-noise and the blue dashed line for low-noise. These

16

measurements were made at IMS stations using rosette pipe filters or porous hoses [15]. This figure makes it clear that the noise in our flat, urban, research environment is by no means ideal. However, these noise levels are typical for day time measurements. For the experiments and measurements described later in this thesis, the cushion wind filter was used, as we had not yet developed the microporous hose/sealed box wind filter of Fig. 1.2. Despite the high wind noise levels at the time of measurements at this site, it will be shown that clear infrasound signals generated by the infrasound source, to be described below, were able to be measured above the noise levels.
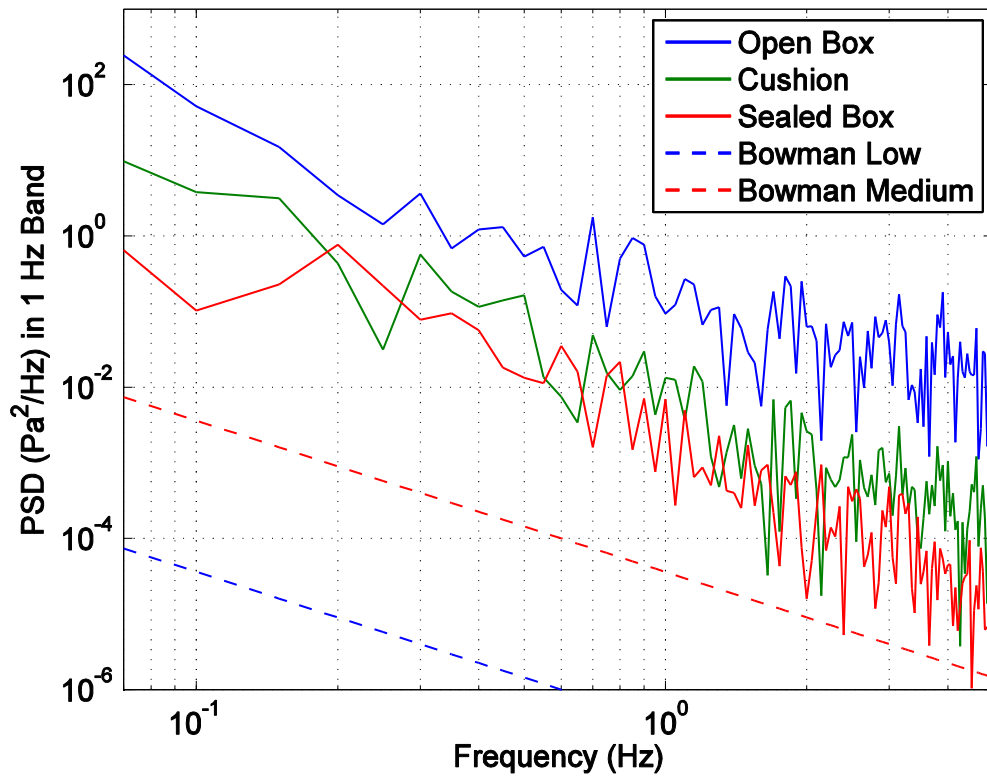
Figure 1.5: Measured Power Spectral Density for research location.

Chapter 2

Apparatus

The model study infrasound generator consists of a ball valve siren mounted on a tripod. The ball valve siren consists of three major components: a reservoir, a motor, and a rotor/stator pair. Additionally, a Pitot tube is used to measure the air flow velocity at the siren exit, and microphones are used to measure the output acoustic pressure generated.

2.1 Reservoir and Compressor

The reservoir of the siren supplies the air that is modulated to produce acoustic signals. The reservoir is filled with air generated by a shop-type electric air compressor, rated at a maximum capacity of 150 psi. The operation time of the siren is determined by the volume of air stored in the reservoir, while the signal amplitude is governed by the reservoir pressure. As a general trend, it was observed that expanding the size of the reservoir and keeping the pressure constant, resulted in a signal with an increased number of cycles and no observable increase in signal amplitude. Moreover, the reservoir depletes over time causing the storage pressure, and thus the signal amplitude, to eventually decrease.

The reservoir used for the siren consists of 5 SCUBA tanks. Each SCUBA tank possesses an unpressurized volume of 0.0133 m^3, leading to a total reservoir volume of 0.0665 m^3 for 5 SCUBA tanks. Pressurized to a pressure of 130 psig, the total air mass is approximately 0.77 kg. At the output of each of the tanks is a cutoff ball valve that can be

used to open or close the tank. This allows the effective size of the reservoir to be modified by opening or closing the valves connected to the individual tanks. The outlet of each tank also has a dial pressure gauge threaded into a port in the ball valve, so that the stored pressure in each of the tanks can be monitored. Unless otherwise noted, all acoustic measurements were made using a reservoir consisting of all 5 tanks.

2.2 Motor

The motor provides the means by which the rotor/stator component of the siren is rotated. The motor used is a commercial, DC powered, trolling motor, developed for the sports fishing trade, which is linked to the stem of the ball valve. The motor provides a constant angular frequency to the ball valve at half the desired infrasound frequency, due to the ball valve opening twice per revolution. The motor is then attached to a planetary gear reducer with a 1:7 reduction ratio that allows for the ball valve to be steadily rotated at lower frequencies. The system possesses an upper frequency limit of 8 Hz.

2.3 Rotor/Stator

The rotor/stator pair comprises of ball valve constructed for nominal ¾″ NPT (National Pipe Thread) fittings, with the handle removed, to allow for 360° rotation when linked to the motor. The true inner diameter of the ball valve (and associated piping) is larger, with an inside diameter of 0.83″, or 2.1 cm. The inner ball, which serves to modulate the air flow, as it turns, serves as the rotor in the siren while the housing serves as the stator. A cutaway illustration of a ball valve is shown in Fig. 2.1 [23].
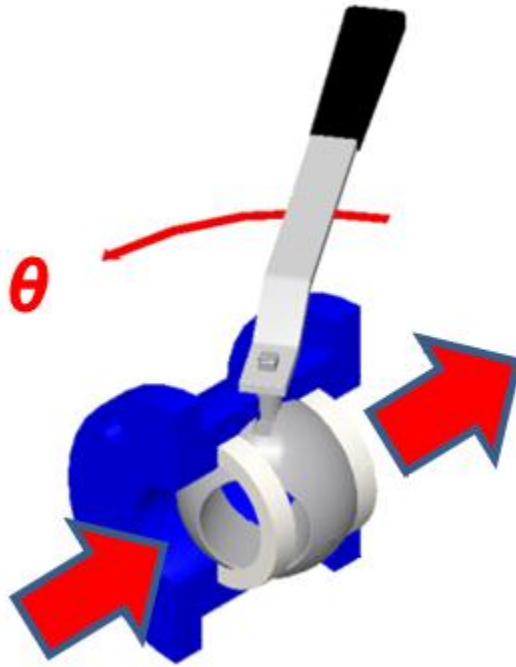
Figure 2.1: Ball valve depiction.

When the ball valve is closed, there is no leakage of air out of the siren, as there can be with disk sirens. A SolidWorks™ software study was done [24] which showed that the open cross-sectional area as a function of time of a rotating ball valve is a triangular waveform. Therefore, the rotor modulates the air to produce a sinusoidal like waveform. The ball valve is connected in series to the reservoir by various lengths of ¾″ NPT nipples, hoses, and manifolds.

2.4 Assembly and Deployment

The infrasound generator was assembled and deployed outdoors, on a grassy plain, where all acoustic measurements were made. The reservoir tanks were positioned on a wooden stand and plumbed in parallel with a common input manifold. Separately,

the motor linked to the rotating ball valve was secured to an aluminum support mounted atop a wooden tripod. Upstream of the ball valve control nipples and shutoff valves were attached, as well as a 'T' cutoff valve, which connected to the air compressor, to provide for safe and convenient operation. Downstream of the ball valve, a short nipple was attached, serving as an exit port and also as a mount for a Pitot tube to measure the exit airflow. Finally, a high pressure, ¾″ NPT gas hose was used to connect the reservoir manifold to the compressed air input nipple, upstream of the ball valve. With this configuration, air flow to the ball valve could be cut off and the air from the compressor turned on, allowing the reservoir tanks to be filled. Once full, the compressor input was shut off and the cut off valve restricting air flow to the rotating ball valve was opened. This allowed for air to flow out of the reservoir, be modulated by the ball valve, and expand into the atmosphere, creating infrasound. The jet nozzle of the infrasound generator can be oriented vertically, with the exit jet firing perpendicular to the ground, or horizontally, with the exit jet firing parallel to the ground. A schematic and photograph of the assembly with the vertical nozzle configuration can be seen in Figs. 2.2 and 2.3, respectively. A schematic and photograph of the assembly with the horizontal jet nozzle configuration can be seen in Figs. 2.4 and 2.5, respectively. It should be noted that Fig. 2.3 shows the microphones on a stand, while all measurements and data shown in this thesis were made with the microphone on the ground, covered by a cushion as shown in Figs. 1.3 and 1.4. Additionally, Fig. 2.3 shows an aluminum Venturi device at the nozzle exit with embedded pressure sensors. This research tool was later removed in favor of a Pitot tube setup up, and all measurements were made with the nozzle exiting modulated

21

compressed air into the atmosphere with a Pitot tube inserted into the flow, as seen in Figs. 2.6 and 2.7.
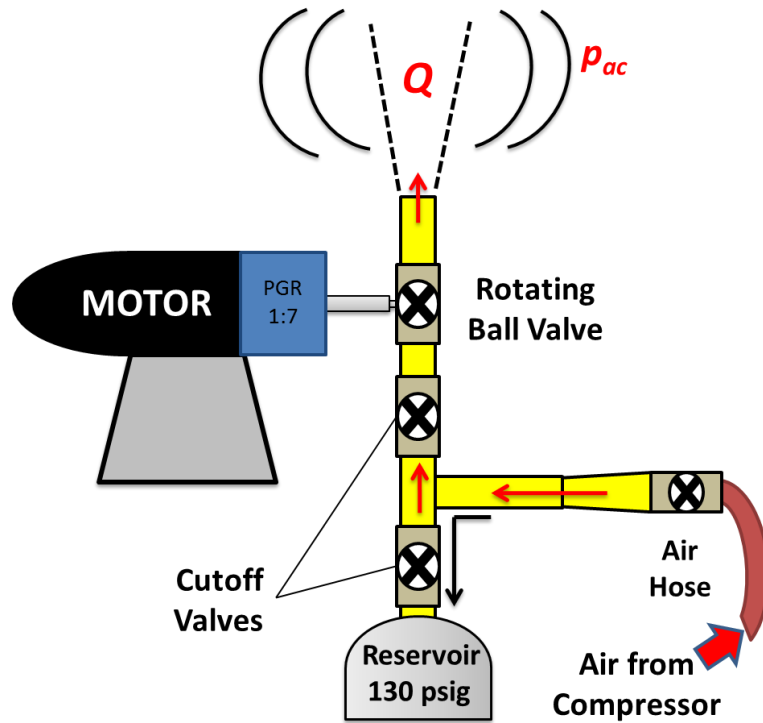
Figure 2.2: Schematic of system with vertical jet nozzle configuration.
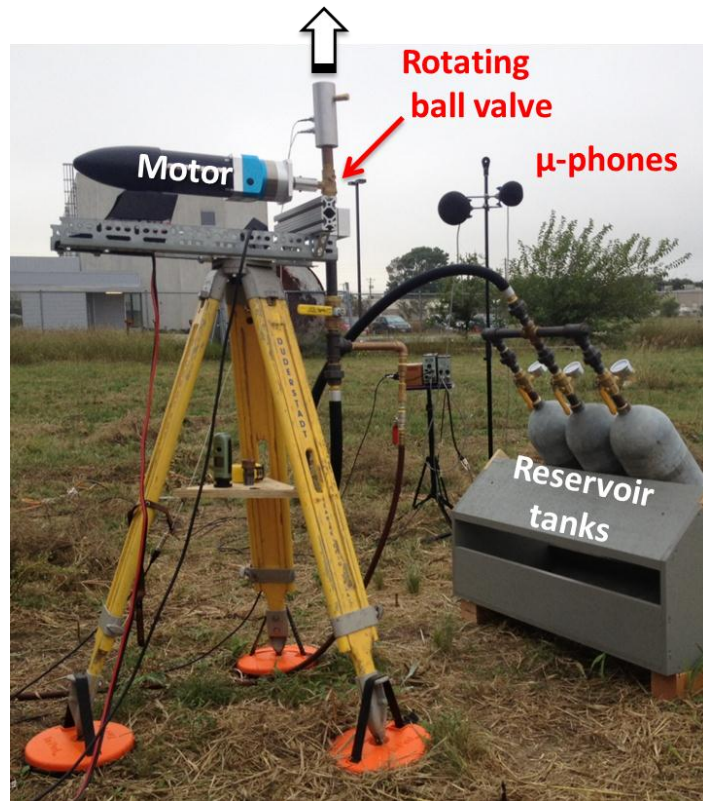
Figure 2.3: Photograph of system with vertical jet nozzle configuration.
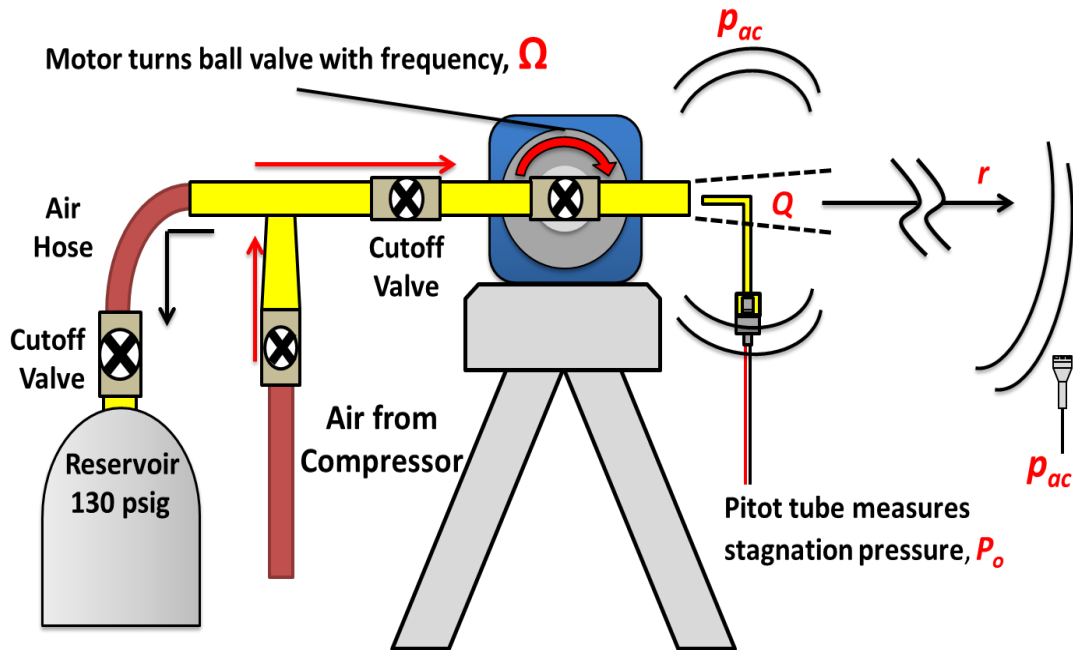
Figure 2.4: Schematic of system with horizontal jet nozzle configuration.

Figure 2.5: Photograph of system with horizontal jet nozzle configuration.

2.5 Pitot Tube

A Pitot tube was used to perform aerodynamic velocity measurements. As the modulated air exits from the siren orifice, a turbulent compressible jet is formed. The Pitot tube, which measures stagnation pressure, can be used to calculate the velocity of the exiting jet. Use of the Pitot tube was restricted to the jet axis. The Pitot tube used was traditional in its design, consisting solely of a small pipe bent at a right angle and exposed to the flow. The non-exposed end of the pipe was connected to a pressure transducer that

measured the stagnation pressure. The exposed end was rounded to reduce flow disturbances and increase the area of the stagnation point. The diameter of the hole immersed in the flow measured 2 mm. The Pitot tube setup can be seen in Figs. 2.6 and 2.7. The presence (Fig. 2.6) or absence (Fig. 2.7) of an exit pipe nipple in the aluminum collar fitting made no noticeable difference in either our acoustic or Pitot tube measurements.

Figure 2.6: Pitot tube setup at outlet with short nipple in aluminum collar.

Figure 2.7: Pitot tube setup at outlet of aluminum collar.

Chapter 3

Theory

In one of his many seminal works on aerodynamically generated sound, Lighthill briefly mentions the siren as the simplest of aeroacoustic sources: a monopole source due to a modulated volume velocity [25]. Similarly, Theobald postulated that a siren with multiple output ports in a disk configuration could be modeled as a ring source, or with the addition of a cone, as a baffled piston [26]. However, the sirens of Lighthill's time, and even our own time, operate on vastly different conditions than the source discussed. The main differences are the operating pressure of the device and the frequency range. While the reservoir pressure of a typical high frequency, high amplitude siren is on the order of 136 kPa (5 psig) [7,8], the air in our reservoir is charged to a pressure on the order of 998 kPa (130 psig). The single port design of the present infrasound source also varies greatly from typical audio band sirens. Small, multiport sirens dominate the design space of modern sirens, and the cross-sectional area designs come in a variety of shapes in order to increase efficiency or change waveform shape and harmonics [7]. For an infrasound siren however, maximizing the airflow while also creating a controlled sine wave are the primary goals. Therefore, a large bore opening, in this case a nominal ¾″ ball valve, was used to increase volume velocity. Moreover, the cross sectional area of a ball valve rotating with time is triangular [24], which for our experiment, can be well approximated by a sinusoidal air modulation.

Whereas Lighthill proposed the siren as a monopole source, the extreme operating conditions of the infrasound source introduce a number of complexities into the problem. For example, the transient formation of a supersonic compressible jet from the exit of the ball valve introduces turbulent noise sources, derived from shed vortices or eddies, which can greatly complicate the physics of the problem. However, these effects are minor in the present frequency range of interest and were ignored. Moreover, the jet was modeled as a single point acoustic source, in contrast to a distributed line array. Characterizing this source was further complicated by the frequency regime and the difficulty of making far field measurements. The main noise component obscuring the infrasound measurements was the presence of wind noise, which was especially high in our testing frequency band. Further, the longest wavelengths were on the order of 100s of meters, so all the measurements were made within a wavelength.

The following section seeks to characterize the infrasound generator source by first evaluating the aerodynamics of the system. Second, a theoretical acoustic model will be proposed in order to explain observed measurements.

3.1 Aerodynamics

3.1.1 Compressible Flow

For acoustics, the medium into which sound is being projected must always be compressible, as it is the fluctuation of the density that allows the acoustic wave to propagate. However, the most fundamental flows of fluid mechanics and aerodynamics are often assumed to be incompressible, i.e., possessing a constant density. There is a

special class of flows in fluid mechanics where the density must be treated as variable. These flows, referred to as compressible flows, travel at velocities fast enough to change their fluid densities. This fluid compression is what causes shock waves to form as the flow is accelerated past the speed of sound. The following physical description of the pipe exit jet follows Chapters 7 and 8 of John D. Anderson's textbook on aerodynamics [27].

A fundamental non-dimensionalized parameter for high speed fluid flows is the Mach number. The Mach number is defined as the ratio of the flow velocity divided by the local speed of sound in the fluid

$$M = \frac{u}{c} \quad , \tag{1}$$

where M is the Mach number, u is the flow velocity, and c is the speed of sound. For our purposes, fluid flows can be considered incompressible for Mach numbers of $M \leq 0.3$, and will be treated as compressible for flow Mach numbers of $M > 0.3$. Of course, supersonic flows will correspond to flows with Mach numbers of $M > 1$.

While changes in density must be accounted for in such flows, it is often a necessary assumption to neglect changes in the entropy of the fluid. This assumption is referred to as the isentropic assumption. For a free jet, it can be further assumed that no work is being done on the fluid and no heat is being added. Under these conditions, it may be stated that the flow is adiabatic. For any fluid, its state can be expressed by its pressure, density, or temperature. In an isentropic flow, the thermodynamic states of the fluid are conveniently related by the following expression:

$$\frac{P_2}{P_1} = \left(\frac{\rho_2}{\rho_1}\right)^{\gamma} = \left(\frac{T_2}{T_1}\right)^{\frac{\gamma}{\gamma-1}} \qquad , \qquad (2)$$

where P is the pressure of the fluid, ρ is the density, T is the temperature, and γ is the ratio of specific heats. The ratio of specific heats, γ, has a value of 1.4 in air at standard temperature and pressure, and is defined as

$$\gamma = \frac{c_p}{c_v} \qquad , \qquad (3)$$

where c_p is the specific heat of air at constant pressure and c_v is the specific heat of air at constant volume. For the gas currently under treatment, the specific heats will have constant values. Thus, we can refer to this gas as being a calorically perfect gas. As the system was operated at moderate temperatures and pressures, the isentropic assumption was made. In order to define the speed of sound c, it is convenient to define a further thermodynamic property of the gas. The specific gas constant, R, is defined for a calorically perfect gas as

$$R = c_p - c_v \qquad , \qquad (4)$$

Using the specific gas constant R, the equation of state at a point in a perfect gas can be expressed by the perfect gas law

$$P = \rho R T \qquad , \qquad (5)$$

It is now pertinent and necessary to define the speed of sound in the fluid. For an isentropic fluid, the square of the speed of a sound wave traveling through the fluid may be physically expressed as the rate of change of the pressure, P, with respect to the density, ρ, at constant entropy, s. Formally, this is relation is expressed as

$$c^2 = \left(\frac{\partial P}{\partial \rho}\right)_s \quad , \tag{6}$$

By evaluating the above partial derivative for an isentropic fluid, the speed of sound for a calorically perfect, isentropic gas, is obtained, resulting in the following formulas

$$c = \sqrt{\frac{\gamma P}{\rho}} = \sqrt{\gamma RT} \quad , \tag{7}$$

where both formulas in Equation (7) are related by the perfect gas law.

In order for the fluid from a reservoir to be accelerated to supersonic velocities, it must be passed through a converging-diverging nozzle, a device that will be qualitatively described presently. If air is flowing through a pipe that exits into the atmosphere, a converging-diverging nozzle corresponds to the section of pipe where the cross-sectional area is gradually reduced along the length of the pipe (converging), and then gradually increased along the length of the pipe (diverging). The minimum cross-sectional area, or the area where the nozzle changes from converging to diverging, is referred to as the nozzle throat. By continuity, it is known that for subsonic flows, reducing the cross-sectional area of a pipe causes the flow velocity to increase, while increasing the cross-sectional area of the pipe causes the flow velocity to decrease. Conversely, for supersonic flows, reducing the cross-sectional area causes the flow velocity to decrease, while increasing cross-sectional area causes the flow velocity to increase. Thus, to increase the speed of a subsonic flow, the cross-sectional area must be reduced along the path of the flow, and to increase the speed of a supersonic flow, the area must be increased along the path of the flow. This is the key to supersonic nozzle design. If at the throat of the nozzle,

the subsonic flow in the converging section has been accelerated to sonic velocity (M=1), then the flow will continue to accelerate to supersonic velocities as it passes through the diverging section. We do not have a designed nozzle present in our system; however, because the open ball valve area is less than that of the pipe at most times during operation, the constriction and expansion along the contours of the ball valve effectively act as a nozzle. This allows for the jet exiting our ball valve to achieve supersonic velocities.

An important concept in compressible flow is the stagnation point. The stagnation point is conceptually a point in the flow where the fluid has been brought to rest isentropically. The state properties of the fluid at the stagnation point will be labeled with a subscript o, e.g. P_o is the stagnation pressure. Properties without the o will be referred to as the static property of the flow. The stagnation properties at any point in the flow can be described as what the quantity would be if the flow was isentropically decelerated to a stop. This is realized when making measurements with a Pitot tube, the type of which has previously been described. The bluff end of the Pitot tube, which faces the flow, ideally becomes a stagnation point in the flow. The opening at the bluff end allows for the measurement of the stagnation pressure, P_o. The stagnation pressure can be related to the Mach number by first stating the energy equation for steady, adiabatic, and inviscid flow as

$$c_p T_o = c_p T + \frac{u^2}{2} \quad .$$
(8)

Rearranging and substituting in γ for a calorically perfect gas, the following expression is found to be

32

$$\frac{T_o}{T} = 1 + \frac{\gamma - 1}{2} M^2 \quad . \tag{9}$$

When combined with the isentropic relationship for pressure and solving for the Mach number, an expression for the flow Mach number is found. This is expressed in terms of the ratio of stagnation to static pressure is given as

$$M^2 = \frac{2}{\gamma - 1} \left[\left(\frac{P_o}{P}\right)^{\frac{\gamma - 1}{\gamma}} - 1 \right] \quad , \tag{10}$$

With the stagnation pressure, P_o, measured by the Pitot tube, and knowledge of the static pressure, P, the Mach number for the jet can be calculated. The static pressure is usually assumed to be the local atmospheric pressure and jet nozzles are usually designed to operate at this condition. As we have not designed a nozzle, and only have an effective nozzle created by the rotating ball valve, we will assume that our static pressure is equal to atmospheric pressure.

A difficulty arises when performing measurements with a Pitot tube for a supersonic flow. When the flow is supersonic, a bow shock forms over the Pitot tube, introducing the need for a further correction to the Mach number calculations. This is illustrated in Fig. 3.1. This figure demonstrates that in the presence of a bow shock, the stagnation pressure measured is not that of the jet flow. Instead, it is that of the flow after the shock. However, there is a relationship between the measured stagnation pressure and the free stream flow conditions. This relationship is known as the Rayleigh Pitot tube formula and is expressed as

$$\frac{P_{o,2}}{P_1} = \left(\frac{(\gamma+1)^2 M_1{}^2}{4\gamma M_1{}^2 - 2(\gamma-1)}\right)^{\frac{\gamma}{\gamma-1}} \frac{1 - \gamma + 2\gamma M_1{}^2}{\gamma+1} \quad , \quad (11)$$

where P_{o2} is the measured stagnation pressure, P_1 is the static pressure, and M_1 is the

Mach number of the jet. This formula is an implicit function of the Mach number, M_1,

and must be solved. However, it is often tabulated in textbooks that cover the subject of

compressible fluid flow.
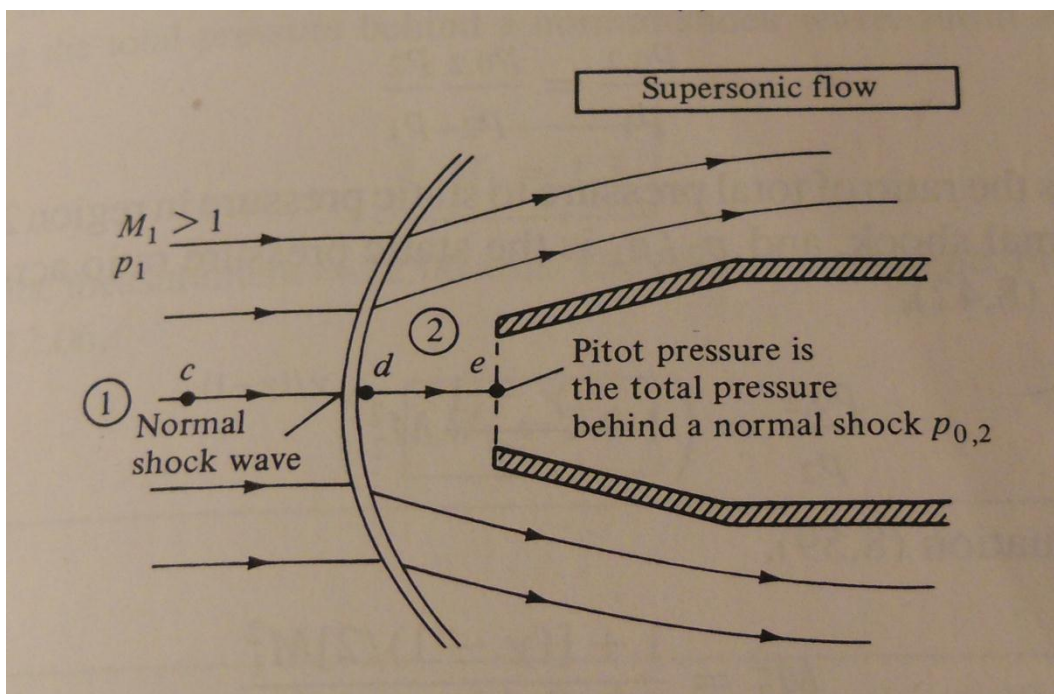
Figure 3.1: Flow conditions for a Pitot tube in supersonic flow (from Anderson [27] "Fundamentals of Aerodynamics" ©, McGraw-Hill (2007)).

3.1.2 Centerline Velocity Decay of Compressible Jet

For the present analysis of the turbulent jet output, it was also desired to model

and predict the decay of the jet's centerline velocity. While turbulence is characterized by

rapid, and sometimes seemingly random, fluctuations in the local flow velocity, the

34

velocity of the bulk flow is fairly consistent. In other words, when referring to the jet velocity, we will refer to the mean velocity of the flow, ignoring any small turbulent fluctuations.

In order to predict the centerline velocity decay, it is necessary to understand the general structure of a turbulent jet. A simplified diagram illustrating the different regions of jet flow can be seen in Fig. 3.2. For a turbulent jet, there is a potential core with length x_c that follows the jet orifice. In this region, the centerline velocity is equal to the jet exit velocity. This potential core region collapses at x_c, where the flow becomes fully turbulent.
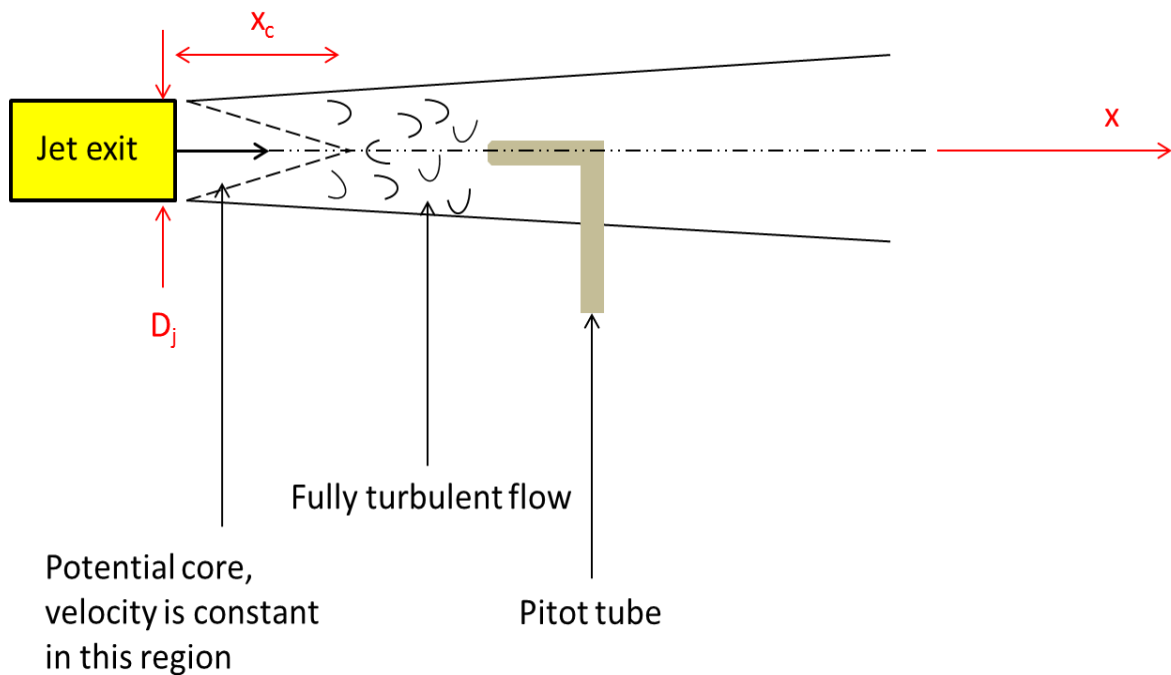
Figure 3.2: Turbulent flow geometry.

It has been shown experimentally and theoretically that the centerline velocity decay of the fully developed turbulent flow for an incompressible free jet is proportional

35

to x^{-1} [28]. However, when the flow is compressible, and moreover supersonic, the matter becomes more complicated. By utilizing numerous experiments that measured the centerline velocity decay of fully turbulent jets, Witze [29] was able to create an empirical formula that collapsed all of the jet velocity decay data to a single curve. The empirical relation is as follows:

$$\frac{u(x)}{u_j} = 1 - \exp\left(\frac{-1}{2\kappa\left(\frac{x}{D_j}\right)\rho'^{0.5} - X_c}\right) \quad , \qquad (12)$$

where, $u(x)$ is the velocity along the jet centerline axis, u_j is the velocity at the jet exit, κ is an empirical constant based on the Mach number, D_j is the diameter of the jet, x is the jet centerline coordinate, ρ' is the ambient density normalized by the jet exit density, and X_c is an empirical constant equal to 0.7 and should not be confused with the potential core length, x_c. The constant κ is given by the equation

$$\kappa = 0.063(M^2 - 1)^{-0.15} \quad , \qquad (13)$$

There is a further correction that can be made when the flow transitions from supersonic to subsonic, which replaces the coordinate x with an adjusted coordinate starting at what is called the sonic point (i.e. the distance x where $M=1$). However, this adjustment is minor and will not be considered here, as all the measurements made were close to the exit of the jet exit, and most were supersonic. While this empirical formula matches the centerline velocity data well, it tends to overestimate the potential core length x_c. Therefore, an updated version of this (Witze's) model will be used. Lau provided a rearrangement of Equation (12), which he refers to as the Kleinstein-Witze formula [30],

with an empirical constant that can be adjusted for the individual case. Lau also introduced a more accurate expression for the potential core length [31].

$$\frac{u(x)}{u_j} = 1 - \exp\left(\frac{\alpha}{1 - \frac{x}{x_c}}\right) \quad , \quad (14)$$

where α is the new empirical constant that depends on the jet conditions, and x_c is given by

$$x_c = D_j(4.2 + 1.1M^2) \quad , \quad (15)$$

Using Equation (14) and α=1.2, the model matches the measured data of this experiment, for a centerline velocity decay very well. Therefore, Lau's empirical formula was adopted for characterizing the spatial evolution of the jet. It should be noted that as x becomes large, and thus the flow slows down and becomes incompressible, the expression approaches the x^{-1} proportionality theorized for an incompressible free jet [28]. Yet again, a correction can be applied to the empirical model for when the flow becomes subsonic. However, the two results are almost indistinguishable from each other and very few measurements were made in the subsonic region. Thus, it is sufficient to characterize the jet by Equation (14) without incorporating the subsonic correction.

3.2 Acoustics

The modulated airflow that is vented into the atmosphere serves as a source of acoustic radiation. The primary generators of the acoustic radiation field are the time varying mass addition into the atmosphere, and the time varying reaction force exhibited on the atmosphere by the jet outlet. Thus, we seek to model the acoustic pressure field

using the superposition of a point source and a point force. The derivation of the following monopole and dipole radiation equations are similar to those found in Chapter 10 of Blackstock's textbook on physical acoustics [32] for laminar flow. However, modifications are made to accommodate the physics of the infrasound source.

3.2.1 The Monopole Source

For laminar flow, time varying mass flow into the atmosphere can be characterized as a simple source, or monopole, radiator. It can be shown that the pressure amplitude for such a radiator is given as

$$p_m = \frac{\rho \dot{Q}}{4\pi r} \qquad , \qquad (16)$$

where, p_m is the peak acoustic pressure amplitude from the monopole, ρ is the ambient fluid density, r is the range from the source to receiver, and $\dot{Q}$ is the volume acceleration. This is given in Equation (D-7) in Chapter 10 of Blackstock [32]. This canonical simple source radiator is envisioned as a sphere injecting and withdrawing fluid time harmonically. Similarly, when venting compressed air into the atmosphere, the volume acceleration for the time harmonic infrasound source is

$$\dot{Q} = j\omega Q \qquad , \qquad (17)$$

where j is the imaginary unit ($\sqrt{-1}$), ω is the angular frequency of the wave, and Q is the volume velocity. Substituting Equation (17) into Equation (18) yields

$$p_m = \frac{j\omega\rho Q}{4\pi r} \qquad , \qquad (18)$$

This equation is equal to that of the canonical spherical simple source. For the system under study, the angular velocity, ω, and the volume velocity, Q, can be expressed as known parameters in Equations (19) and (20) below as

$$\omega = 2\pi f \qquad , \qquad (19)$$

$$Q = u_j A \qquad , \qquad (20)$$

where f is the frequency of the infrasound wave, u_j is the peak jet velocity at the nozzle outlet, and A is the area of the jet outlet. Q is also known as the source strength of the monopole. From the equations, it can be seen that in this model, the time varying volume velocity flow generates monopole radiation.

The geometry of the monopole radiator is shown in Fig. 3.3. The simple source, S, is at a height, h, above the ground, which is modeled as a rigid half space.
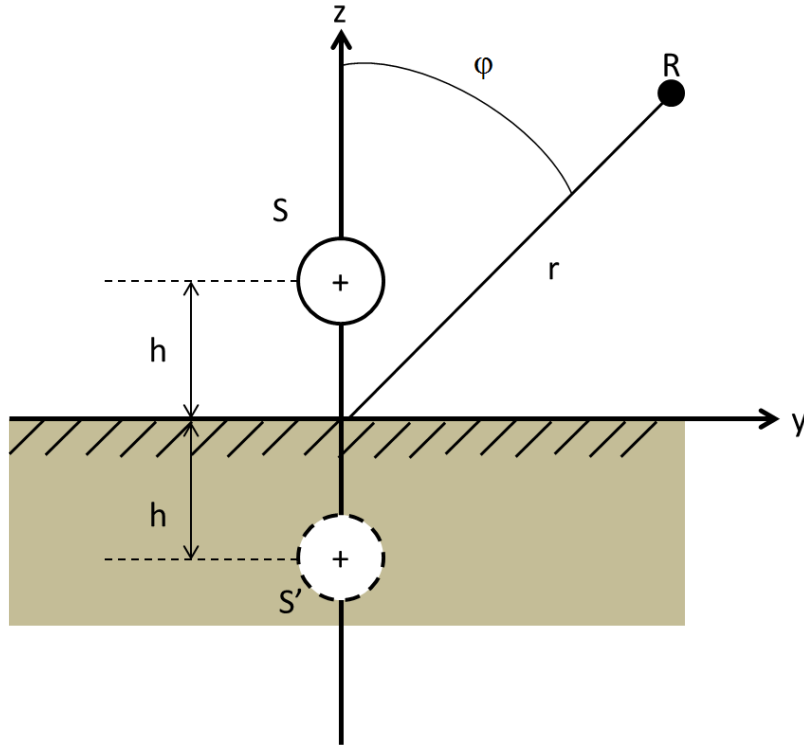
Figure 3.3: Monopole above a rigid half space.

Since the simple source is close to the ground, we can replace the rigid surface by placing an image source of matching phase at a distance of h below the y-axis. The image source in Fig. 3.3 is denoted by a dashed circle and is labeled S′. The total pressure at a receiver, R, is the sum of the source and its image, and is given as

$$p = \frac{j\omega\rho Q}{4\pi} e^{j(\omega t - kr)} \left(\frac{e^{jkh\cos\varphi}}{r - h\cos\varphi} + \frac{e^{-jkh\cos\varphi}}{r + h\cos\varphi} \right) \quad , \qquad (21)$$

where Equation (21) is a constant term and propagation term multiplied by the addition of the source and image source spreading terms. The height of the source above the ground was h=1.6 m for the vertical orientation and h=1.3 m in the horizontal orientation. For most of the performed experiments, the microphone was at a distance or angle such that

r>>*h*cosφ. Therefore, *h*cosφ can be neglected in the denominator of the spreading terms, but will be retained in the exponential phase factors. The resulting expression is:

$$p = \frac{j\omega\rho Q}{4\pi r} e^{j(\omega t - kr)}(e^{jkh\cos\varphi} + e^{-jkh\cos\varphi}) \qquad ,$$

$$= \frac{j\omega\rho Q}{4\pi r} e^{j(\omega t - kr)} 2\cos(jkh\cos\varphi) \qquad , \qquad (22)$$

It is shown that spherical spreading has been recovered. Moreover, because *kh*<<1, the cosine term is approximately equal to unity. The wavenumber *k* values for the experiment ranged from *k*=0.02 m^{-1} to *k*=0.14 m^{-1}. Therefore, the pressure amplitude for the monopole component of the infrasound generator is:

$$p_m = \frac{j\omega\rho Q}{2\pi r} \qquad . \qquad (23)$$

Note that this expression is equivalent to that of a free space monopole. This equation will be used to model the acoustic pressures generated by the infrasound source mass addition.

3.2.2 The Dipole Source

The time varying thrust force of the jet outlet on the fluid also generates an acoustic radiation field. This stems from Newton's third law; if a force is applied onto an object, an equal and opposite force will be applied by the object. The jet exerts a thrust force onto the infrasound generator plumbing and hardware. Since the infrasound generator is fixed in space, the plumbing and hardware exert a back reaction onto the fluid and the surrounding medium. The described thrust reaction force, which is time

41

harmonic, results in acoustic dipole radiation. In his 1961 Bakerian Lecture on sound generated aerodynamically [25], Lighthill summarized:

> With solid objects in air, on the other hand, the dipole strength is usually closely equal to the force with which the body acts on the air, that is, equal and opposite to the aerodynamic force on the body…

Moreover, in a personal communication with P.J. Westervelt, it was expressed that the output jet momentum would create an acoustic dipole [33].

This thrust force was observed during the experiments. When the system was first operated, and compressed air was vented into the atmosphere, there was a strong back reaction force that caused the tripod, upon which the jet nozzle was mounted, to tip over. This thrust force is also fundamental to rocket propulsion, where venting of a high velocity gas, and the subsequent reaction force, propels the mass of the rocket. In order to prevent the tripod from tipping over, weights were attached to the two front legs of the tripod. Fixing the tripod caused a reaction force to be exhibited back against the force of the flow and onto the surrounding medium. This force is time harmonic, being related to the time varying flow, and can be expressed as

$$F = P_o(t)A \qquad , \qquad (24)$$

where, $P_o(t)$ is approximated as the time varying stagnation pressure measured by the Pitot tube, and A is the projected area upon which the stagnation pressure acts. The projected area will be the area perpendicular to the fluid pathway, which is equal to the area of the jet outlet. Essentially, the surface integral of the force is taken over the area of the exiting air flow. This concept is similar to that discussed by Lamb [33], where a plane

wave scattered off a sphere exhibits monopole radiation, as expected, and dipole radiation as well, due to the reaction force that keeps that sphere fixed in space.

It is known that a time varying point force in a fluid exhibits dipole radiation. Equation (4-4.5) in Pierce's book on acoustics [35] describes the radiation from a point force as

$$p_d = \frac{1}{4\pi} \mathbf{e_r} \cdot \left(\frac{1}{r} + \frac{1}{c} \frac{\partial}{\partial t} \right) \frac{\mathbf{F}\left(t - \frac{r}{c} \right)}{r} \quad , \qquad (25)$$

where $\mathbf{F}$ is the force acting on the fluid and $\mathbf{e_r}$ is the unit vector in the propagation direction. Assuming a time harmonic force, we can evaluate the derivative, which leads us to the canonical dipole, which is a sphere translating back and forth in a fluid, along the axis. Therefore, Equation (25) results in

$$p_d = \frac{1 + jkr}{4\pi r^2} F \cos\theta \cos\varphi \quad , \qquad (26)$$

where θ is the azimuthal angle, φ is the polar angle, F is the peak force, and k is the wavenumber of the acoustic wave, defined in Equation (27), as

$$k = \frac{\omega}{c} \quad . \qquad (27)$$

The orientation of the dipole axis will change based on the orientation of the jet nozzle. The dipole axis will be perpendicular to the ground when the jet nozzle is oriented vertically and parallel to the ground when the jet nozzle is oriented horizontally. By switching between a vertical and horizontal jet nozzle configuration, the dipole axis is rotated 90°. The geometry of these configurations are shown in Figs. 3.4 and 3.5.

Fig. 3.4 shows the geometry for the vertically oriented jet nozzle. The dipole is denoted as D, placed some height h away from a rigid half space. The rigid interface can be removed and replaced with an image dipole, D′, when the dipole is close to the ground.
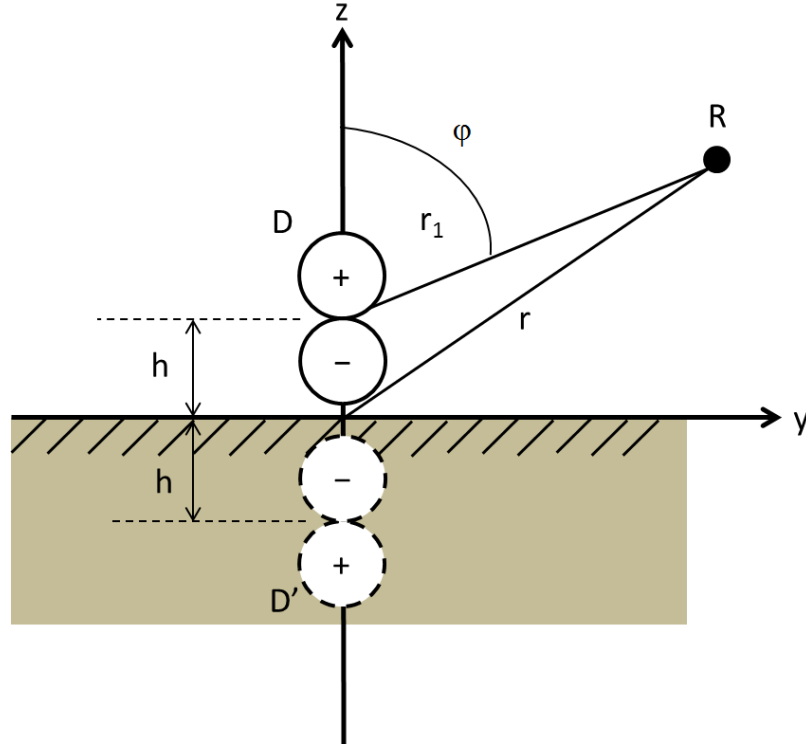
Figure 3.4: Vertical dipole above a rigid half space.

The total pressure at the receiver, R, is the addition of the pressure contributions from the dipole source and its image. This is expressed in the equation below as

$$p_d = \left\{ \left(\frac{1 + jk(r - h\cos\varphi)}{4\pi(r - h\cos\varphi)^2} \right) e^{jkh\cos\varphi} - \left(\frac{1 + jk(r + h\cos\varphi)}{4\pi(r + h\cos\varphi)^2} \right) e^{-jkh\cos\varphi} \right\} F\cos\theta\cos\varphi e^{j(\omega t - kr)}$$

$$, \qquad (28)$$

where the first (bracketed) part of Equation (28) is the propagation factor of the dipole and its image, and the second part is a scaling term determined by the source strength and

44

the receiver angle. The $h\cos\varphi$ terms that appear with the receiver distance r can be neglected if $r \gg h\cos\varphi$. This will be an appropriate approximation for all but the closest measurement ranges. The $h\cos\varphi$ terms in the exponentials will be retained, as they may have a strong impact on phase. This assumption yields

$$p_d = \left\{ e^{jkh\cos\varphi} - e^{-jkh\cos\varphi} \right\} \frac{1 + jkr}{4\pi r^2} F\cos\theta\cos\varphi e^{j(\omega t - kr)} \quad ,$$

$$= 2j\sin(kh\cos\varphi) \frac{1 + jkr}{4\pi r^2} F\cos\theta\cos\varphi e^{j(\omega t - kr)} \quad , \quad (29)$$

Due to the low frequency nature of the source addressed here and its proximity to the ground, it is true that $kh \ll 1$. Therefore, $\sin(kh\cos\varphi)$ is approximately equal to its angle, $kh\cos\varphi$. Substituting this into Equation (29) will result in the pressure amplitude for a vertical dipole above a rigid surface being:

$$p_d = (jkh\cos^2\varphi) \frac{1 + jkr}{2\pi r^2} F\cos\theta \quad , \quad (30)$$

This result is very similar to that found in Chapter 10, Equation (D-35), of Blackstock [32]. While Blackstock assumes far field from the beginning, so the r^{-2} dependence is removed, the presented theory retains the r^{-2} spreading dependence. It is observed that this source will die out quickly and will have longitudinal quadrupole directivity due to the $\cos^2\varphi$ factor.

An analogous approach can be taken for the horizontally oriented jet nozzle and dipole. The geometry for the horizontal dipole, D, above the rigid half space is shown in Fig. 3.5. Yet again, because the dipole is close to the ground, we can replace the rigid boundary with an image source D′.
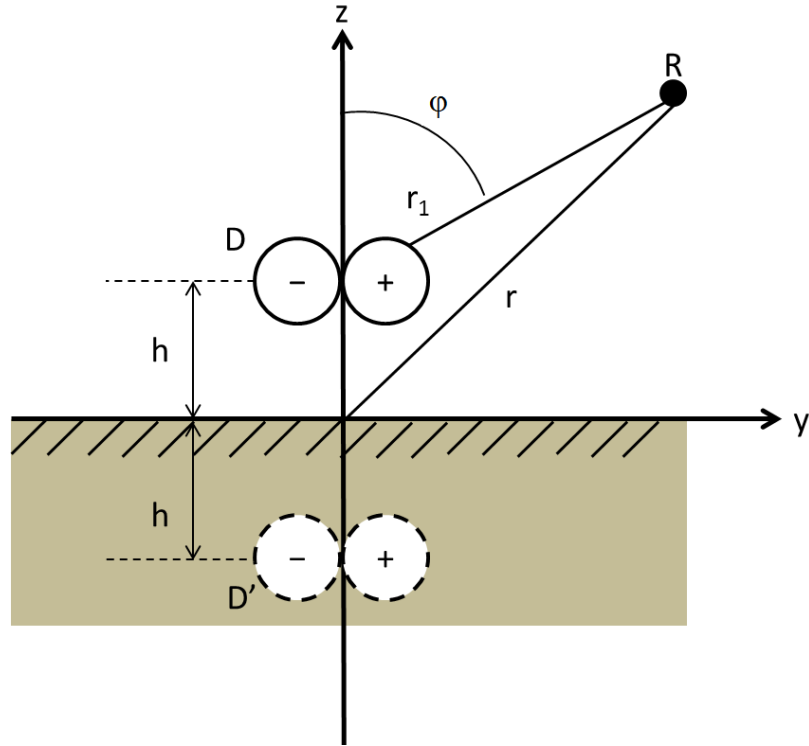
Figure 3.5: Horizontal dipole above a rigid half space.

By the same mathematical reasoning as for the vertical source, the total acoustic

pressure at the receiver, *R*, from the dipole and its image will become:

$$p_d = \left\{ \left(\frac{1 + jk(r - h\cos\varphi)}{4\pi(r - h\cos\varphi)^2} \right) e^{jkh\cos\varphi} + \left(\frac{1 + jk(r + h\cos\varphi)}{4\pi(r + h\cos\varphi)^2} \right) e^{-jkh\cos\varphi} \right\} F\cos\theta\sin\varphi e^{j(\omega t - kr)}$$

$$, \qquad (31)$$

Note in Equation (31) that the $\cos\varphi$ term in Equation (26) has been replaced with

$\sin\varphi$ as a result of rotating the dipole axis by 90°. Assuming, as before, that $r \gg h\cos\varphi$,

Equation (31) reduces to:

$$p_d = \left\{ e^{jkh\cos\varphi} + e^{-jkh\cos\varphi} \right\} \frac{1 + jkr}{4\pi r^2} F\cos\theta\sin\varphi e^{j(\omega t - kr)} \quad , \quad \text{which}$$

46

$$= 2\cos(kh\cos\varphi)\frac{1+jkr}{4\pi r^2}F\cos\theta\sin\varphi e^{j(\omega t-kr)} \qquad (32)$$

Finally, by assuming $kh\cos\varphi\ll 1$, $\cos(kh\cos\varphi)$ is approximated as 1. This results

in the pressure amplitude for a horizontal dipole above a rigid interface to be expressed

as:

$$p_d = \frac{1+jkr}{2\pi r^2}F\cos\theta\sin\varphi \qquad , \qquad (33)$$

The end result essentially doubles the pressure of the free field dipole described in

Equation 33, but with $\sin\varphi$ replacing $\cos\varphi$ after the 90$^{\text{o}}$ rotation of the dipole axis. This

equation is again analogous to Equation (D-32) in Blackstock [32], the main difference

being the retention of the r^{-2} spreading dependence.

3.2.3 The Total Sound Pressure Level

For the modulated compressed air source of this thesis, it is proposed that the total

acoustic pressure will be the sum of both the monopole radiation pressure and the dipole

radiation pressure. The total SPL will be used as the metric of comparison between the

measured data and the physical values predicted by theory. The total SPL is defined as:

$$SPL = 20\log_{10}\left(\frac{|p_m+p_d|}{p_{ref}\sqrt{2}}\right) \qquad , \qquad (34)$$

where p_{ref} is the reference pressure, equal to 20 µPa, p_m is the peak monopole pressure

amplitude (Equation 23), and p_d is the peak dipole pressure amplitude for the current jet

nozzle orientation (Equation 30 or Equation 33). For the two specific orientations of the

infrasound generator, the vertically oriented jet nozzle and the horizontally orientated jet

nozzle, the dipole axis will be rotated by 90°. The location of the microphone will make the polar angle, φ, near 90° for the vertical and horizontal jet nozzle cases. Physically, the dipole contribution will be near zero for the vertical jet orientation, except for at the nearest ranges. Conversely, the dipole contribution will not be diminished in the horizontal jet orientation. This will be further demonstrated in the results section.

While the monopole and dipole sources occur at different places, at the outlet of the jet nozzle and the back of the jet pipe, the sources add in phase and effectively act in the same location. This is because the separation between the two source locations, l, is very small when compared to the wavelength of the infrasound wave. In other words, because the waves being radiated are low frequency, they add in phase over the short distance of separation. Therefore, the proposed theoretical model for the infrasound generator is the superposition of a point source and a point force. This will be valid across our entire frequency range.

Chapter 4

Experimental Procedure

The model infrasound generator was set up in an outside field in the back of the Applied Research Laboratories main building, away from shops, sheds, and trees. All outdoor measurements were made during daylight working hours, with wind speeds typically in the 0 to 15 mph range. A small metal test shelter was located near the experiment and was used to house all electronic recording equipment including oscilloscopes, power supplies, amplifiers, and filters. The air compressor used to pressurize the reservoir was located near the experimental set up and refilled the air supply of the reservoir after each test. However, the compressor was never running or supplying air during the experiment, in order to prevent excess noise.

Two different configurations of the generator jet outlet were tested. First, tests were performed with the jet pointed vertically, perpendicular to the ground. The experiments were then repeated with it pointed horizontally, parallel to the ground. Beam pattern measurements were performed in this configuration to explore the source directivity.
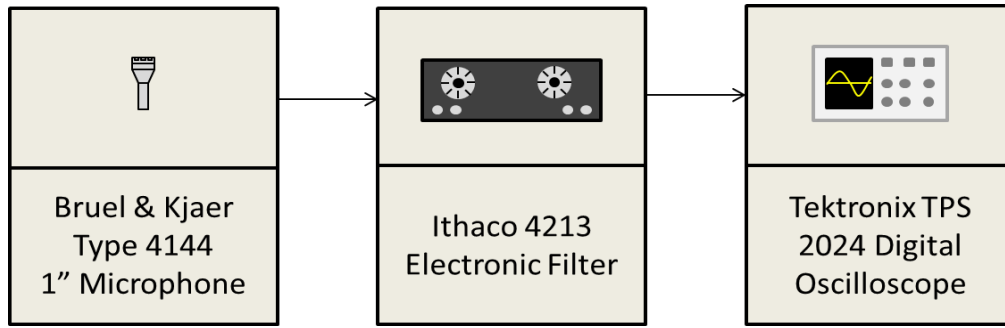
4.1 Data Acquisition

4.1.1 Instrumentation for Vertically Oriented Nozzle

Microphones were placed on the ground, oriented vertically, and padded cushions were placed over the microphones to reduce wind noise without attenuating the

infrasound (Figures 1.3 and 1.4 of Chapter 1). For the vertical orientation, two microphones were used to collect data. The microphones used were one Bruel and Kjaer (B&K)™ Type 4144 1″ microphone and one Bruel and Kjaer Type 4193-L-004 ½″ microphone. The Type 4144 microphone has a lower -3 dB point at 1.4 Hz while the Type 4193-L-004 is designed to have a flat response down to 0.07 Hz. Therefore, the 1″ microphone measurements were not as reliable at the lowest recorded frequencies as those made with the ½″ B&K microphone. The 1″ B&K microphone signal was passed through an Itahco™ 4213 Electronic band pass filter in order to reduce broadband ambient noise. The signal was then displayed on a Tektronix® TPL 2024 digital oscilloscope. The data was recorded to a compact flash disk for further analyzing. This flow of data is graphically displayed in Fig. 4.1. The data recorded with the ½″ B&K microphone followed a similar path. The measurements made with the ½″ B&K microphone passed through a Burr-Brown™ Model 100 AC decade amplifier before being filtered and then displayed on the oscilloscope. This data was also recorded to the compact flash disk. This data acquisition format is displayed in Fig. 4.2.

Fig. 4.3 shows the data acquisition for the aerodynamic stagnation pressure measurements. A Pitot tube was placed on the jet axis at the infrasound generator's outlet. The end of the Pitot tube outside of the flow was outfitted with a PCB Piezotronics Integrated Circuit-Piezoelectric (ICP®) Model 102A02 dynamic pressure sensor, detailed in Appendix C. This dynamic pressure sensor passed a voltage signal to the Tektronix digital oscilloscope, which was recorded to the compact flash disk.

Figure 4.1: Data acquisition for vertical jet pipe measurements using Bruel & Kjaer 1″ microphone.
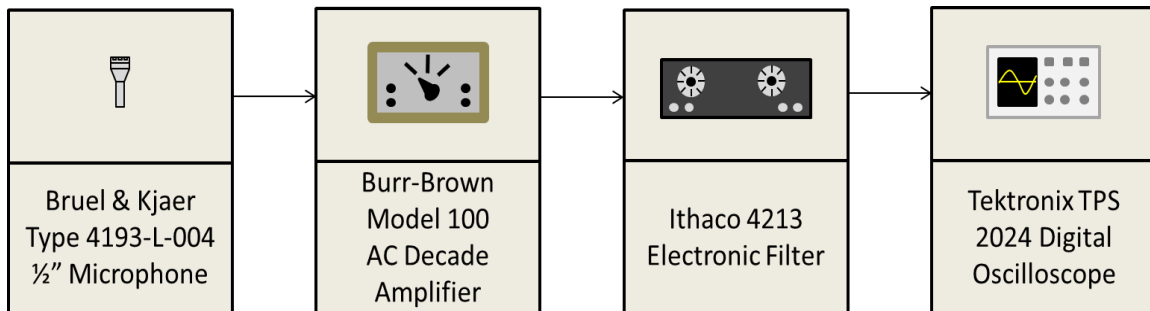
Figure 4.2: Data acquisition for vertical jet pipe measurements using Bruel & Kjaer ½″ microphone.
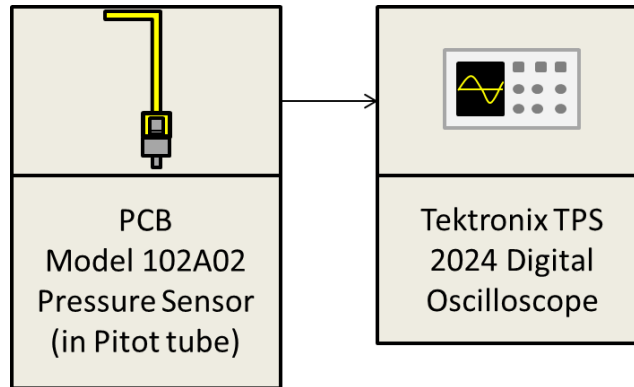
Figure 4.3: Pitot tube sensor for vertical jet pipe.

4.1.2 Instrumentation for Horizontally Oriented Nozzle

The acoustic measurements for the horizontal jet nozzle orientation were made with a single G.R.A.S.™ Type 40AZ ½″ microphone designed to operate between 0.5 Hz and 20 kHz. The frequency response of this microphone when paired with a G.R.A.S.

51

Type 26CG preamplifier is included in Appendix B. The data flow for the horizontal orientation are shown in Fig. 4.4. Measurements made by the ½″ G.R.A.S. microphone are amplified by the Burr-Brown amplifier before being filtered by the Ithaco Electronic filter and being displayed on an Agilent™ DSO-X 2004A digital oscilloscope. The data is then recorded from the oscilloscope to a USB flash drive for further analysis. For directivity measurements, two of these microphone setups are used, one for normalization and one for field measurements..

Fig. 4.5 shows the Pitot tube setup for the horizontally oriented nozzle. The Pitot tube was in the same geometric location as in the vertically oriented setup, but was now equipped with a Kavlico™ P255 pressure sensor, detailed in Appendix D. The Kavlico sensor provided the advantage of being able to maintain a steady-state pressure reading instead of discharging over a short period of time. The voltage was passed on to the Agilent oscilloscope and recorded to a USB flash drive.
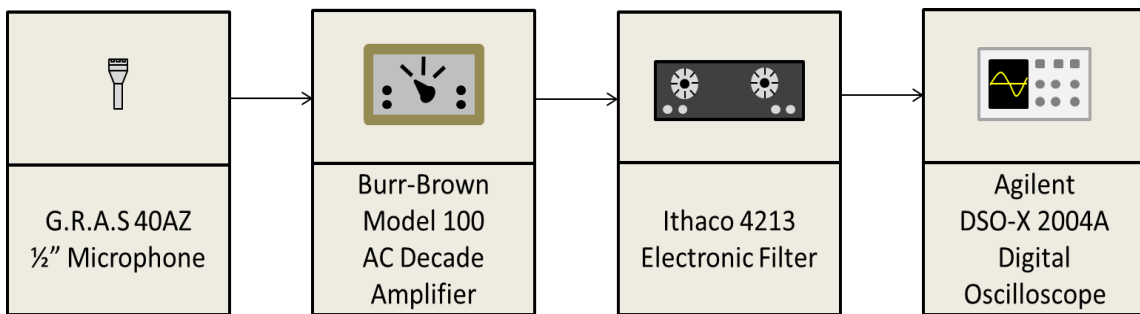
Figure 4.4: Data acquisition for horizontal jet pipe measurements using G.R.A.S. ½″ microphone.
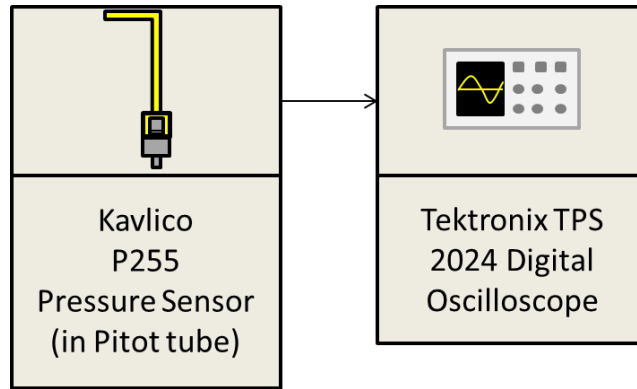
Figure 4.5: Pitot tube sensor for horizontal jet pipe.

The computer software programs MATLAB and Microsoft Excel were used heavily for the data reduction. Waveforms were recorded by the oscilloscopes and transferred to a desktop computer. Excel spreadsheets were made to tabulate the data for varying frequency, range, jet pipe orientation, etc. The waveforms were then plotted on MATLAB and the peak voltage amplitudes were recorded in the Excel spreadsheets. The voltages were then converted into acoustic pressures and sound pressure levels. MATLAB was used to plot the sound pressure levels, as well as generate theoretical curves for each experimental study.

4.2 Flow Visualization

A flow visualization experiment was performed in a dark and dry room. The moisture in the air collected by compressor, located outside, condensed when the compressed air was vented into the dry room. This allowed for the jet to be visualized in the form of cloud like puffs of water vapor. A high speed camera shooting at 600 frames per second was used to capture a video showing the growth and decay of a flow modulated at approximately 3.7 Hertz. A meter stick was attached to the jet stand with

white tape marking off every 10 centimeters. High intensity lights were used to help illuminate the flow for the video capture. This visualization was done with the nozzle exit oriented vertically.

4.3 Propagation

An experiment was performed to measure the propagation characteristics of the infrasound signal. A microphone was placed in the field at distances ranging from 2 m to 32 m. The microphone was moved progressively further out after each test for a range of frequencies. The test frequencies included 1.25 Hz, 2.5 Hz, 3.7 Hz, 5.4 Hz, and 8 Hz. This experiment was performed for both vertical and horizontal nozzle orientations. For the vertical nozzle, test ranges included 2 m, 4 m, and 8 m. For the horizontal nozzle, all measurements were made on axis and test ranges included 8 m, 16 m, 24 m, and 32 m.

4.4 Frequency Response

An experiment was performed to measure the frequency response of the system. A microphone was placed in the field at specified distance from the infrasound source. Signals of varying frequencies were then generated and measured. The frequency response covered a 2 octave band and included the following frequencies: 1.25 Hz, 2.5 Hz, 3.7 Hz, 5.4 Hz, and 8 Hz. The frequency response was recorded at various ranges from 2 m to 24 m. This experiment was performed for both vertical and horizontal nozzle orientations. For the horizontal nozzle orientation, the frequency response was measured

at ranges of 2 m, 4 m, and 8 m. For the vertical nozzle orientation, the frequency response was measured at 8 m, 16 m, and 24 m.

4.5 Reservoir Volume

An experiment was performed in order to determine the effect of reservoir volume on the infrasound source's acoustic output. During this experiment, the reservoir size was varied by opening and closing the shutoff valves in order to change the number of tanks in the reservoir. By preventing air storage in the tanks, the size of the reservoir could be controlled. The number of tanks used in the reservoir was varied from 1 to 3 tanks, resulting in the reservoir volume being changed from 0.0133 m^3 to 0.0399 m^3. After the reservoir was filled, the acoustic output was recorded at a range of 1 meter. The reservoir was then resized by opening the cut off valve to a tank and the test was repeated. The experiment was performed for reservoir volumes of 0.0133 m^3, 0.0266 m^3, and 0.0399 m^3. While the final reservoir included up to 5 tanks, 3 was the maximum number of tanks used in the reservoir volume test. This test was performed for the vertical nozzle orientation only.

4.6 Directivity

An experiment was performed in order to determine the directivity of the source. Only the directivity of the horizontal nozzle orientation was measured. The directivity experiment was performed in two stages. In the first stage, the directivity of a 90° quadrant was measured for a span of frequencies from 1.25 Hz to 8 Hz at a distance of 8

m. The second stage consisted of measuring the directivity for a full 360° circle at a fixed frequency of 8 Hz at ranges of 8 m and 16 m. For both stages, a microphone was held on axis at 8 m and was used for normalization. This allowed for any variances in source strength caused by inconsistencies in the system, i.e. reservoir pressure variations, to be eliminated from the measurements. Data was taken in 15° increments with the nozzle axis being the 0° point. For the 90° quadrant measurements, one G.R.A.S. 40AZ microphone was kept on axis for normalization, and a different G.R.A.S. 40AZ was moved around the arc. For the full 360° circle measurements, the B&K Type 4144 1″ microphone was held on axis at a range of 8 m for normalization, while G.R.A.S. 40AZ microphones were moved around the perimeter of the circle. A schematic of the full 360° experiment is shown in Fig. 4.6 below.
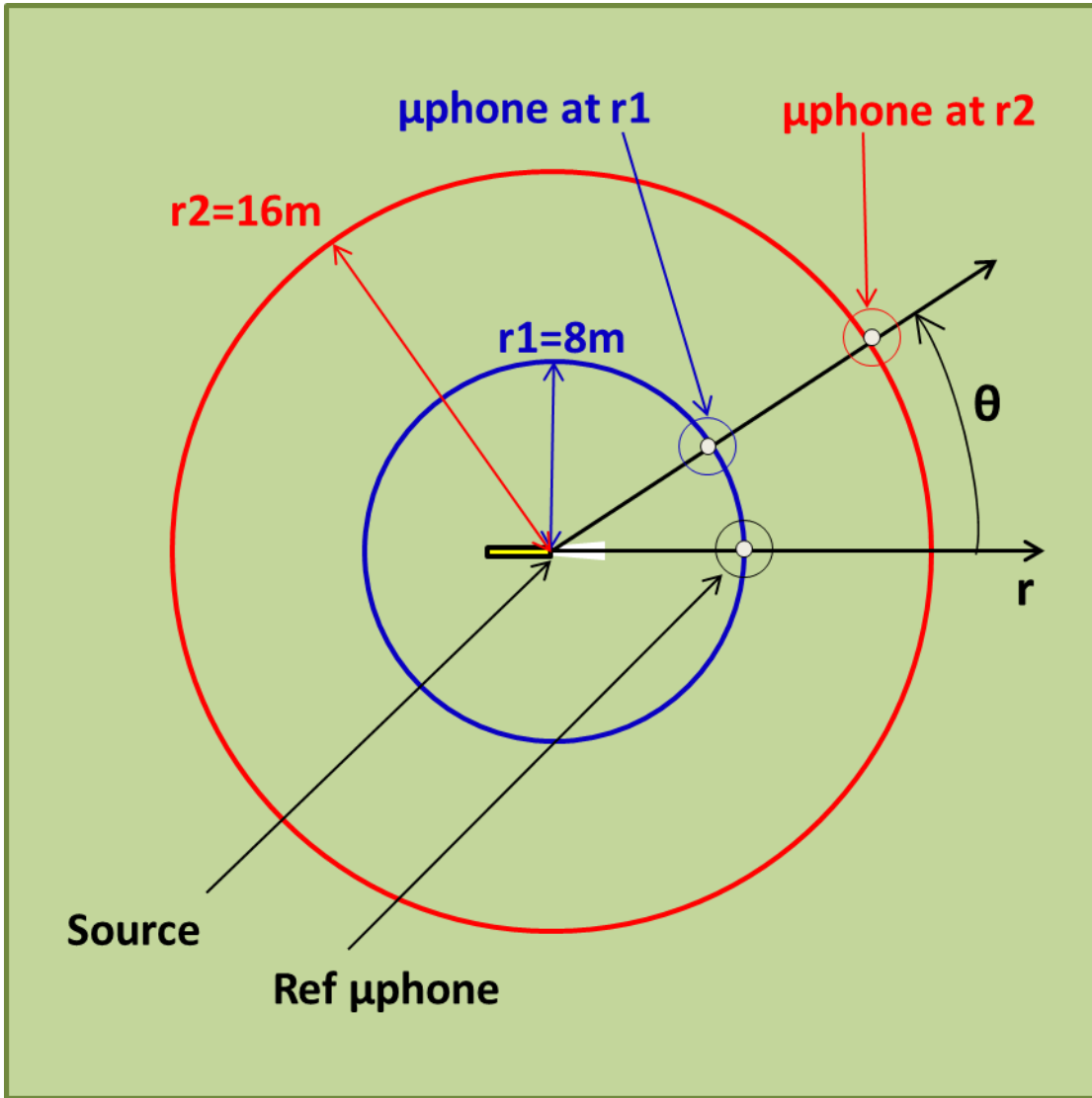
Figure 4.6: Experimental setup for full circle directivity measurements.

4.7 Jet Velocity

An experiment was performed in order to characterize the velocity decay along the output jet axis. A Pitot tube was used to measure the stagnation pressures along the jet axis from the exit of the jet nozzle out to 0.413 m. The measured stagnation pressures were used to calculate the flow velocities. The airstream was modulated at a frequency of

8 Hz for this experiment. Therefore it was necessary to choose the cycle of the wave form from which to calculate the velocity. The cycle with the maximum peak stagnation pressure was always chosen, and the peak stagnation pressure was used to calculate the velocity. These measurements allowed for the characterizations of the maximum peak velocity decay along the jet axis. The set up for this experiment is seen in Fig. 4.7.
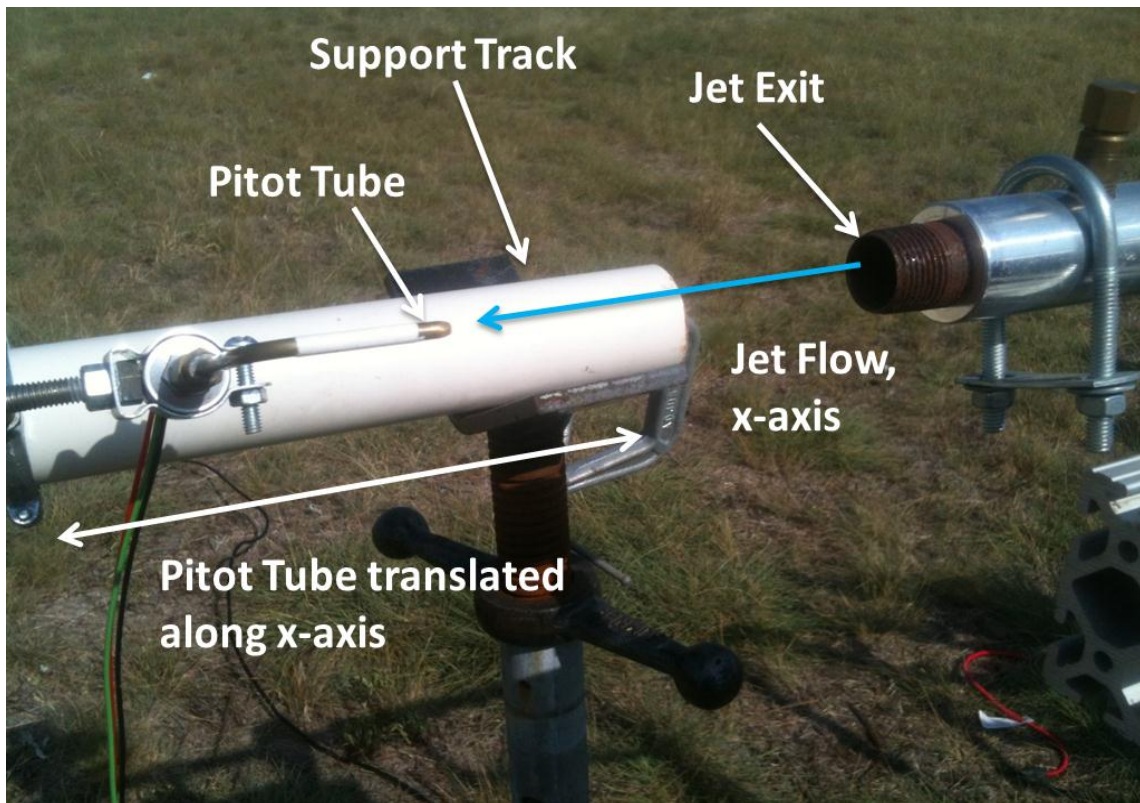
Figure 4.7: Sliding track setup for centerline velocity decay experiment.

Chapter 5

Results

The results of the experiments are detailed in the following section. The collected experimental data will be displayed and discussed, along with possible explanations for system behavior.

5.1 Typical Measurement Waveforms

In Figs. 5.1 and 5.2 below, typical measured waveforms are shown. Fig. 5.1 is a typical waveform for the acoustic signal captured by the microphones. Specifically, it is a narrow band filtered signal with a bandwidth from 6.3 to 10 Hz, measured with a cushion wind filter at 16 m, for an output signal of 8 Hz. Fig. 5.2 shows a typical Pitot tube measurement for the same experimental run as the acoustic data. It shows each individual pressure "surge" of the jet that corresponds to each acoustic wave. The envelope of the Pitot tube pressure pulses shows a sharp rise followed by a gradual decay caused by the depletion of the reservoir. The envelope of the acoustic signal follows a similar growth and decay, except the rise time is slower possibly due to the narrow band pass filtering of the signal.

The Pitot tube data was used to calculate the monopole source strength, volume velocity Q, using Equations (11), (1), and (20). An example time series of the calculated volume velocity is shown in Fig. 5.3. The Pitot tube data can also be used to approximate the dipole source strength, F, using Equation (24). An example of the calculated force

time series is shown in Fig. 5.4. It can be seen in Figs. 5.3 and 5.4 that the monopole and dipole source strengths are in phase. This will cause the source to have an asymmetric radiation pattern, as the monopole and dipole pressures will add constructively in the direction of the flow and destructively in the opposite direction.

The theoretical monopole pressure was predicted by using the measured source strength Q, in Equation (23). The volume velocity value that was selected was the maximum peak value from a time series at a specific frequency. For example, the maximum peak-to-peak volume velocity for f=8 Hz, shown in Fig. 5.3, is approximately Q_{pp}=0.19 m^3/s. Therefore, a source strength of Q=0.095 m^3/s would be used in Equation (23) to predict the monopole pressure. The theoretical dipole pressure was predicted using the measured source strength F, in Equations (30) (vertical orientation) or (33) (horizontal orientation). The force that was selected was the maximum peak value from a time series at a specific frequency. For example, the maximum peak-to-peak force for f=8 Hz, shown in Fig. 5.4, is approximately F_{pp}=130 N. Therefore, a peak dipole strength of F=65 N would be used in Equation (30) or (33), depending on the infrasound source orientation. The total sound pressure level would then be calculated using Equation (34).

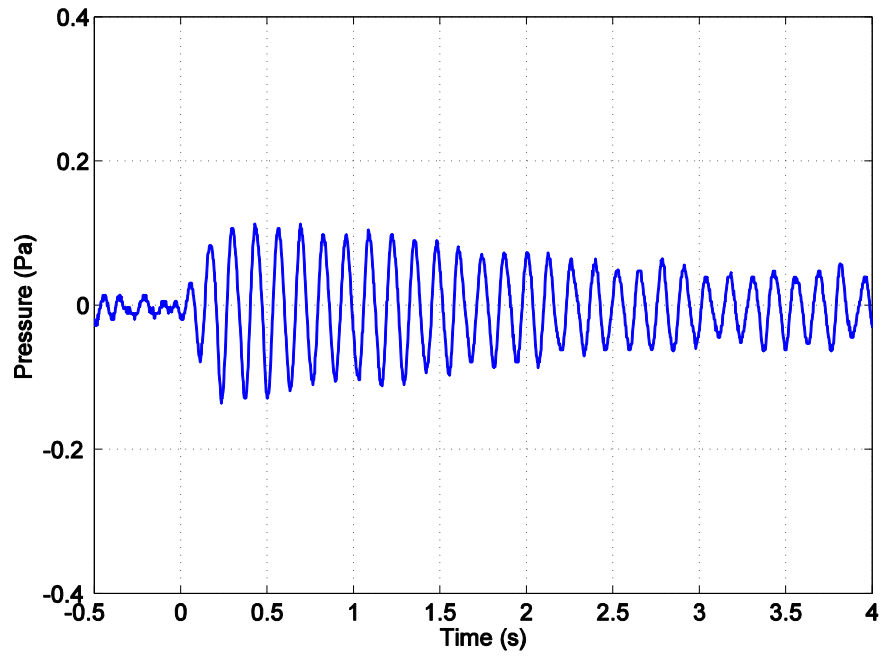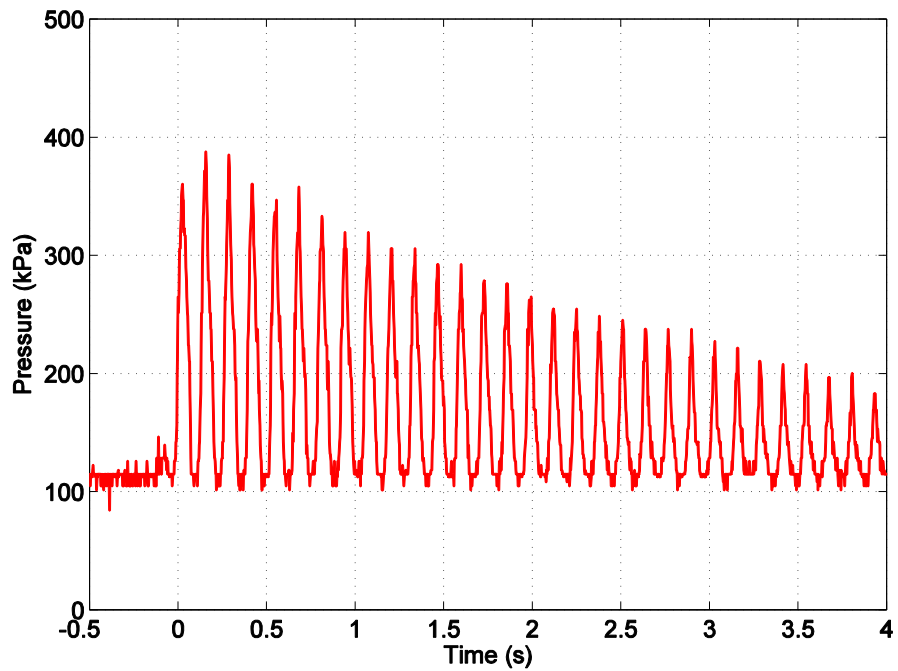**Figure 5.1: Example waveform for microphone data.**

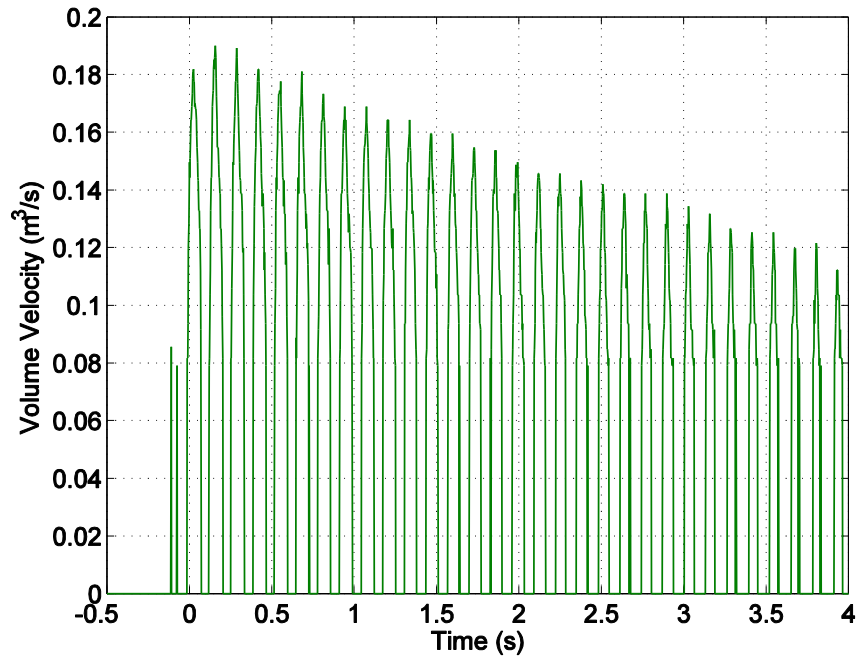**Figure 5.2: Example waveform for Pitot tube pressure data.**

61

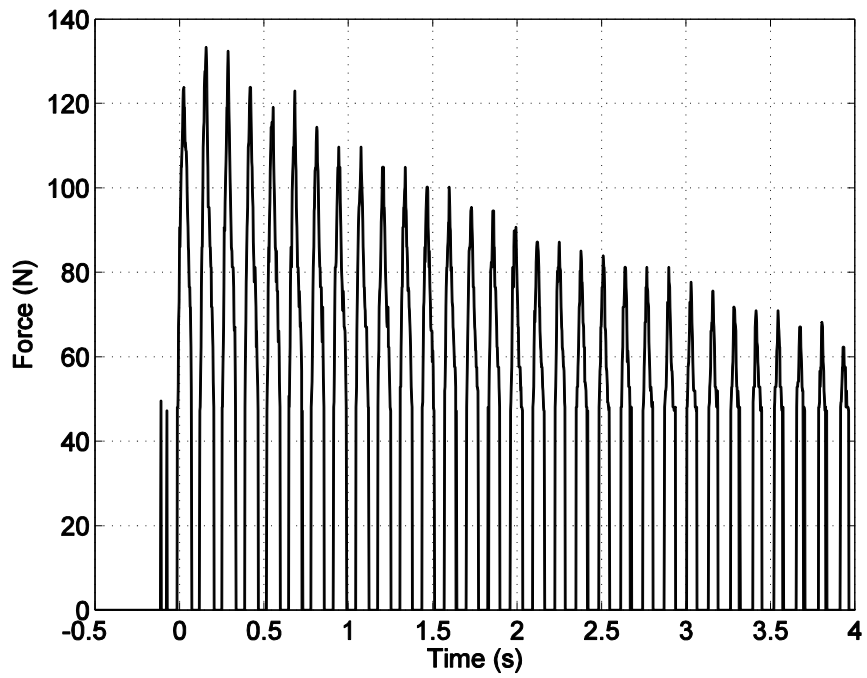**Figure 5.3: Example waveform for measured volume velocity.**

Figure 5.4: Example waveform for measured force.

62

5.2 Flow Visualization

The results of the flow visualization measurements are shown below in Figs. 5.5 through 5.12. The subsequent frames were taken from a high speed movie, taken at 600 frames per second. The frequency of the flow modulation is approximately 3.7 Hz. Therefore, the entire sequence of photographs showing the evolution of the jet lasts about 0.27 seconds, from startup to maximum to shut down. While the water vapor served as a decent medium for the flow visualization, much of the motion away from the centerline of the jet is not observed, due to the water vapor becoming less dense and thus more difficult to visualize. It should be noted therefore, that there is much more motion in the surrounding medium that includes swirling and circulation as well as the shedding of eddies that is not captured in these photos. Anecdotally, the flow was seen to disturb foam padding on the ceiling about 4 meters above the nozzle exit, whereas, the flow can only be visibly seen for about a meter. However, this flow visualization serves to qualitatively demonstrate the large amount of turbulence in the flow, and show how the jet spreads and evolves with time. The jet spreads to a maximum solid angle of 23°, as seen in Fig. 5.8.

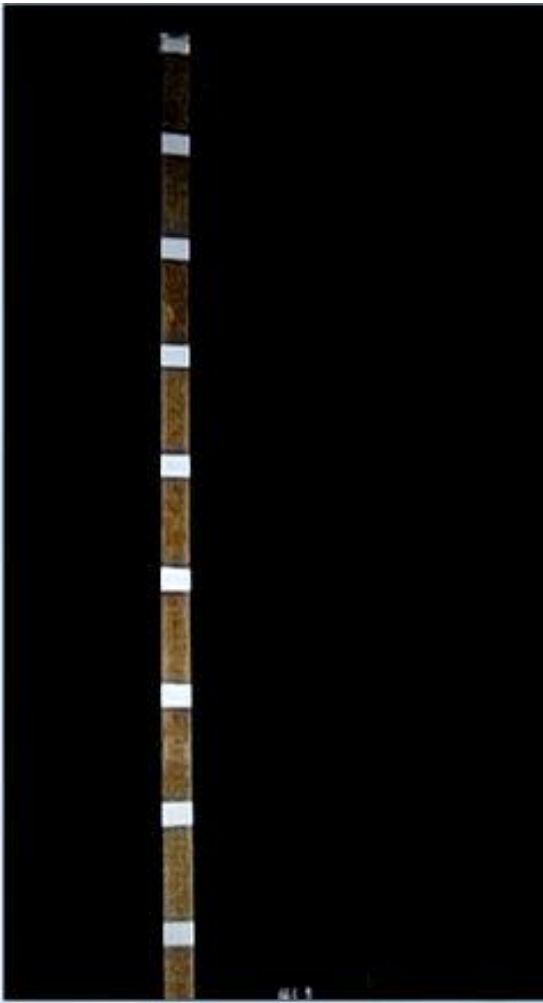**Figure 5.5: Startup T = 0 seconds.**

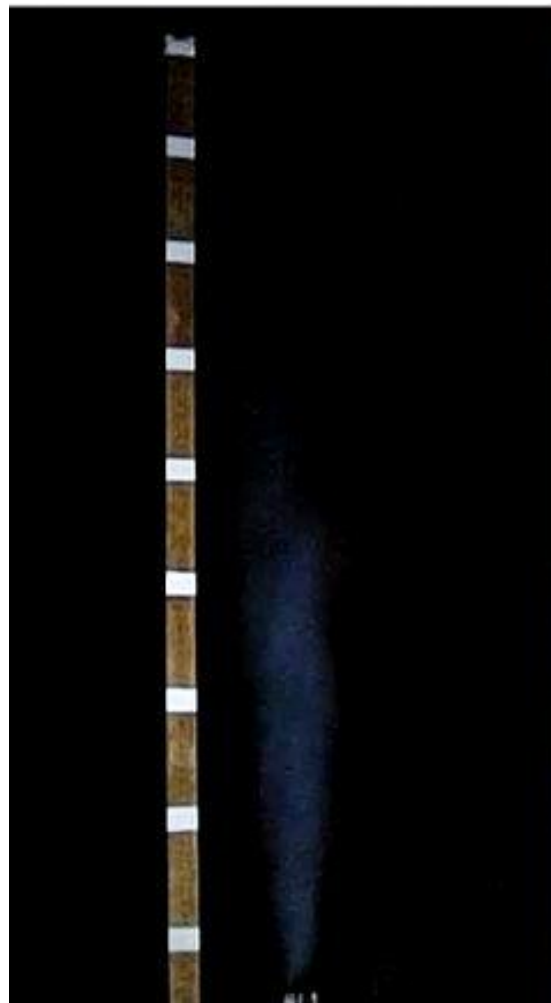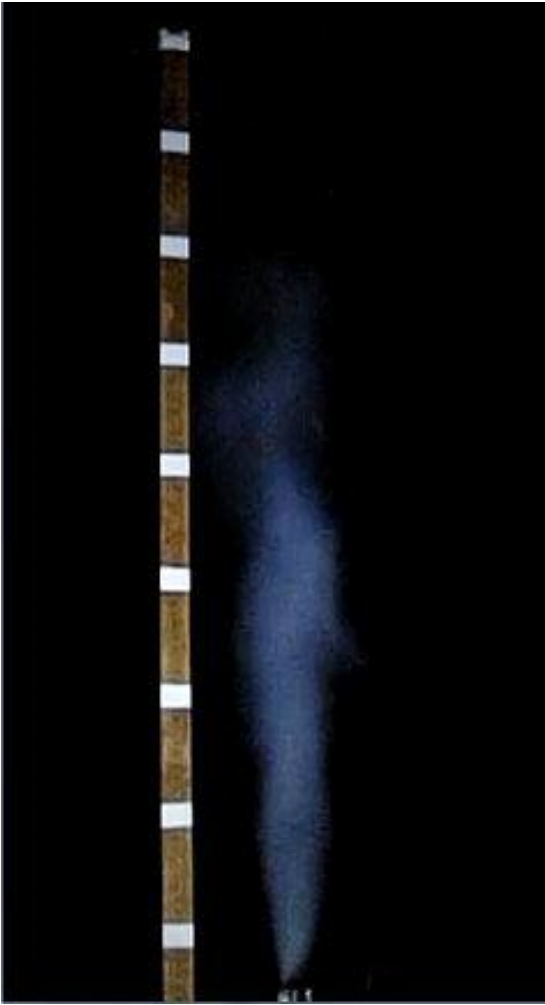**Figure 5.6: Increasing T ≈ 0.0386 seconds.**
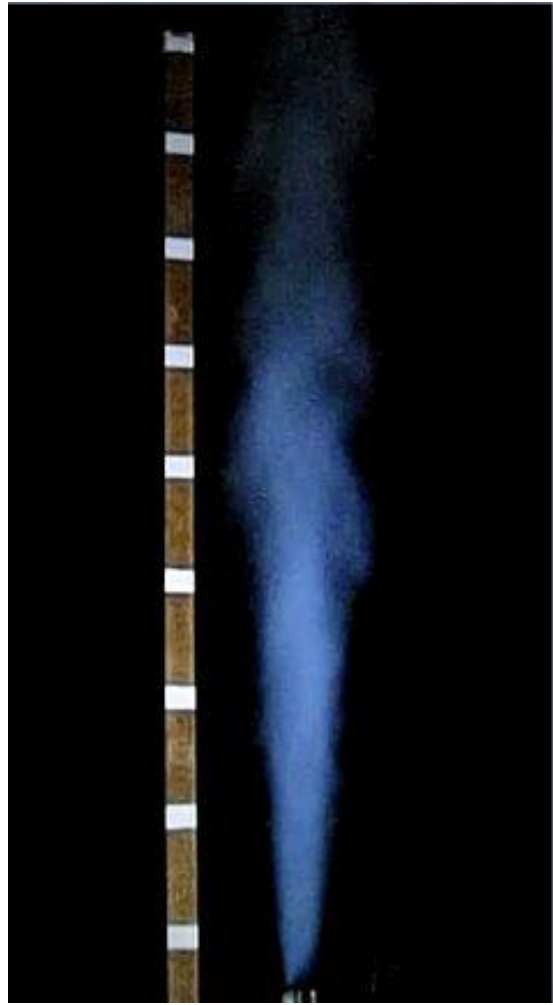
Figure 5.7: Increasing T ≈ 0.0772 seconds.   **Figure 5.8: Maximum T ≈ 0.1158 seconds.**

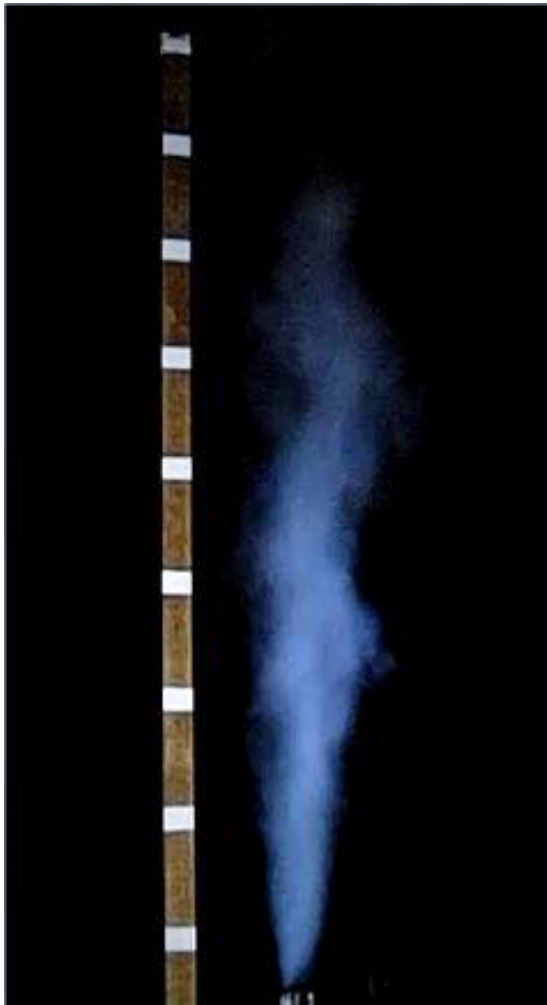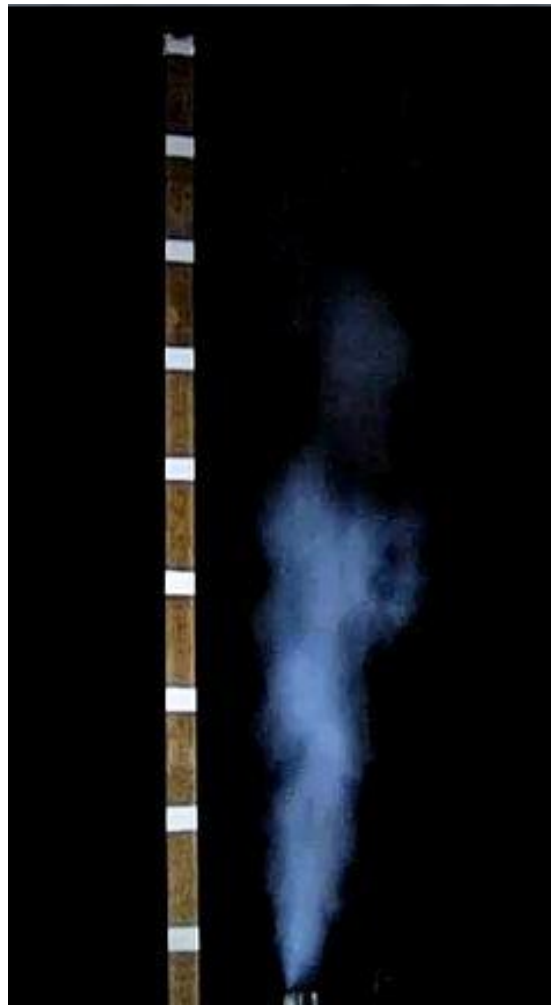**Figure 5.9: Decreasing T ≈ 0.1544 seconds.**
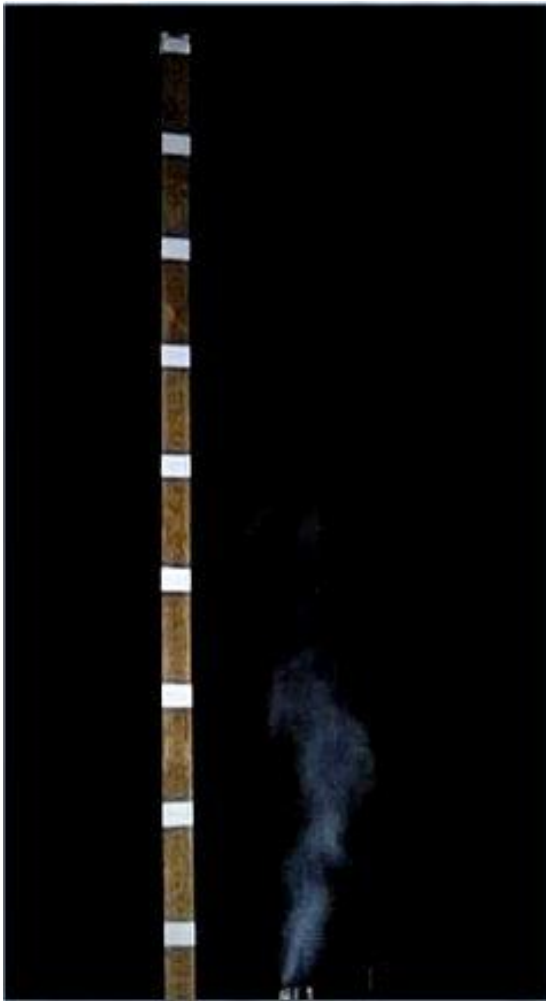

Figure 5.10: Decreasing T ≈ 0.1930 seconds.

Figure 5.11: Decreasing T ≈ 0.2316 seconds. **Figure 5.12: Shutdown T ≈ 0.2702 seconds.**
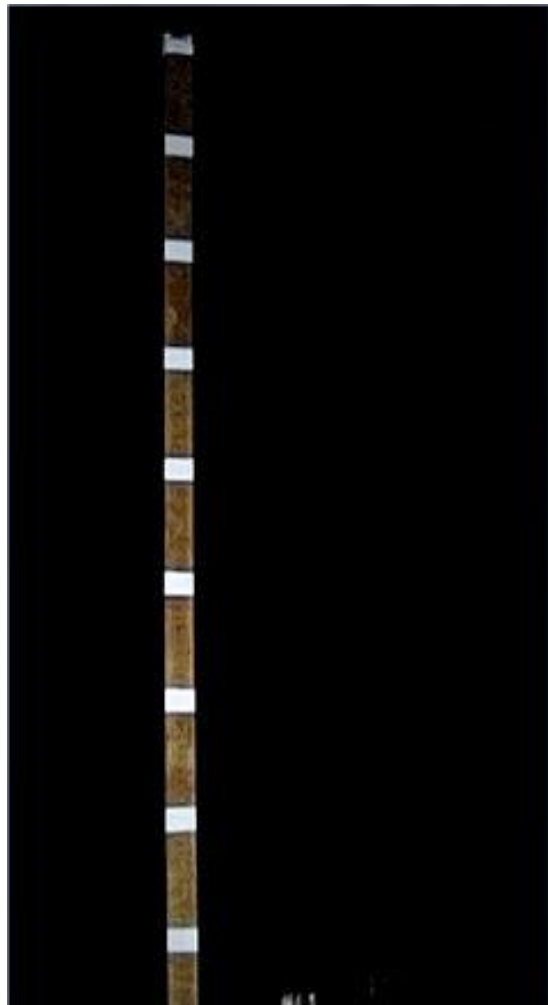
5.3 Empirical Source Strengths

The Pitot tube measurements that were used to characterize the jet flow volume velocity were taken at the outlet of the jet pipe. The Pitot tube was positioned in the middle of the pipe in order to make velocity measurements on axis. The peak stagnation pressure of the time series recorded at this location was used to calculate the peak velocity of the jet flow. The peak volume velocity was found by multiplying by the pipe exit area. The peak thrust force of the flow was likewise calculated, using the peak stagnation pressure of the time series multiplied by the pipe exit area. The peak source strengths for the monopole and dipole model were measured in this manner.

During the experimental process, it was found that the jet velocity from the exit nozzle varied as a function of frequency. In particular, the successive maximum pressure of the modulated pulsations decays slower for increasing frequency. This frequency dependence was observed when using the Pitot tube to measure stagnation pressure and calculate the velocity and thrust force. This was an anticipated result, and there are a number of obvious physical explanations. The most feasible explanation is that at the lowest frequencies, the air is being vented so rapidly that by the time the ball valve completes a rotation, the air in the reservoir is largely depleted. Since the force that accelerates the air jet to its maximum velocity is determined by the reservoir storage pressure, and the reservoir storage pressure is dependent on the volume of compressed air in the storage tanks, as the air runs out, the velocity and force of the air jet decreases. At high frequencies, the ball valve is only open for a short amount of time, so the reservoir back pressure remains more constant over a larger number of cycles, and the velocity and

force are higher, for a longer period of time. At low frequencies, tremendous amounts of air are vented for even one cycle, meaning that the reservoir pressure is being greatly decreased before the ball valve can completely open. This shown in Fig. 5.13, where the peak pressures of the lower frequency signals have both a lower maximum amplitude and a faster decay rate than the higher frequency signal peak pressures. The test shown in Fig. 5.13 is for the horizontal orientation, but similar trends are expected in the vertical case. This causes the source strengths of the low frequency waves to be weaker, as the cyclic repetition increases. One way to remedy this problem would be to incorporate a pressure regulator into the system plumbing to ensure that each air pulse has the same back pressure. However, pressure regulators have a tight, time-variable air constriction which would limit the volume outflow of the jet. Alternatively, a larger reservoir could be employed so that the amount of air lost for each low frequency cycle is negligible to the total reservoir volume, thus allowing for an effectively constant reservoir pressure.
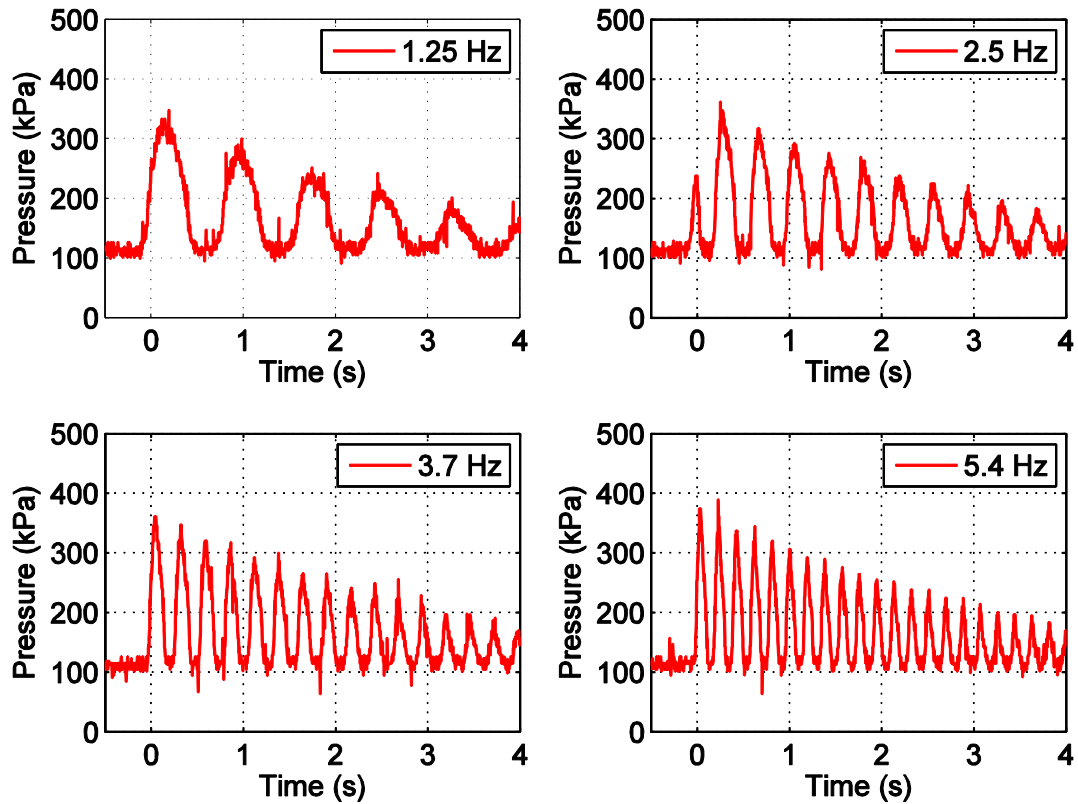
Figure 5.13: Pitot tube waveforms for increasing frequency for horizontal orientation.

This frequency dependence was observed in both the vertical and horizontal exit pipe orientations. An empirical fit for the monopole source strength, volume velocity Q, and the dipole source strength, thrust force F, was generated from the measurements for use in the theoretical source model given by Equations (23), (30), and (33) of the theory chapter. The source strength measurements and the accompanying empirical curve fits can be seen in Figs. 5.14-5.17. Figs. 5.14 and 5.15 show the empirical relationships for the peak volume velocity and peak force while in the vertical nozzle orientation. Likewise, Figs. 5.16 and 5.17 show the volume velocity and force empirical relationships for the horizontal nozzle.

70
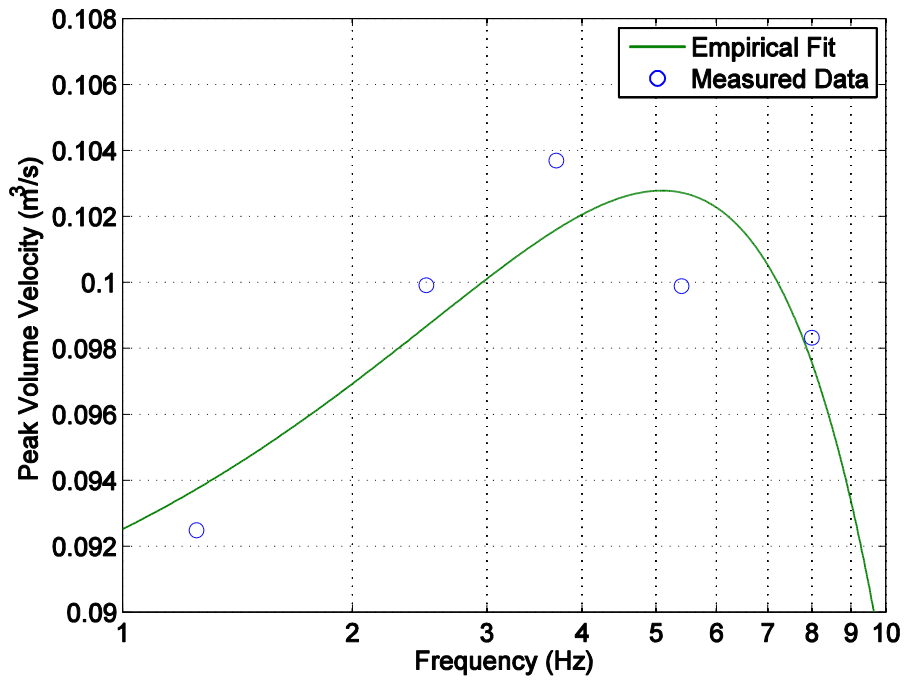
Figure 5.14: Peak volume velocity empirical fit vertical jet nozzle.
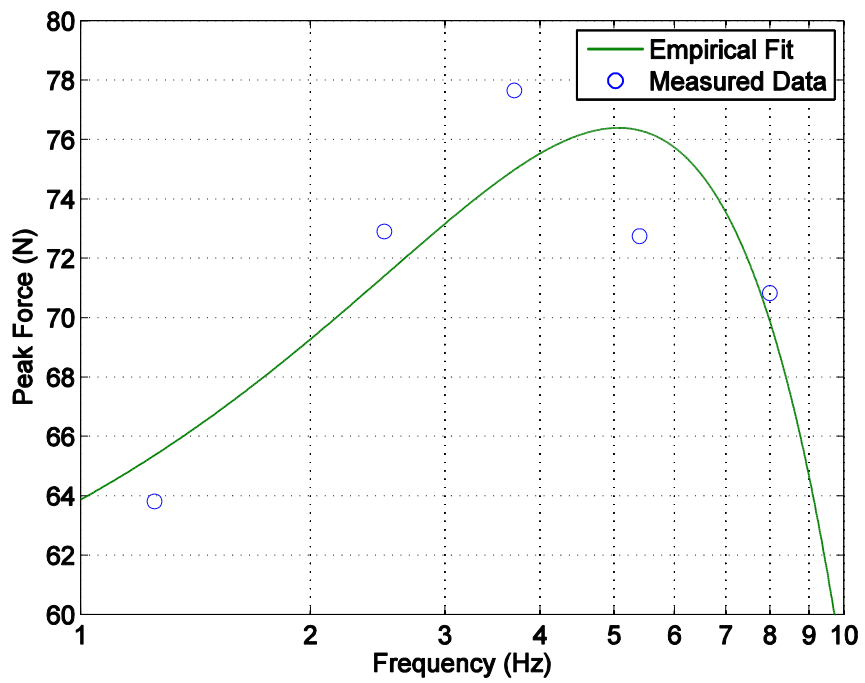
Figure 5.15: Peak force empirical fit vertical jet nozzle.

71

The empirical fit of the vertically oriented nozzle is found to follow a quadratic trend, contrary to the constant trend that would be expected with an infinitely large reservoir. While the empirical fit does not match the collected measurements exactly, it follows the trend of the data well. It should be noted however, that this empirical fit is only valid through a frequency of 8 Hz, as above this frequency, there is a roll-off caused by the quadratic nature of the empirical curve fit. The empirical curve fits for the horizontally oriented jet pipe are shown below, in Figs 5.16 and 5.17.
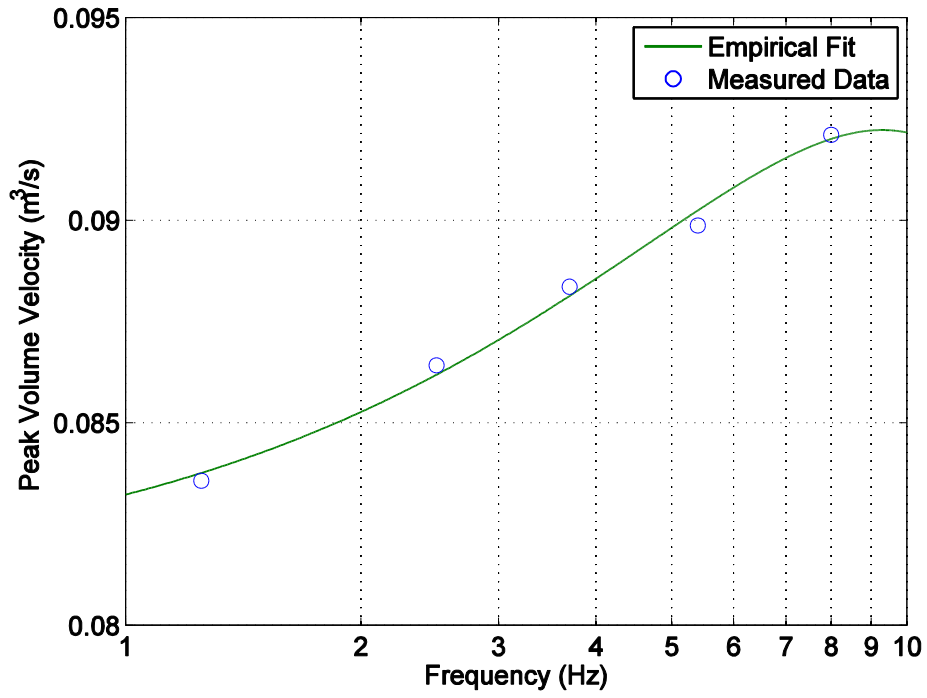
Figure 5.16: Peak volume velocity empirical fit horizontal jet nozzle.
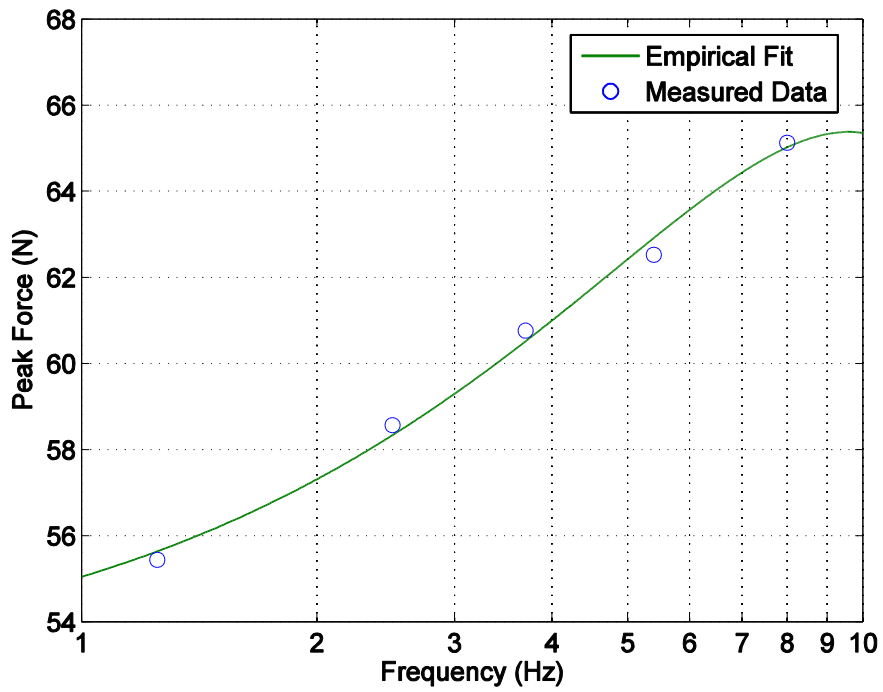
Figure 5.17: Peak force empirical fit horizontal jet nozzle.

73

The above figures show that the source strength frequency dependence for the horizontally oriented nozzle follows a quadratic trend with frequency, rather than a constant trend as would be expected from a system with a reservoir of unlimited size. These four empirical curves will be used for the source strengths, Q and F, when comparing the theoretical predictions to the measured data. The difference between the vertical and horizontal source strength frequency responses is unexplained at this time. A possible explanation is the use of different sensors for the vertical orientation (PCB$^{\text{TM}}$ Model 102A02) and the horizontal orientation (Kavlico$^{\text{TM}}$ P255). The details of the two sensors are included in Appendices C and D.

5.4 Propagation

The propagation experiments were performed for both vertical and horizontal nozzle configurations, with the microphone(s) placed at increasing ranges along the ground. For the vertical nozzle, a band of frequencies was tested from 1.25 Hz to 8 Hz over a range of 2 m to 24 m. For the horizontal nozzle, the same band of frequencies was used at somewhat longer ranges, due to the fact that microphone measurements are simply not feasible in the high aerodynamic flow close to the exit nozzle. The results can be seen in Figs. 5.18-5.22 for the vertically oriented nozzle and in Figs. 5.23-5.27 for the horizontally oriented nozzle. Comparisons to theory from Chapter 3 are also shown and will be discussed in more detail in a subsequent section.

5.4.1 Vertically Orientated Propagation

Not all frequencies were detectable over the full range of distances for the vertical nozzle experiments. The 1.25 Hz signal was only detectable at ranges of 2 m and 4 m. The 2.5 Hz and 3.7 Hz signals were only detectable over the ranges of 2 m to 8 m. Only the 5.4 Hz and 8 Hz signal were detectable over the entire range of 2 m to 24 m. This is reflected in the displayed data in Figs. 5.18-5.22. It should be noted that the SPL for the 1.25 Hz infrasound signal is larger than the SPL of the other frequencies at the 2 m range but quickly falls off, being undetectable at 8 m. It is seen that higher than expected amplitudes occur near the source. The cause of this is unknown, but it is very possible that aerodynamic flow and circulation could be interacting with the microphones for this short range and low frequency. It is more pronounced for this frequency than for the other frequencies due to the longer duration of the air pulses.

Each of the figures below show the recorded data with circles or asterisks, with the theoretical model of a combined point monopole and point dipole with a solid line (Equations (23) and (30), respectively), the theoretical dipole contribution with a dashed-dotted line (Equation (30)), and the theoretical monopole contribution with a dashed line (Equation (23)). For the vertical nozzle measurements, data with the asterisks were taken with the ½″ diameter Bruel & Kjaer microphone™, while the circles denote the data collected with the 1″ diameter Bruel & Kjaer microphone™ (see Appendix A for specifications).
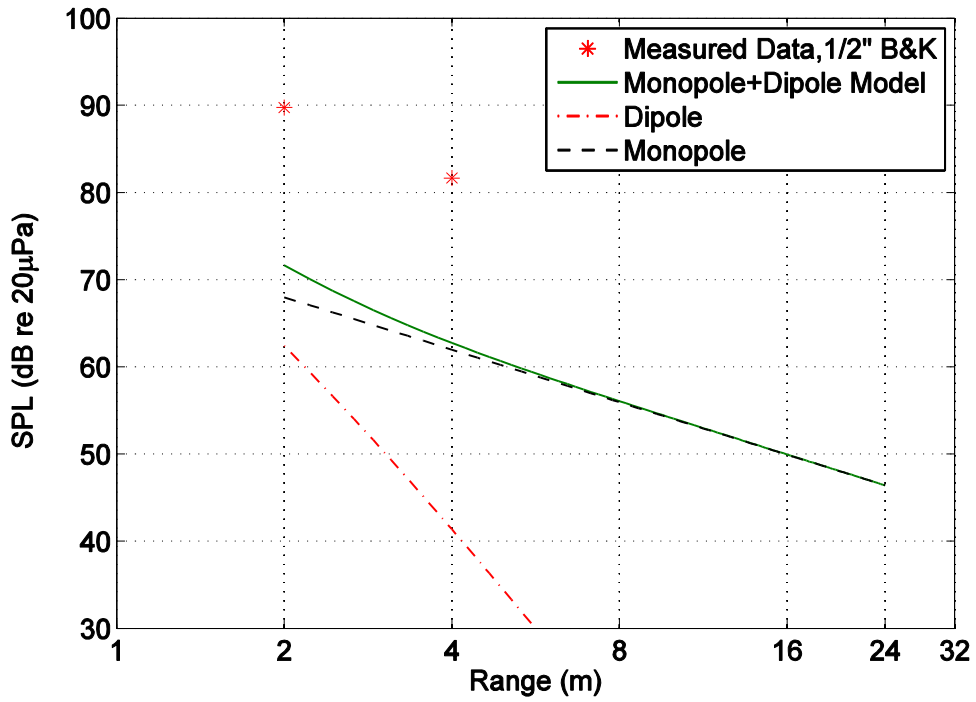
Figure 5.18: Propagation measurements for vertical jet nozzle f=1.25 Hz.
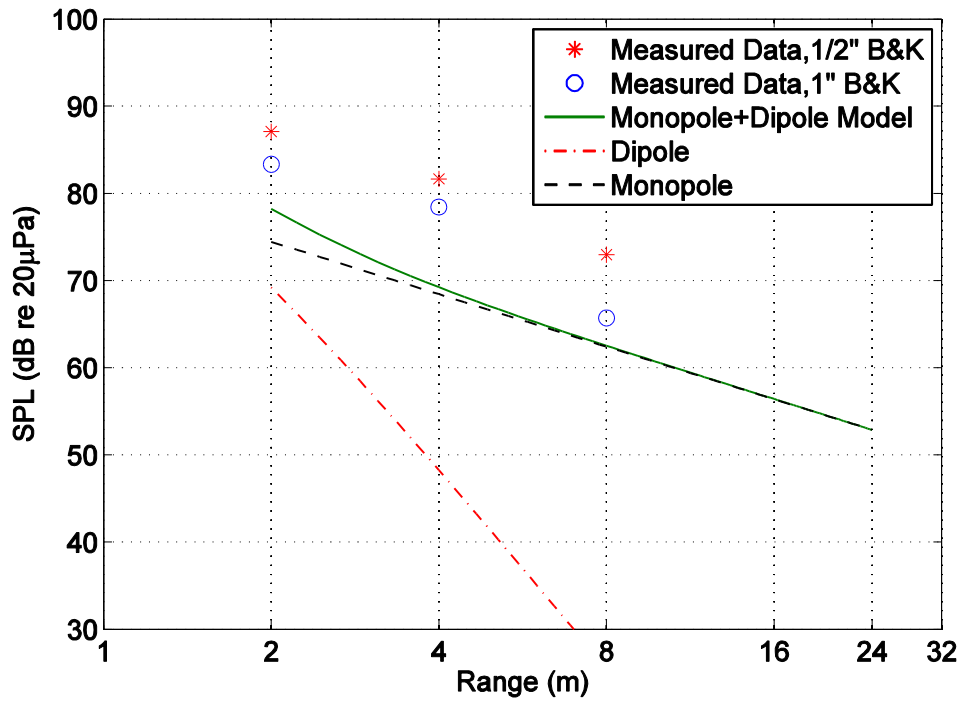
Figure 5.19: Propagation measurements for vertical jet nozzle f=2.5 Hz.

76
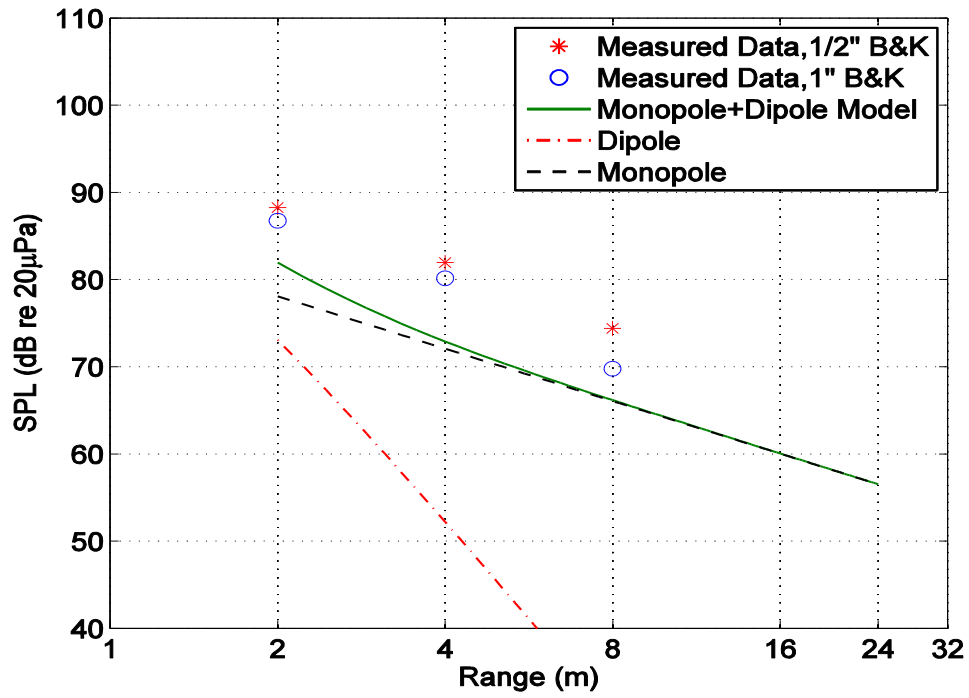
Figure 5.20: Propagation measurements for vertical jet nozzle f=3.7 Hz.
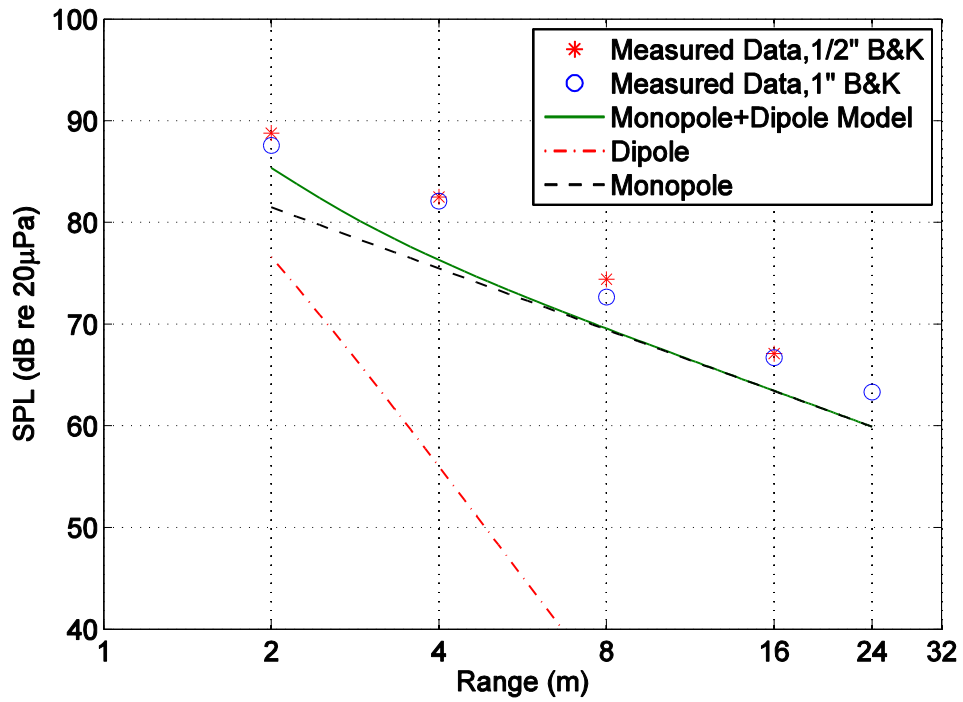
Figure 5.21: Propagation measurements for vertical jet nozzle f=5.4 Hz.
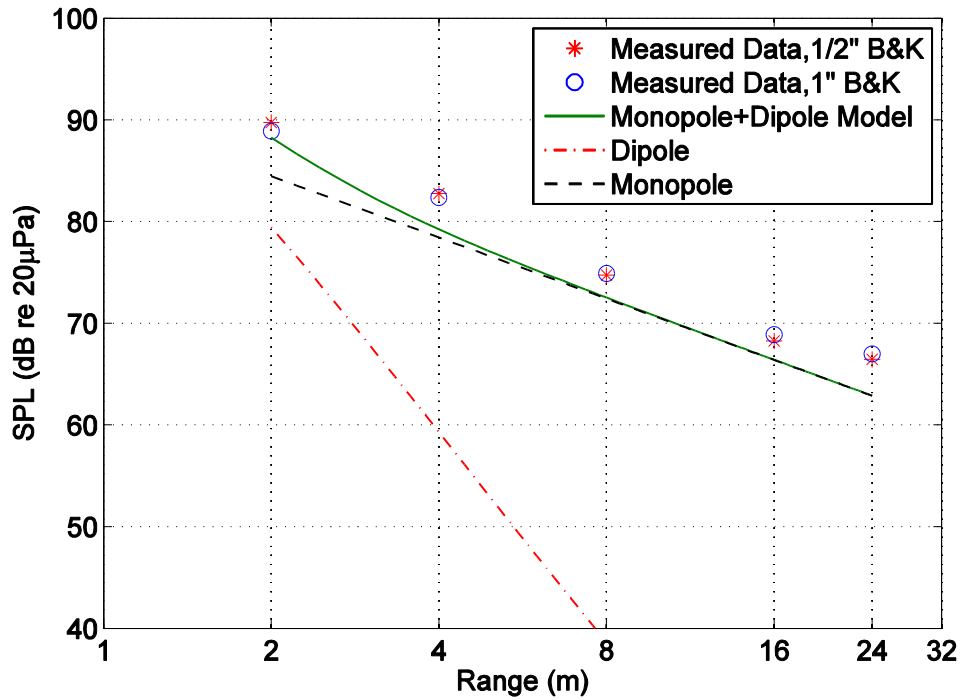
Figure 5.22: Propagation measurements for vertical jet nozzle f=8 Hz.

5.4.2 Horizontally Oriented Propagation

For the horizontal orientation, a band of frequencies was tested from 1.25 Hz to 8 Hz over a range of 8 m to 24m. The results can be seen in Figs. 5.23-5.27. For the 8 Hz signal, one additional measurement was made at a propagation range of 32 m. For all other frequencies, the signal was undetectable at this range due to the overwhelming presence of wind noise in the filtering band. For the horizontal measurements, only one microphone, a G.R.A.S. Corporation ½" diameter Model 40AZ ™, was used to collect the data (see Appendix B for specifications). As for the case of the vertical nozzle data, all of the following plots contain measured data, compared to the theoretical model, the dipole contribution, and the monopole contribution. The monopole contribution is given

78

by Equation (23) and the dipole contribution is given by Equation (33) from the theory, Chapter 3.

It can be seen that when horizontally oriented, the pressure wave spreads proportionally to r^{-2}, causing a drop in 12 dB per octave. Contributions from the monopole increase the source strength, especially at higher frequencies. This is predicted by Equation (33) of Chapter 3, as for small kr (low frequencies and close ranges), the acoustic pressure is proportional to r^{-2}. However, as kr is increased, it can be seen that sound pressure level follows spherical spreading, as the dipole pressure in Equation (33) becomes proportional to r^{-1}. This is especially noticeable in the 8 Hz propagation measurements. In each of the cases for the horizontal nozzle propagation measurements, the proposed model of a combined monopole and dipole matches the data well.

It can be observed that the horizontal nozzle configuration has an added gain of ~6 dB across the frequency band and thus can be detected out to farther propagation ranges. This result will be explained in the directivity section, to follow. However, due to hydrodynamic nearfield and jet interactions with the microphone, short range measurements were not made. All measurements were of course made within a wavelength away from the source, due to the extremely long wavelengths of infrasonic signals.
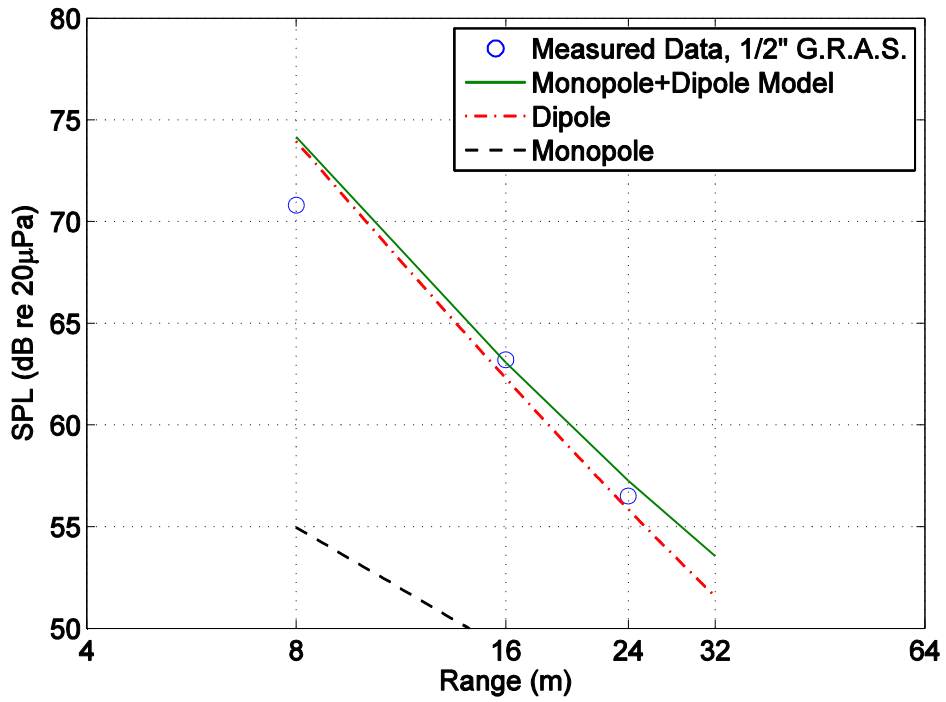
Figure 5.23: Propagation measurements for horizontal jet nozzle (on axis) f=1.25 Hz.
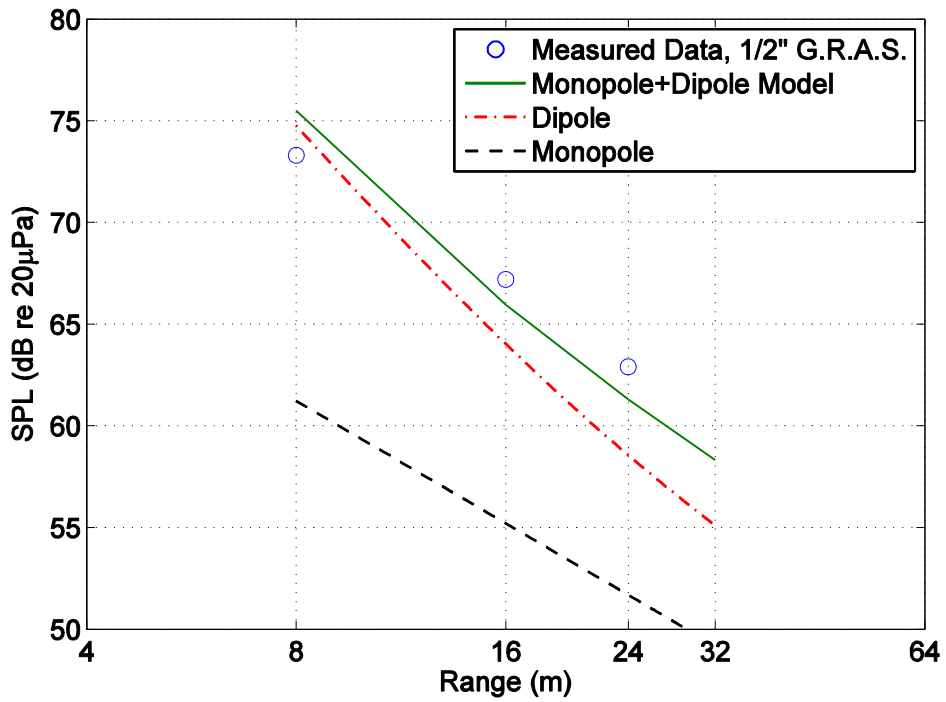
Figure 5.24: Propagation measurements for horizontal jet nozzle (on axis) f=2.5 Hz.
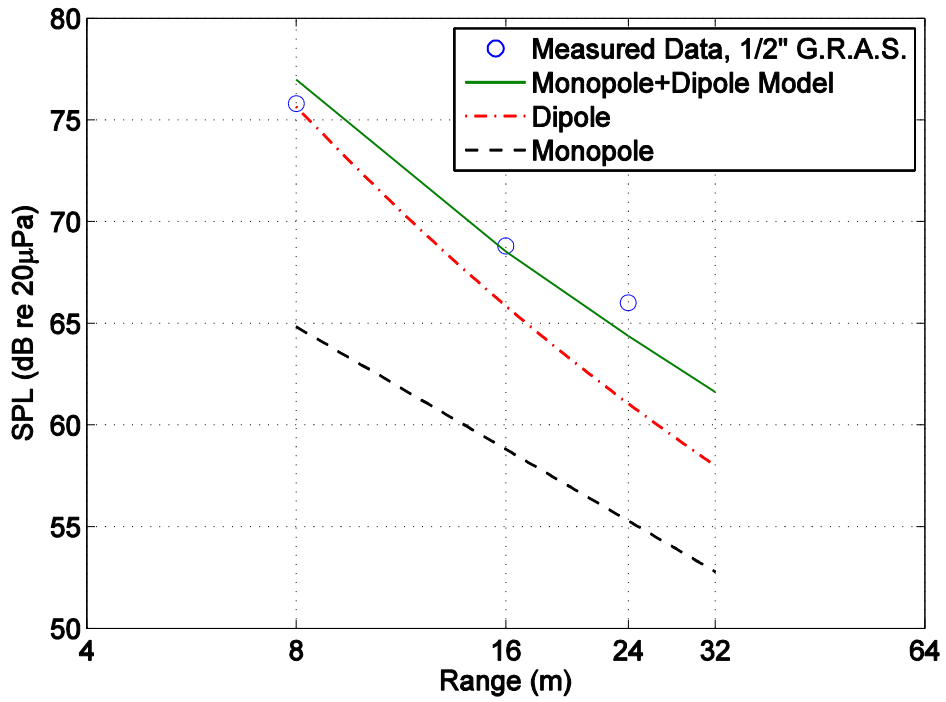
Figure 5.25: Propagation measurements for horizontal jet nozzle (on axis) f=3.7 Hz.
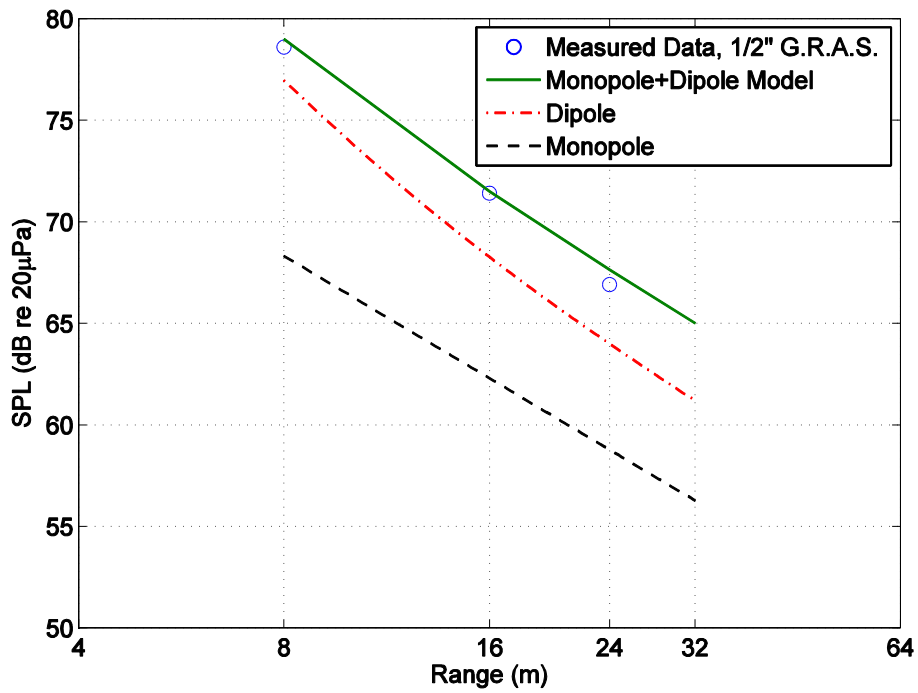
Figure 5.26: Propagation measurements for horizontal jet nozzle (on axis) f=5.4 Hz.
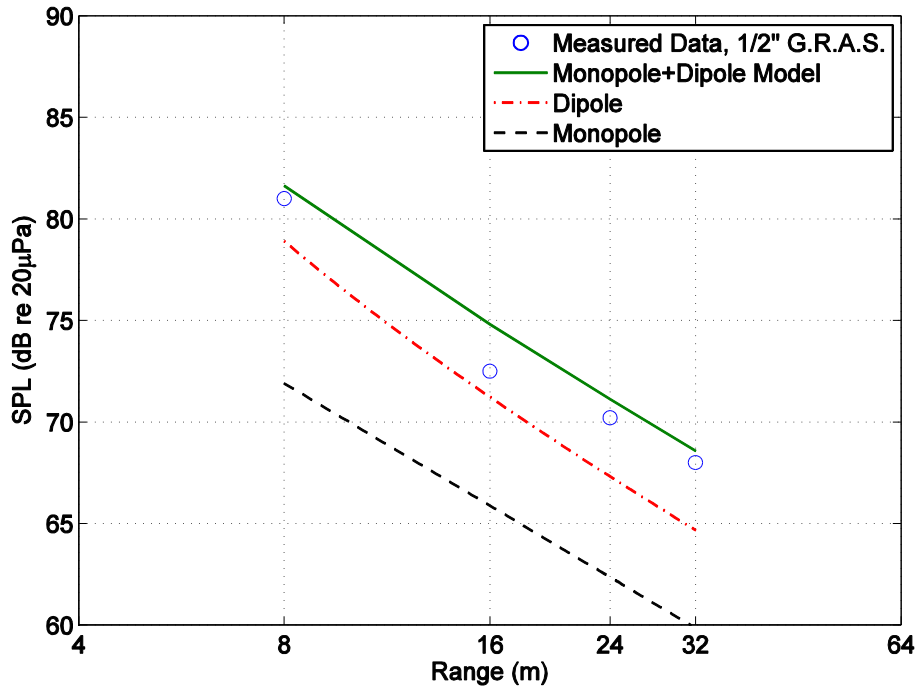
Figure 5.27: Propagation measurements for horizontal jet nozzle (on axis) f=8 Hz.

5.4.3 Brief Observations

It is interesting to examine the measured results of our experiments in light of the theoretical predictions. For the vertical nozzle, the dipole component is found to be weak, while the monopole only contribution is potentially strong. This is predicted by Equation (30), where the acoustic pressure exerted by the dipole will be near zero when the microphone is located on the ground. The opposite is true for the horizontal nozzle, as predicted by Equation (33). The horizontal nozzle shows that the dipole only component is strong whereas the monopole contribution is relatively weak. Of course, the most satisfying and appropriate theory curves are those for the physically correct superposition of monopole and dipole sources. This points to the significance of our nozzle orientation,

82

as it dictates the alignment of the dipole axis and the acoustic pressure contribution of the dipole.

5.5 Frequency Response

The frequency response experiment was performed for both vertical and horizontal configurations.

5.5.1 Vertically Oriented Frequency Response

For the vertical nozzle configuration, the frequencies measured spanned from 1.25 Hz to 8 Hz for ranges from 2 m to 8 m. The results are shown in Figs. 5.28-5.32. For the 8 m, 16 m, and 24 m ranges, some of the frequencies were unable to be detected due to the strong presence of wind noise in the band pass filtered signal bands. For the 8 m range, only the 1.25 Hz signal was undetectable, while for the 16m and 24 m, only the 5.4 Hz and 8 Hz signal were measurable. It can be seen that there is a slight increase in SPL with increasing frequency. Over the ~ 2 octave band from 2.5 Hz to 8 Hz, there is an increase of ~2 or 3 dB. Yet again, as in the case of the propagation measurements, the 1.25 Hz signal does not follow this trend and its SPL is actually stronger at 2 m than the SPL of the signals immediately higher in frequency, perhaps implicating aerodynamic influences at the microphone. At 4 m, the 1.25 Hz signal decreases relative to the other frequencies and is undetectable at 8 m. It is proposed that these anomalous results are caused by aerodynamic effects present at this range for the 1.25 Hz infrasound signal.

83

Moreover, the 1.25 Hz signal is near the low end frequency threshold for our microphones, and the data may not be as reliable as for higher frequencies.

In each of the subsequent plots, the data measured by the 1″ B&K microphone is displayed with circles, the data measured by the ½″ B&K microphone is displayed with asterisks, the combined theoretical point source and point force model is plotted with a solid line, the dipole contribution is plotted with a dashed-dotted line, and the monopole contribution is shown with a dashed line.

The discussion begins with results for the vertical nozzle. Comparisons to theory are made, with Equation (23) for the monopole only model, Equation (30) for the dipole only model, and the summation of the two for the monopole plus dipole model. For the range of 2 m, the level of the infrasound generator is overestimated, but the trends with increasing range match fairly well to the monopole plus dipole model, the agreement increasing with frequency, which will be shown to be the trend at all of the subsequent range datasets. For the frequency response at 4 m, the level and overall trend of the monopole plus dipole model match the data less well. It should be remarked that since all the measurements were done outdoors, they were subject to prevailing winds, which varied in strength over periods measured in minutes, typically at 2 - 15 mph, with less variability in direction. At both of these ranges, the dipole component of the source dominates the frequency response, while the monopole contribution is negligible. This may be due to the close proximity to the source. The inaccuracy of the 2 m frequency response may be due to the presence of strong aerodynamic effects at this range. For the ranges of 8, 16, and 24 m, the frequency response of the theoretical model is dominated

by the monopole contribution, and the dipole contribution all but disappears at ranges of 8 m and beyond. Consequently, the data at these ranges matches the level and trend of the monopole contribution better than that of the combined monopole and dipole. It must be noted that in this configuration, the axis of the dipole is perpendicular to the ground, and therefore the dipole components will be greatly diminished, as the receiver location is located near the null of the dipole directivity.

Figure 5.28: Frequency response measurements for vertical jet nozzle r=2 m.

Figure 5.29: Frequency response measurements for vertical jet nozzle r=4 m.

Figure 5.30: Frequency response measurements for vertical jet nozzle r=8 m.
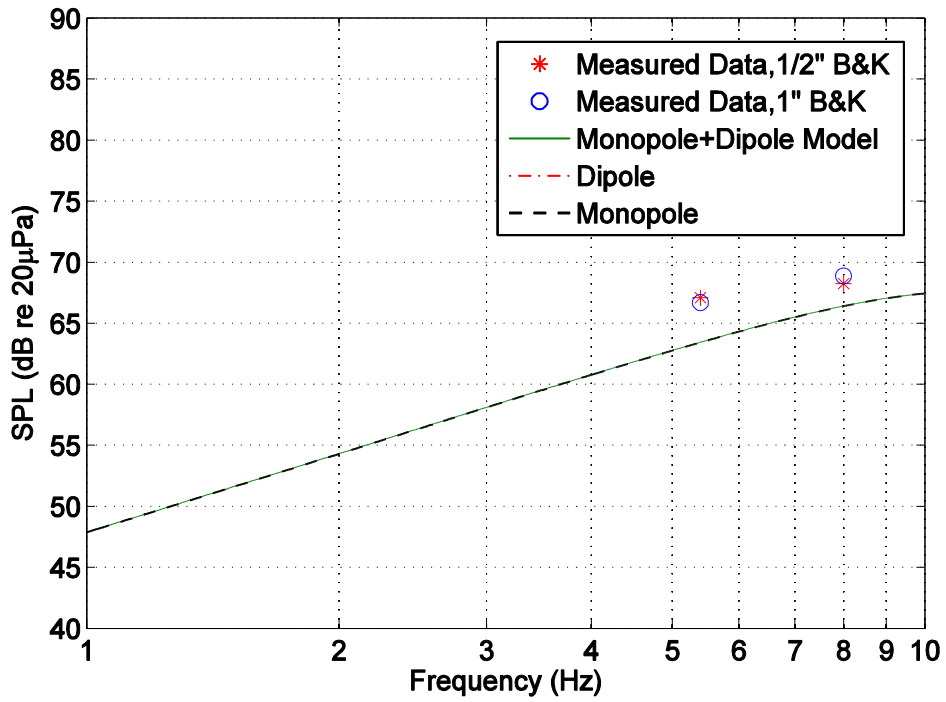
Figure 5.31: Frequency response measurements for vertical jet nozzle r=16 m.
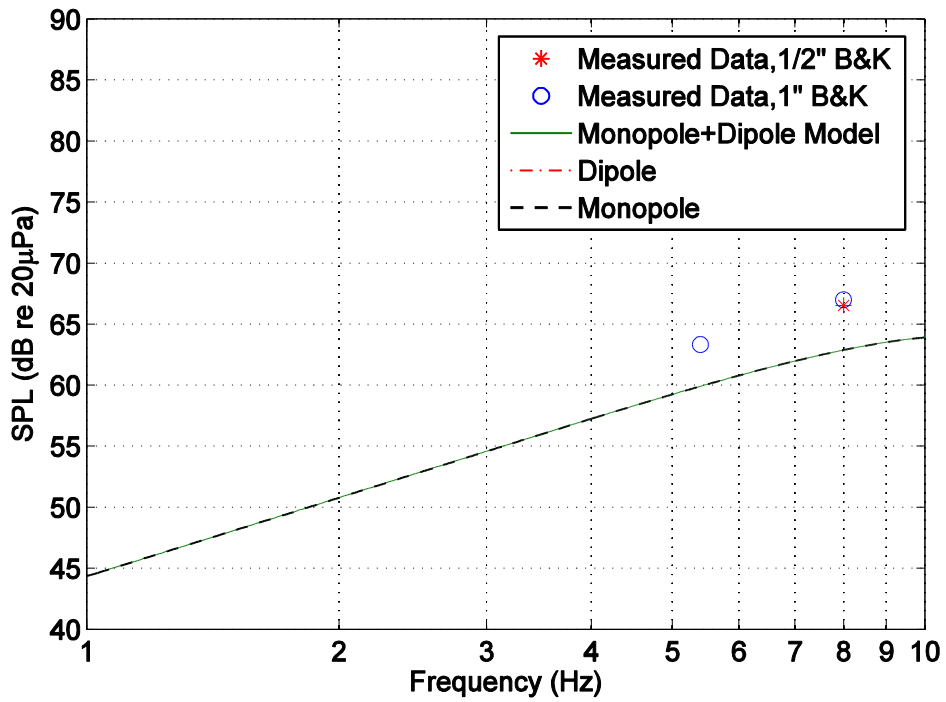
Figure 5.32: Frequency response measurements for vertical jet nozzle r=24 m.

87

5.5.2 Horizontally Oriented Frequency Response

For the horizontal configuration, the frequencies measured spanned from 1.25 Hz to 8 Hz for ranges from 8 m to 24 m. This can be seen in Figs. 5.33-5.35. Due to probable hydrodynamic nearfield and jet interactions with the microphone, measurements were unable to be accurately made at ranges of 2 m and 4 m. It can be seen in Figs. 5.33-5.35 that the measured SPL for 8, 16 and 24 m ranges increases with increasing frequency, leading to a ~10 dB increase as the frequency is increased from 1.25 Hz to 8 Hz.

For each of the ranges in the horizontal orientation, the model prediction matches the data points well. Furthermore, the frequency response generally follows the dipole frequency response with the level being boosted by the monopole component with increasing contributions at increasing frequencies. Yet again, for the horizontal nozzle orientation the theoretical model of a point source (Equation (23)) and point force (Equation (33)) is a sufficient model for the infrasound generator.
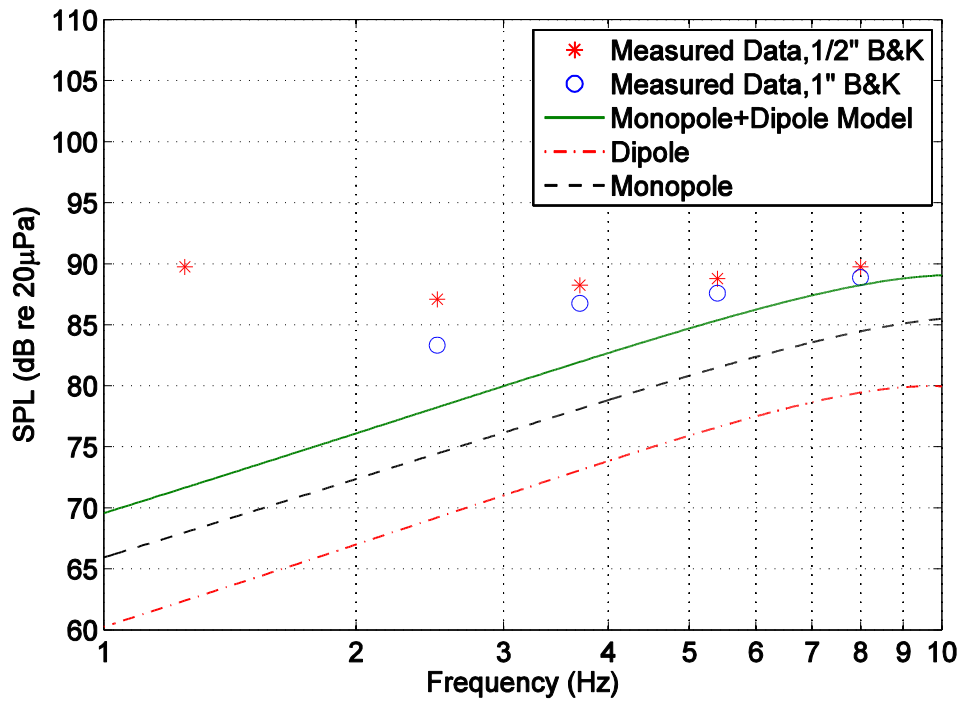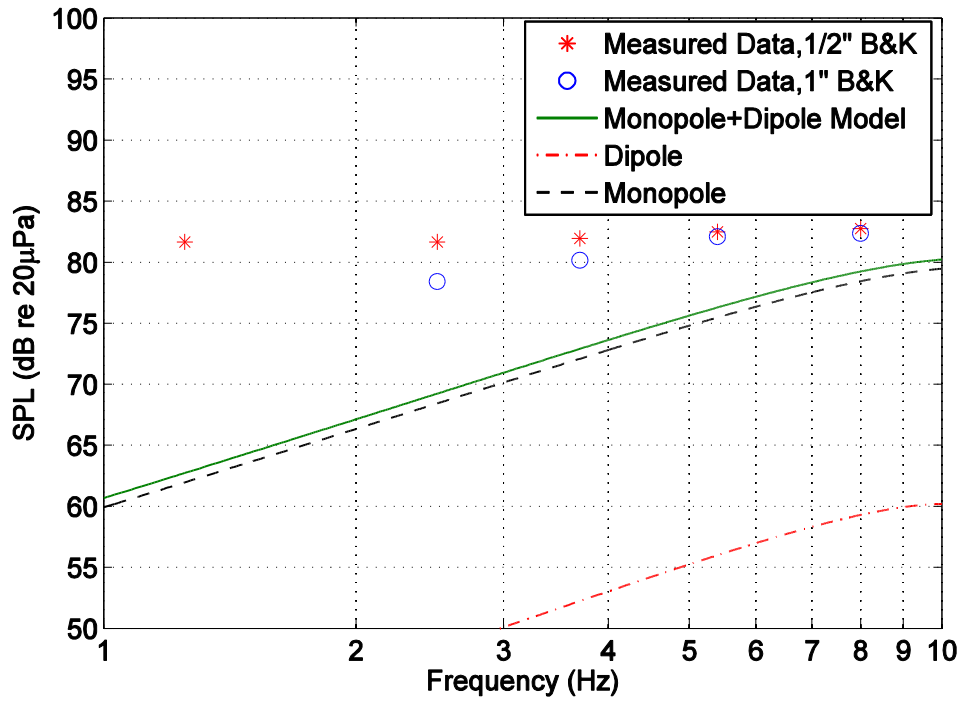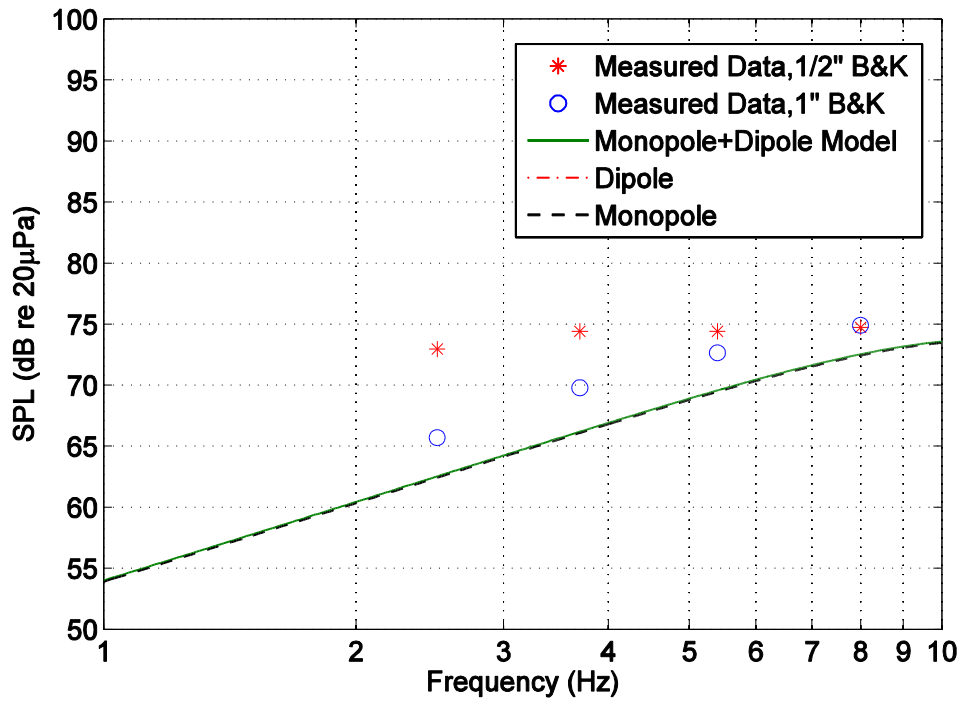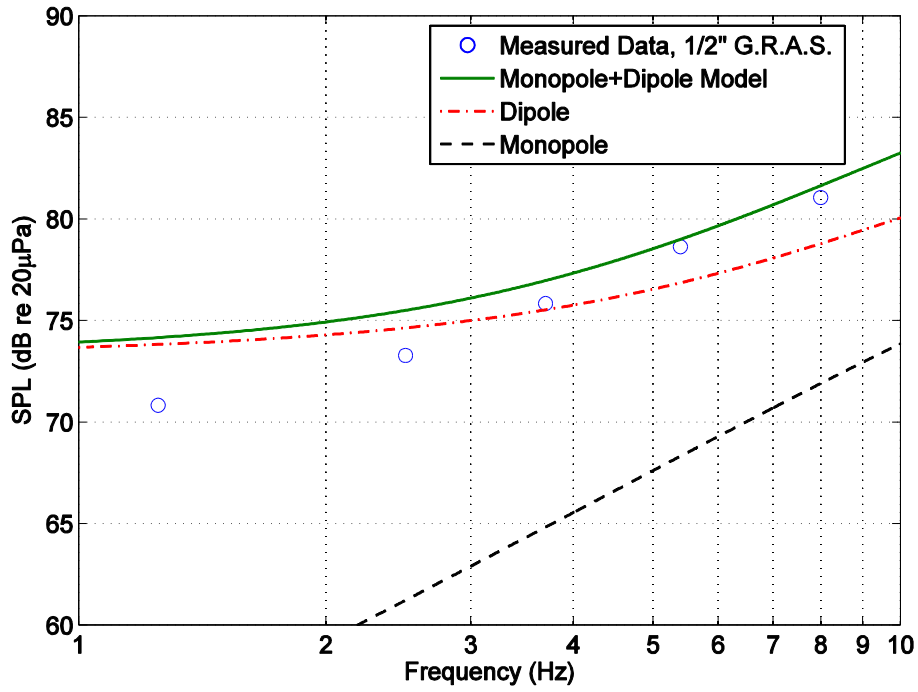
Figure 5.33: Frequency response measurements for horizontal jet nozzle r=8 m.
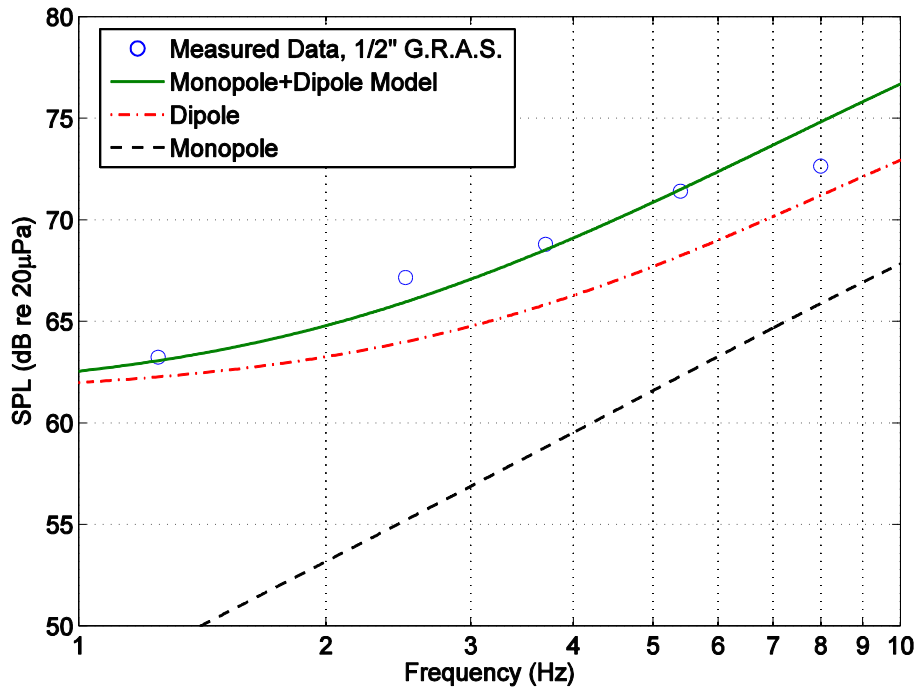
Figure 5.34: Frequency response measurements for horizontal jet nozzle r=16 m.
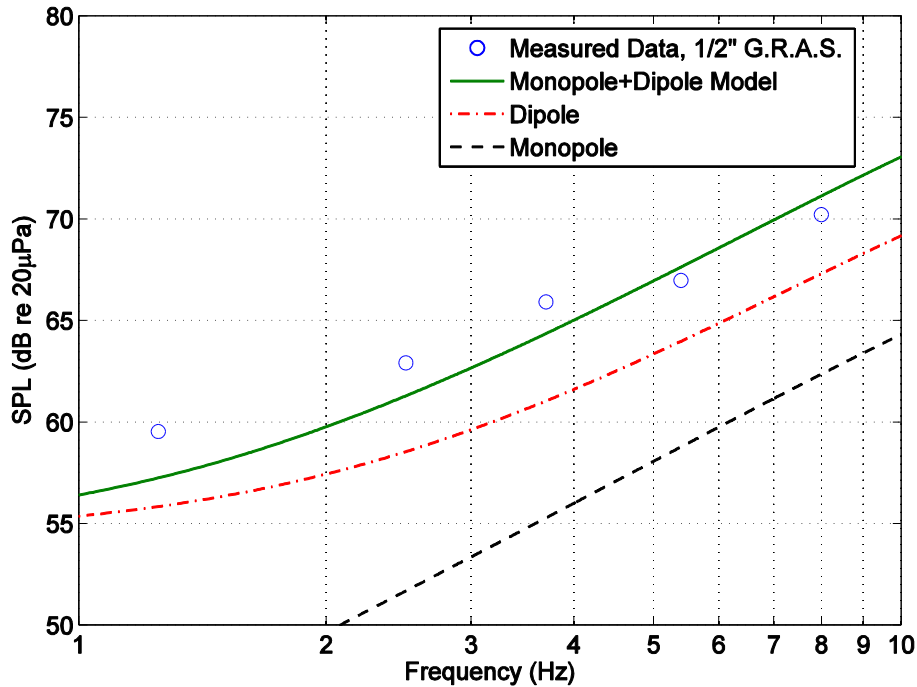
Figure 5.35: Frequency response measurements for horizontal jet nozzle r=24 m.

5.5.3 Vertical/Horizontal Frequency Response Compare

The only measurement overlap between the vertical nozzle configuration and the horizontal nozzle configuration is the frequency response of the system measured at 8 m. The two frequency responses can be seen in Fig. 5.36. The difference between the two increases with increasing frequency. At 1.25 Hz, the gain obtained by turning the nozzle horizontal is only a negligible amount (~1 dB), due probably to aerodynamic circulation, but at 8 Hz, the gain obtained by turning the nozzle horizontal is a significant 6 dB. Therefore, at higher frequencies, rotating the nozzle had the effect of doubling the signal. The difference in sound pressure level is also different between both microphones used to

collect the vertical orientation data. The difference between the two outputs is most likely due to the low frequency roll off of the 1″ B&K microphone.
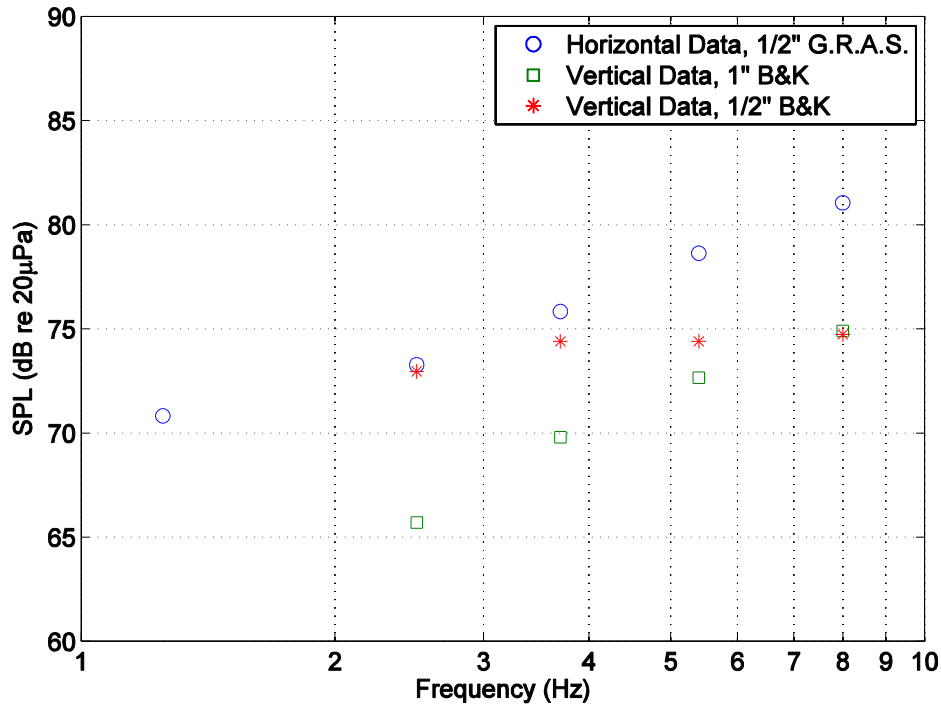
Figure 5.36: Comparison of frequency response measurements for horizontal and vertical jet nozzle.

5.6 Reservoir Volume

In order to determine the effect of the reservoir volume on the output infrasound signal, a test was performed with the exit jet in the vertical orientation at constant frequency and range, but with varying reservoir volume. The infrasound signal measured had a frequency of 3.7 Hz and was measured at a range of 1 m with a wide band filter. While 1 m is too close of a range to get meaningful quantitative infrasonic pressure measurements due to aerodynamic effects, in determining the qualitative effect of

reservoir volume on relative maximum pressure level, the data is instructive. The results of this test can be seen in Fig. 5.37.

It was observed that increasing the reservoir volume from 1 tank to 3 tanks does not significantly affect the maximum pressure amplitude of the infrasound signal. However, it was seen that signal amplitude is sustained for more cycles, as the amount of air in the reservoir has been increased. For example, in Fig. 5.37 the positive peak of the 4th cycle has a pressure value of less than 1 Pa for a reservoir with only one tank. The pressure value of the same peak on the same cycle for a reservoir with three tanks however, is 2 Pa. This demonstrates that with a greater air supply, the infrasound generator can produce greater signal amplitudes for a longer duration of time. This is simply because a larger reservoir contains a larger mass of air than a smaller reservoir. The volume this mass of air occupies in the atmosphere dictates the pressure, which is proportional to volume velocity. For a smaller reservoir at the same pressure of the larger reservoir, less air mass will be contained, and as air is released to the atmosphere, the air inside the tank will become less dense, thus lowering the reservoir pressure. This causes the potential energy of the stored air to be reduced. However, for the larger reservoir, air is vented out at the same maximum peak rate, but the mass of the air lost is smaller relative to the total tank size. Thus, when the air redistributes and expands, the equilibrium pressure reached will be closer to the original reservoir pressure than it would be for the smaller reservoir. For a larger reservoir system, the potential energy will be closer to a constant over the same period of time.

These effects are dictated by a physical phenomenon known as flow choking. Choked flow refers to a flow where the mass flow rate will not increase unless the reservoir pressure is increased. When flow traveling from a reservoir into the atmosphere goes through a restriction and the reservoir pressure is at least approximately 1.89 times greater than atmospheric pressure, the Mach number at the restriction will be equal to unity, and the flow will be choked. Thus, the mass flow rate is fixed. This is represented physically [36] by the expression,

$$\dot{M} = \frac{P_o A^*}{\sqrt{T_o}} f(\gamma, R) \qquad . \qquad (35)$$

In Equation (35), $\dot{m}$ is the mass flow, P_o is the reservoir pressure, T_o is the reservoir temperature, and $f(\gamma, R)$ is a function of the specific gas constant, R, and the ratio of specific heats for air, γ. A^* is the area of the nozzle where the Mach number is equal to unity, which for choked flow, corresponds to the area of the throat. From this equation it can be seen that for a reservoir with constant T_o, γ, and R, only the reservoir pressure, P_o, and throat area, A^*, can change the mass flow.

Choked flow is observed in the system when the reservoir size was changed. Although the amount of air available to the system was increased, the maximum output pressure stayed the same because the flow was choked and the mass flow of air out of the system was fixed. This choking also caused the signal to last longer, as it took a longer time for the reservoir to be emptied. The fixed mass flow rate can be overcome by increasing the pressure in the reservoir, or increasing the size of the throat.

At higher frequencies, less air is ejected per cycle due to the shorter period of time that the ball valve is open. Thus, higher frequencies sustain their maximum amplitude for a greater number of cycles than for low frequencies at a fixed reservoir volume. This is seen in Fig. 5.38, where the 2.5 Hz signal decays to less than half of its maximum positive peak pressure 4 cycles after the maximum pressure. In contrast, the 8 Hz signal decays to less than half of its maximum positive peak pressure 16 cycles after the maximum pressure.
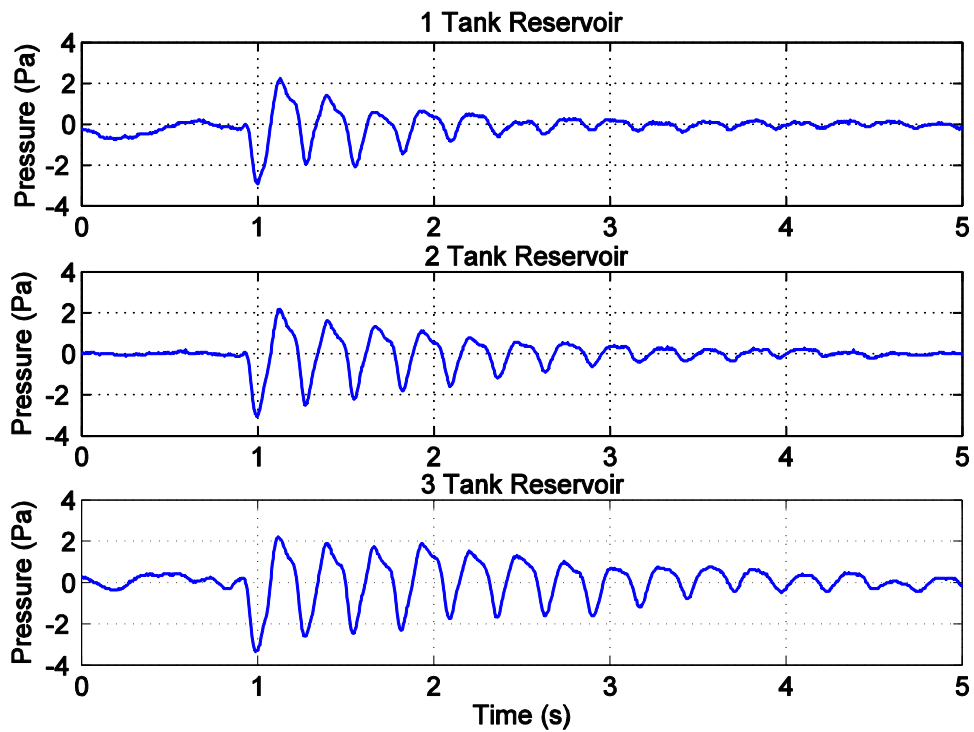
Figure 5.37: Acoustic waveforms for varying tank volume.
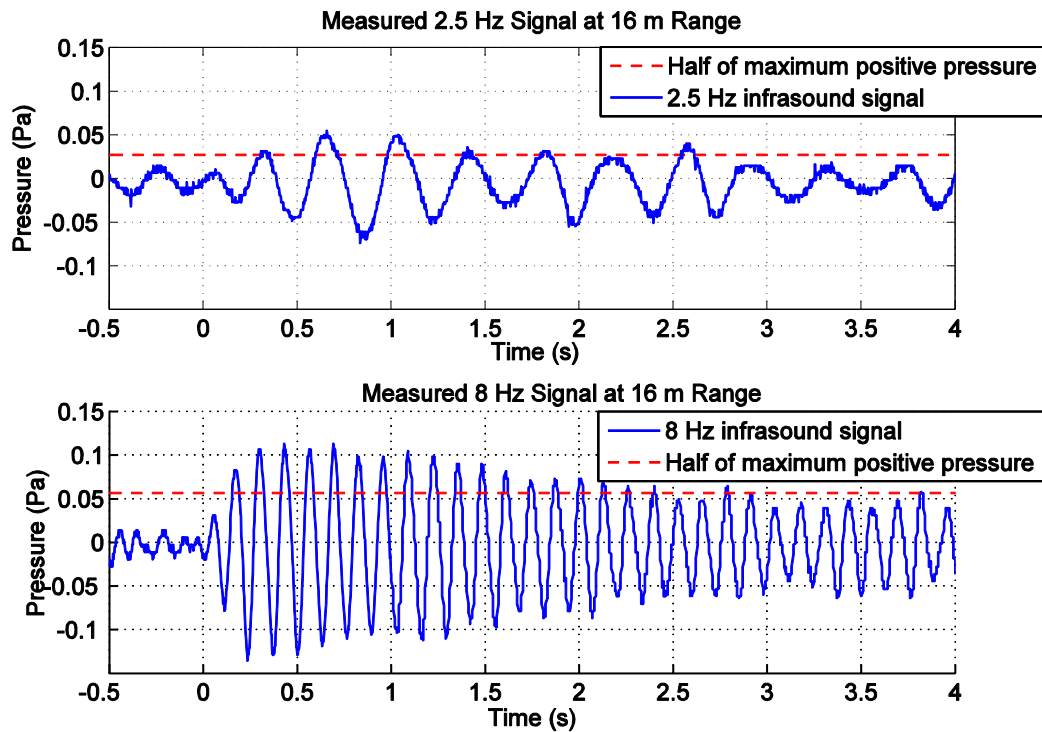
Figure 5.38: Comparison between 2.5 Hz and 8 Hz acoustic waveforms.

5.7 Directivity for the Horizontal Jet Orientation

Sound pressure level measurements were made for the horizontal jet outlet configurations, as a function of angle in the horizontal plane. The results can be seen in Figs. 5.39-5.52, where the jet nozzle axis was taken to be at the origin. All of the data was taken with the ½″ G.R.A.S. microphones, placed under the "Papasan" cushion, to reduce or eliminate aerodynamic effects. The directivity measurements are displayed in two different formats. In the first display method, the polar plots display the measured sound pressure levels, along with the sound pressure levels predicted by the theory (Equation (34)). Some of the on-axis directivity measurements differ slightly from the on-axis propagation measurements because the experiments were performed on different

95

days with different weather conditions. For example, the measured SPL for the on axis 1.25 Hz propagation data was recorded as 71 dB re 20 µPa. However, Fig. 5.39 shows that both the measured and theoretically predicted on axis SPL for the 1.25 Hz signal is 74 dB re 20 µPa. This is simply a result of varying experimental conditions in the field. The second way the data is displayed is on rectangular plots with both the measurements and theoretical predictions being normalized. The measured acoustic pressures were normalized against a reference microphone that was located on the jet axis at a range of 8 m. For the quarter circle measurements, the reference microphone was a ½″ G.R.A.S. microphone. For the full circle measurements, the reference microphone was a 1″ B&K microphone. The theoretically predicted acoustic pressures were normalized by the theoretical on axis value.

5.7.1 Single Quadrant Directivity Measurements

Figs. 5.39-5.48 show the directivity of the infrasound source for angles from 0° to 90° for frequencies of 1.25 Hz to 8 Hz, at a measurement range of 8 m. The theoretical directivity of the combined monopole and dipole model (Equation (23) and Equation (33)) are plotted in the figures with solid lines while the measured data points are plotted with circles. The polar plots show that the theory matches the sound pressure levels well for all angles. Likewise, the rectangular beam patterns show that the general shape of the beam pattern matches the normalized measured data well. The model does a good job matching the data, especially at the highest frequencies. The asymmetric shape of the directivity pattern could be attributed to the monopole and dipole source strengths being

in phase (Figs. 5.3 and 5.4), causing constructive interference in the direction of the flow, and destructive interference in the opposite direction. Similar directivity measurements have been made for model and full size pulse jets, akin to those on World War II era V-1 "buzz bombs", although over audible frequencies [37-39].

Figure 5.39: Polar directivity of SPL for f=1.25 Hz signal at 8 m range.

Figure 5.40: Rectangular directivity of normalized pressure level for f=1.25 Hz signal at 8 m range.

98
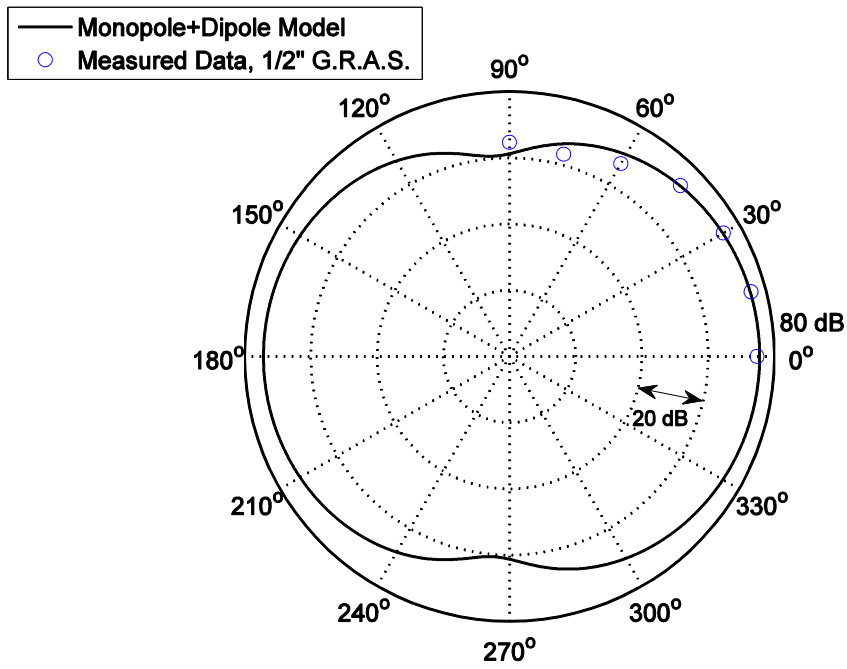
Figure 5.41: Polar directivity of SPL for f=2.5 Hz signal at 8 m range.
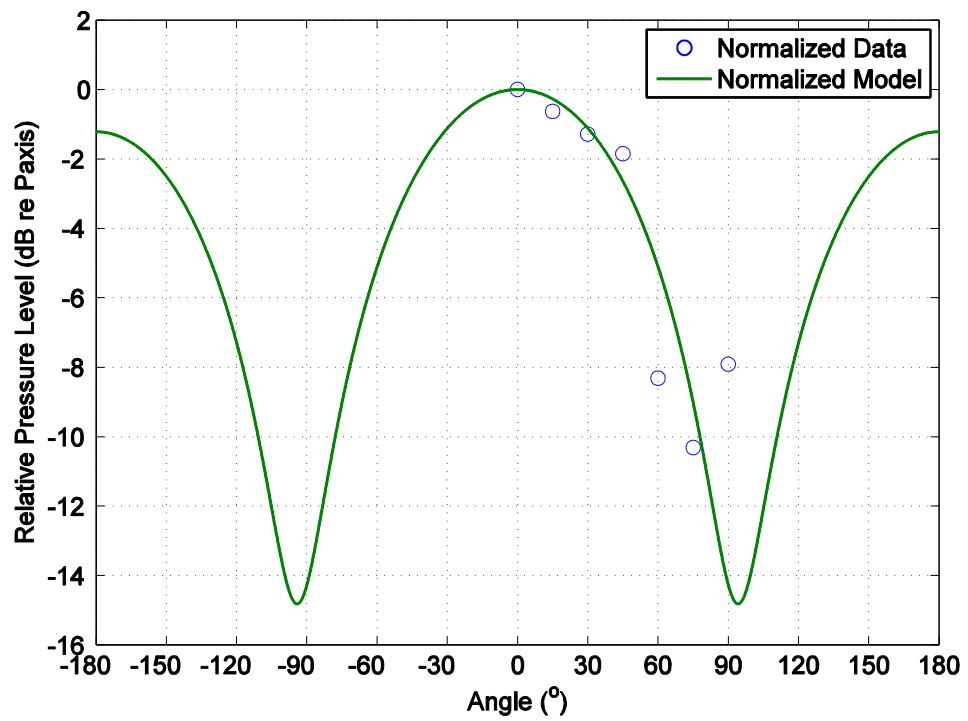
Figure 5.42: Rectangular directivity of normalized pressure level for f=2.5 Hz signal at 8 m range.

99
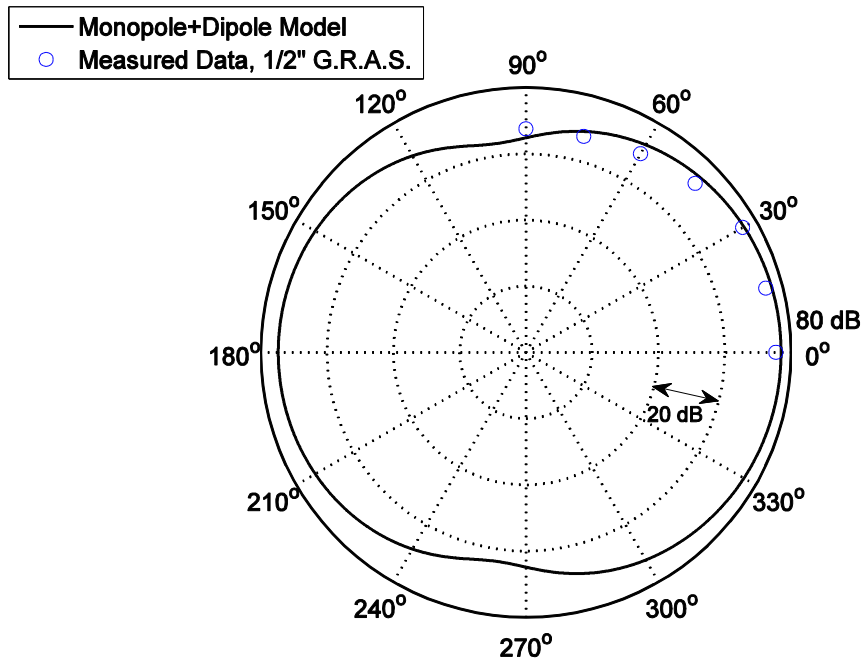
Figure 5.43: Polar directivity of SPL for f=3.7 Hz signal at 8 m range.
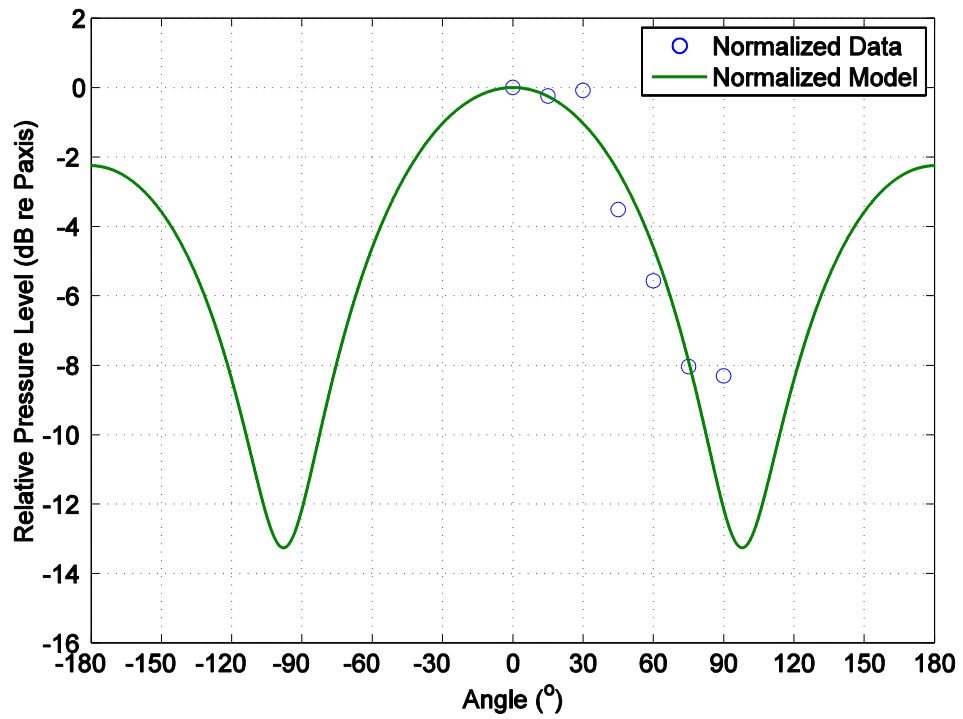
Figure 5.44: Rectangular directivity of normalized pressure level for f=3.7 Hz signal at 8 m range.
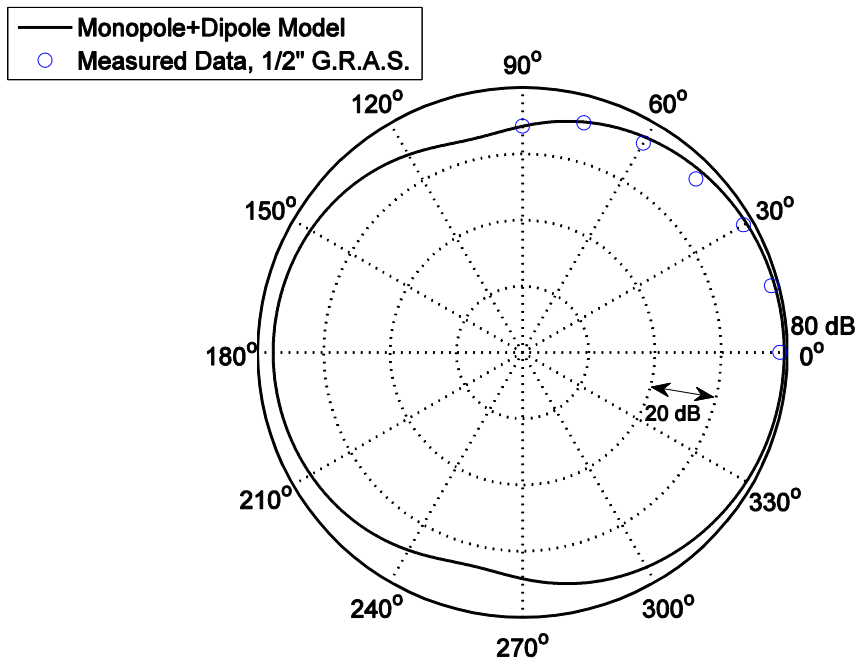
Figure 5.45: Polar directivity of SPL for f=5.4 Hz signal at 8 m range.
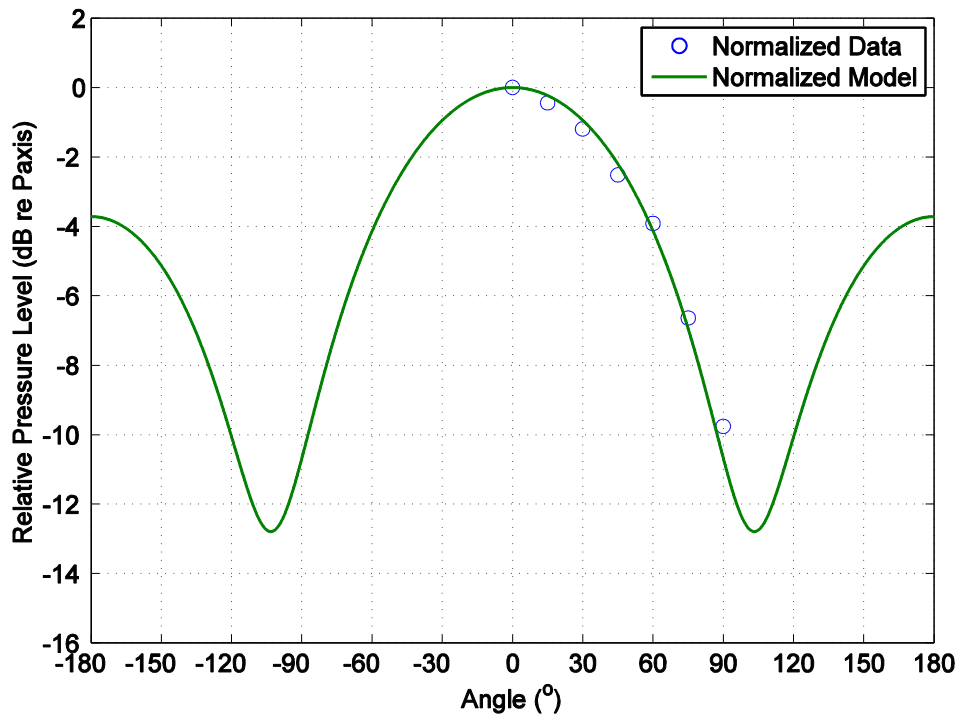
Figure 5.46: Rectangular directivity of normalized pressure level for f=5.4 Hz signal at 8 m range.

101

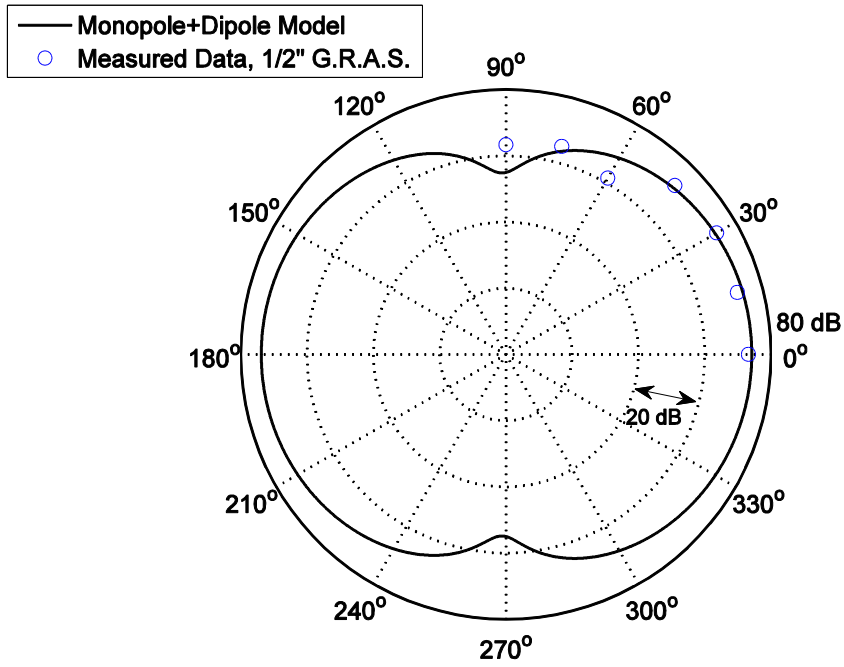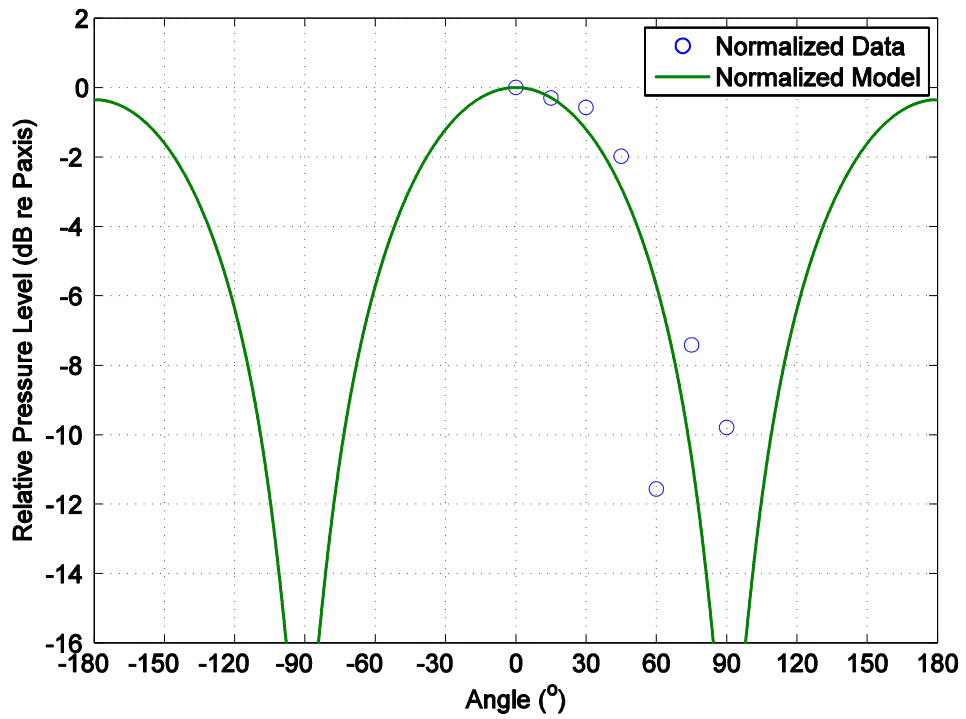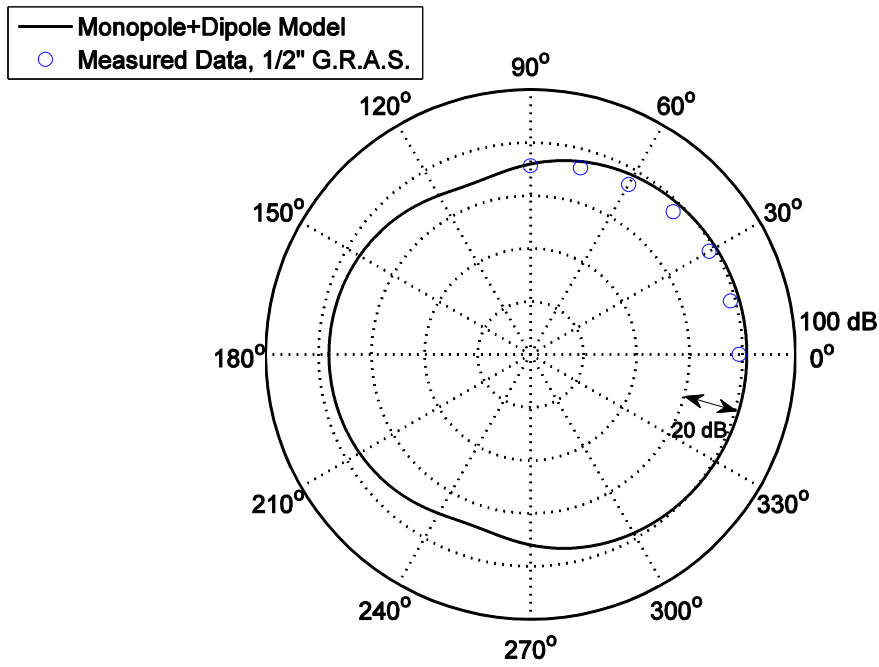**Figure 5.47: Polar directivity of SPL for f=8 Hz signal at 8 m range.**
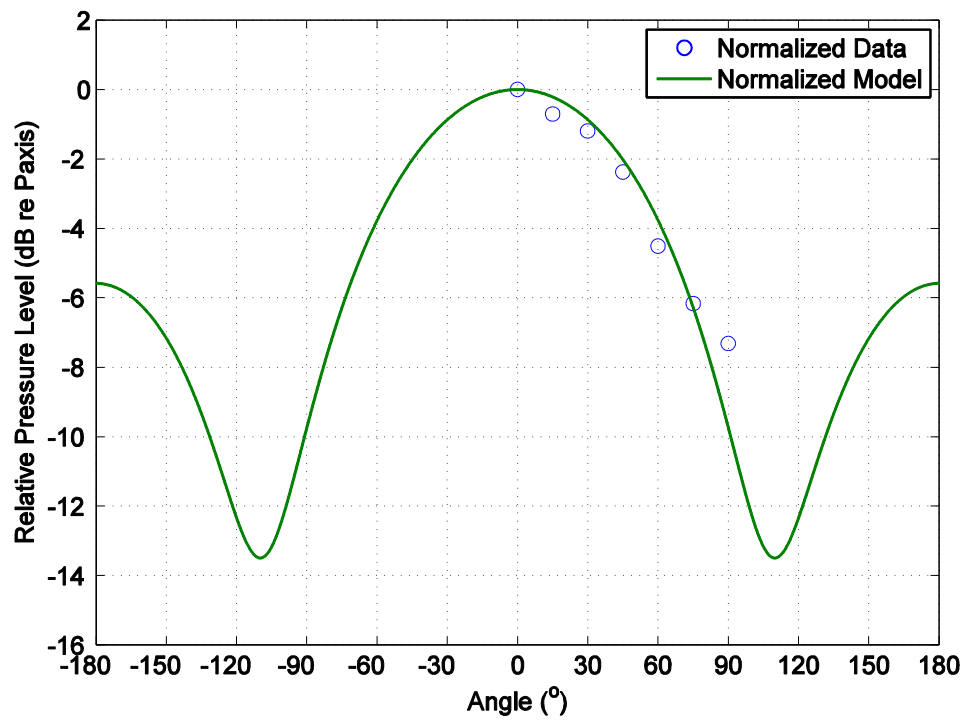
Figure 5.48: Rectangular directivity of normalized pressure level for f=8 Hz signal at 8 m range.

5.7.2 Full Azimuth Directivity Measurements

Full 360 degree directivity patterns were measured and are shown in Figs. 5.49-5.52. The measurements were made at 8 m and 16 m at a frequency of 8 Hz. The signals at all angles for the normalized plots were normalized by the on axis measurements made at 8 m, in order to remove minor changes in reservoir pressure as well as environmental influences such as wind, etc. The full 360 degree directivity patterns were not done for the lower frequencies, as the levels would be very difficult to consistently detect around the full circle, especially at farther ranges. Even at the highest frequency, 8 Hz, it was difficult to make measurements behind the source (θ=120°-240°) due to the decrease in infrasound pressure amplitude. For each of the plots, the theoretical model directivity of Equation (34) is shown with a solid line, while the measured data is shown with circles. The SPL values are plotted on polar plots, while the relative pressure levels are plotted on rectangular plots. The theoretical predictions match the data points well. The nulls do not match the data exactly, but it is probable that a myriad of experimental and environmental effects could alter the exact position and depth of these nulls. Regardless of the discrepancies, the theoretical model matches the data quite well.
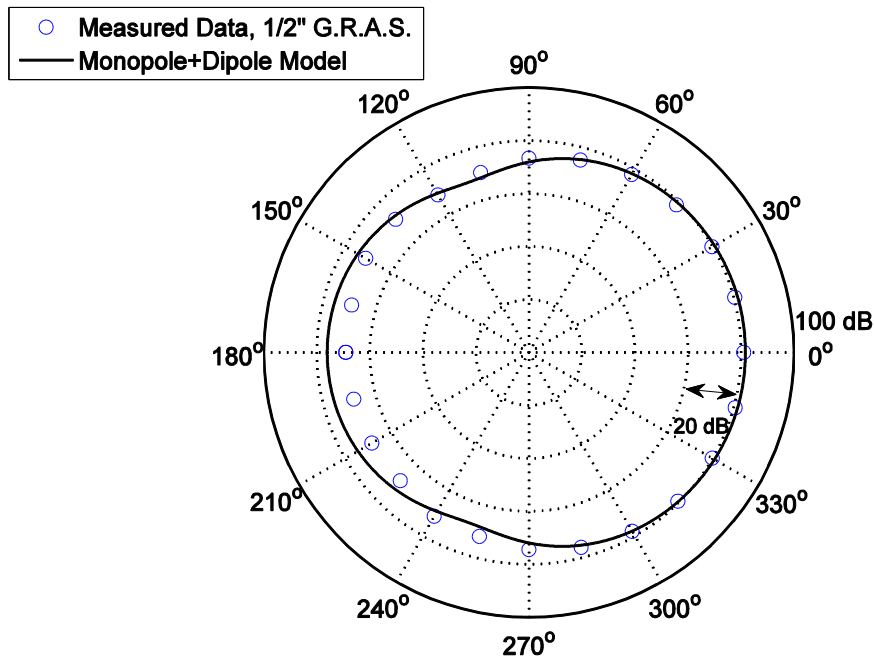
Figure 5.49: Complete 360° polar SPL directivity for f=8 Hz signal at r=8 m.
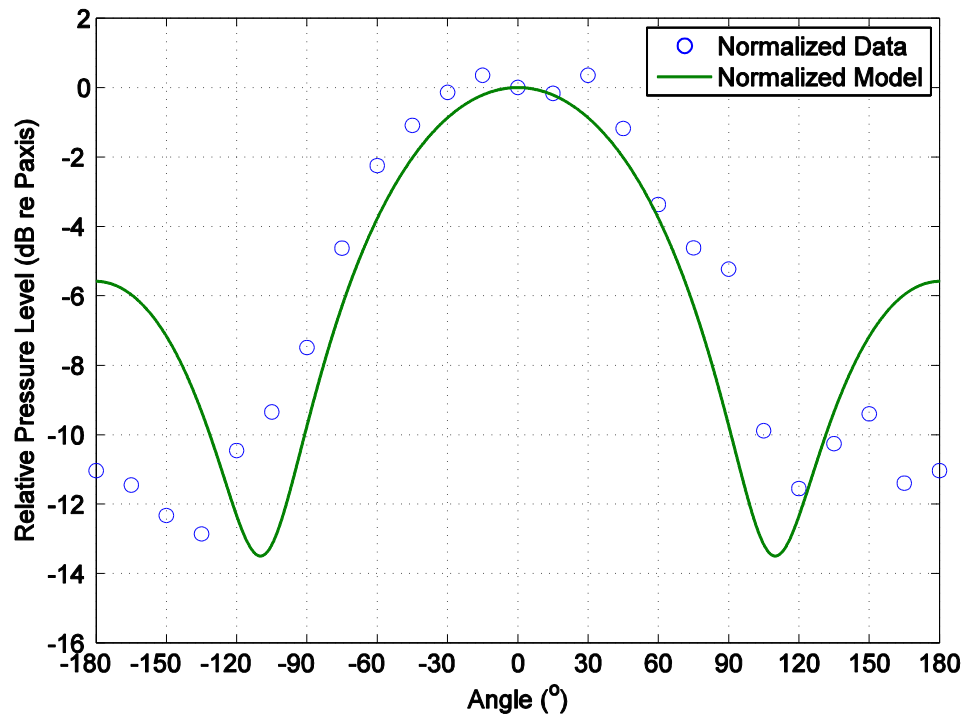
Figure 5.50: Rectangular directivity of normalized pressure level for f=8 Hz signal at r=8 m.

104
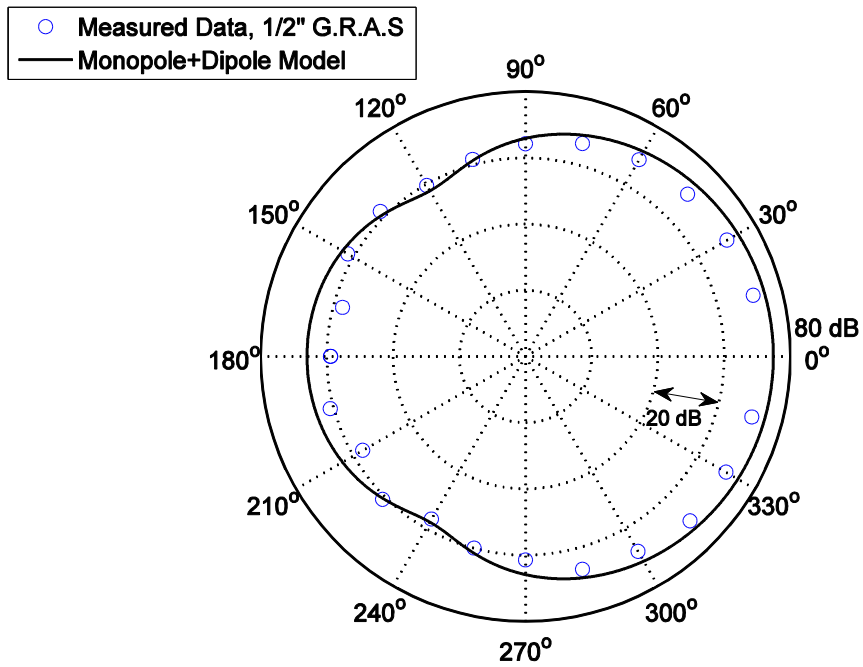
Figure 5.51: Complete 360° polar SPL directivity for f=8 Hz signal at r=16 m.
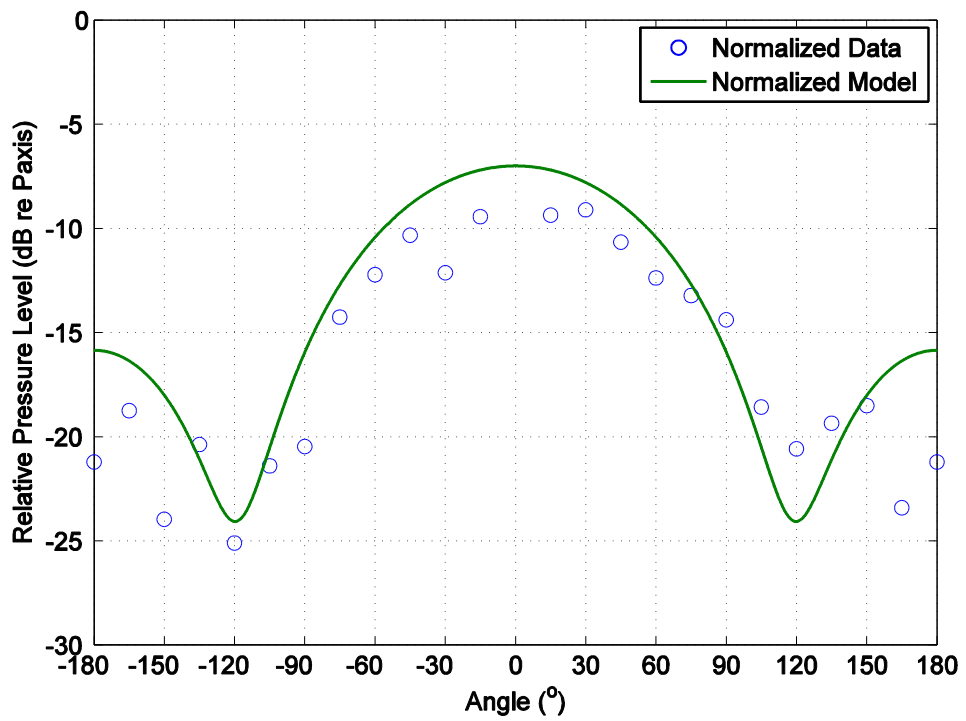
Figure 5.52: Rectangular directivity of normalized pressure level for f=8 Hz signal at r=16 m.

105

5.8 Jet Centerline Velocity Decay

The jet velocity measurements were measured from the exit of the jet outlet out to 0.413 m. The velocity measurements were made along the axis and were compared to the empirical formulas developments by Witze [29] and Lau [30,31]. The centerline jet decay and the empirical formulas are plotted in Fig. 5.53. It can be seen that the data closely matches the Lau empirical fit found in the literature for an empirical constant of $\alpha=1.2$ [30]. Minor discrepancies can be explained by the unfortunate flexibility of the infrasound generator stand. Due to the high speed of the jet exiting from the nozzle, a large amount of thrust is produced. This thrust acted upon the generator stand and caused it to deflect. This deflection caused the nozzle, and thus the jet, to move. This prevented the measurements from being exactly on the axis of the jet flow and thus reduced the measured stagnation pressure and velocity. However, the magnitudes of the measured values are still close to the empirical curve, and follow the trend nicely.
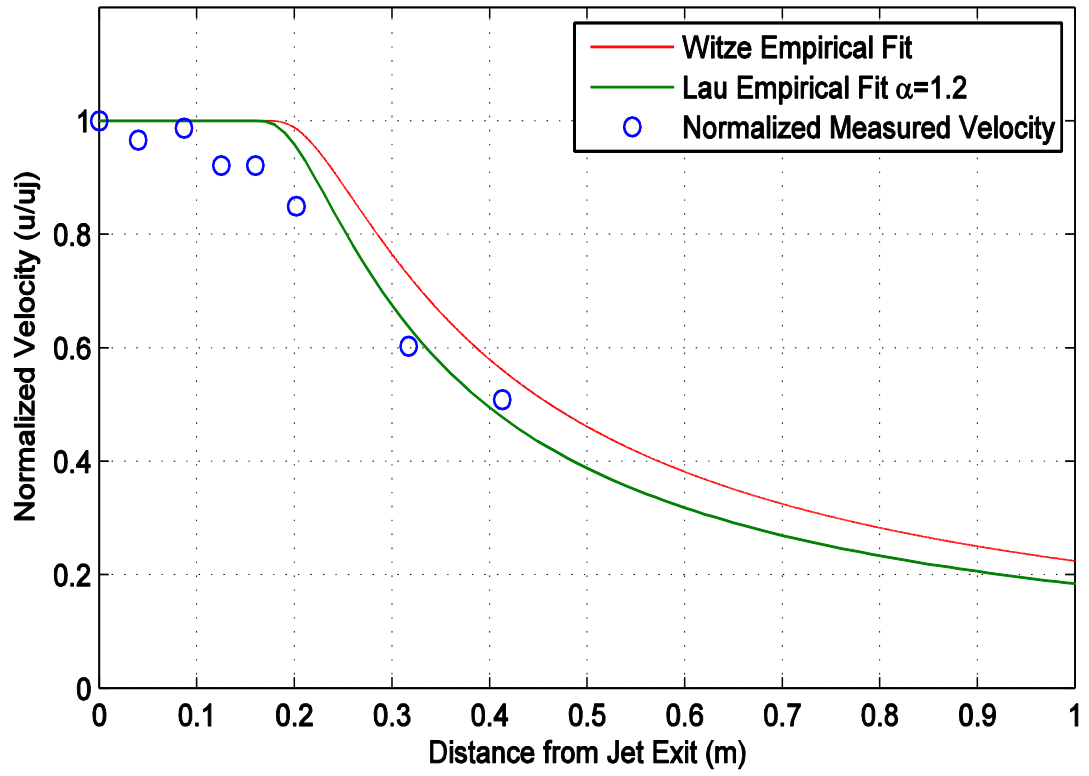
Figure 5.53: Jet centerline velocity decay.

Chapter 6

Discussion

This thesis examined the experimental development of a model infrasound generator employing the release of modulated compressed air into the atmosphere. The generator operated on the siren concept, where air was passed from a reservoir through a rotor/stator pair and into the atmosphere. A rotating ball valve modulated the air flow into to a triangular velocity emission that expanded and propagated into the atmosphere as a near sinusoidal infrasound wave. Although there may be several different end applications, the present development had in mind a system to eventually be used in calibration, testing, and research involving infrasound arrays deployed in the International Monitoring System (IMS), which is integral to the Comprehensive Nuclear Test Ban Treaty (CTBT) [15].

The source is constructed of a simple reservoir made from SCUBA tanks that stores the compressed air, a dc motor that rotates the modulator, which itself is a rotor/stator pair composed of a ball valve which serves to modulate the air flow in the context of a siren. These elements were assembled together to create the infrasound generator. A Pitot tube was attached to the outlet of the exit jet pipe to allow for the flow stagnation pressure to be measured and recorded, and a wind shielded microphone was deployed in the field on the ground to measure the output acoustic pressure. The source exit nozzle was configured in two orientations: with the output vertical, perpendicular to the ground, and with the output horizontal, parallel to the ground. By switching the

orientation of the jet nozzle from vertical to horizontal, the detected source level was increased by approximately 6 dB. The constructed source was as an experimental model that was developed in order to gain physical insight into how a source of this type generates infrasound. This assisted us in the development of a theoretical model.

The theoretical model that was developed allowed for a better understanding of the physics of this type of system, and allowed for predictions about the source level, propagation, frequency response, and directivity to be made. This theory was needed in order to understand and predict the sound pressure levels generated by this type of siren source, operating at infrasonic frequencies. Understanding the physics allows for scaled up systems to be designed and engineered to meet specific requirements. The theory was developed by physically observing the system (witnessing the rapid air injection into the atmosphere and the strong thrust forces produced), taking experimental data on both fluid flow and acoustic parameters, and comparing proposed models to the measured data. Observation of the system injecting air into the atmosphere and being subjected to a strong thrust force led to the development of an acoustic monopole (air injection) and dipole (thrust force) based theory. This theory allows us to predict the frequency response, propagation, and directivity characteristics of the system.

The source was described as a point monopole superimposed on a point dipole. When the exit jet nozzle is either vertical or horizontal, it is baffled against a rigid half space (the ground). The monopole source was caused by the time varying modulated volume velocity flowing out of the exit nozzle in the form of a high velocity jet. The dipole source was caused by the time varying reaction forces applied to the medium at

the exit nozzle, in response to the thrust caused by the jet. Theory and experiment were developed for both orientations of the exit nozzle: perpendicular to the ground in the vertical case, and parallel to the ground in the horizontal case. When the exit nozzle was vertical, the dipole pressure contribution at the microphone was negligible because the microphone was located near the null of the dipole directivity. Ground reflections were also a source of complications. When the exit nozzle was horizontal, the dipole contribution was of comparable strength to the monopole because the microphone was located near the maximum of the dipole directivity. Of course, the physical description is much more complicated at the closest ranges due to interactions between the aerodynamic nearfield flow and the microphones. The exit jet flow was supersonic, so careful considerations of the compressible fluid mechanics were made. The Rayleigh-Pitot tube formula was employed to calculate the fluid velocity from the Pitot tube, thus correcting for the bow shock that formed over the Pitot tube inserted into the supersonic outlet flow.

The frequency of the source can be controlled and varied to produce useful infrasound levels, given only that the system's drive motor can turn its modulator, a rotating ball valve, at the required angular velocity and that there is sufficient reservoir storage pressure. Moreover, the source strength can be increased by increasing the amount of airflow, through increasing the pressure and reservoir storage capacity, and increasing the ball valve size. This results in being able to scale up (or down) the size of the source, for a desired application, be it for increased source level or for different frequencies, including even lower infrasonic as well as higher audio frequency usage.

Five main experiments were performed in order to characterize the infrasound generator. These included propagation, frequency response, dependence on reservoir volume, directivity, and jet velocity measurements.

1) In propagation, it was found that for the <u>vertical</u> nozzle, the infrasound waves tend to spread spherically, especially at horizontal ranges of 8 meters and greater. For the <u>horizontal</u> nozzle, it was found that the waves typically spread spherically. While wind noise was noticeably present during the experiments, using electronic band pass filtering and mechanical wind shielding (see Figs. 1.3 and 1.4) effectively reduced the noise levels. Signals at the highest frequency (8 Hz) were easily detectable out to a range of 24 m for both vertical and horizontal orientation. Signals became increasingly difficult to detect at long range with decreasing frequency. Moreover, signals measured off axis for the horizontal nozzle orientation became more obscured by wind noise as the sound pressure level dropped with increasing azimuthal angle, due to the effectively "cardioid" directivity of the horizontal orientation in the forward direction.

2) The frequency response of the source was found to increase with frequency for both the vertical and horizontal orientations, and to be dependent on the reservoir storage pressure and drive frequency. Additionally, the frequency response was affected by the monopole and dipole source contributions, with the monopole source dominating the frequency response of the vertical orientation and the dipole source dominating the response for the horizontal orientation. The monopole source is proportional to the frequency and the volume velocity, whereas the dipole source is proportional to the frequency and the aerodynamic thrust force. Both the volume velocity and the thrust

force are dependent on the reservoir pressure. The "bleeding down" of the reservoir volume caused a noticeable rapid decrease in reservoir pressure at the lowest frequencies. This resulted in the volume velocity and thrust force having a lower peak amplitude at the lowest frequency. The frequency dependence of the system volume velocity and thrust force were measured, fitted with a curve fit, and used as approximate source strengths for the monopole (Equation (23)) and dipole (Equation (30) and Equation (33)) models. The reservoir bleed-down at low frequency resulted in the frequency response of the source deviating from the linear frequency dependence expected for constant source strength. The sound pressure level was found to increase with increasing frequency, asymptotically approaching linear frequency dependence at the farthest range (24 m).

3) Experiments that varied the reservoir volume showed that increasing the reservoir volume did not increase the peak source level, as the flow velocity is limited by the reservoir outlet pipe size (was "choked"), but instead allowed for a longer signal.

4) Directivity measurements were made for receivers placed on quarter circles on the ground at various frequencies, and for receivers placed on full circles on the ground at the highest frequency (8 Hz) and at two different ranges (8 and 16 m) . The source level is of course highest on axis, and measurements were made near or on axis for calibration and to ensure the greatest source strength and distance for the propagation measurements. Sound pressure levels were significantly lower in the region behind the source ($\theta=120^o$ to 240°) and were very difficult to detect when directly behind the source ($\theta=180^o$). The directivity pattern in the horizontal orientation had a cardioid shape due the combination of the monopole and dipole source. Directivity measurements in the vertical orientation

112

were not attempted due to measurement difficulties and to the lower SPL values compared to the horizontal orientation. It is expected that the directivity would be effectively omnidirectional due to the dipole having negligible contribution to the overall SPL at ranges of 8 m and greater in the vertical orientation.

5) The jet velocity was also measured using a Pitot tube positioned along the centerline of the jet and was found to follow empirical trends developed in the compressible turbulent jet literature. The jet velocity decreases with increasing range and approaches an x^{-1} velocity dependence asymptotically, where x is axial distance.

Finally, the infrasound source work discussed in this thesis led to the development of a larger scale system [40]. This scaled up system can be seen in Fig. 6.1. It was developed with two 500 gallon tanks pressurized by an industrial compressor up to 110 psi, with a number of control ball valves to remotely manage the airflow. Air is modulated with two synchronized rotating ball valves measuring $2''$ in diameter and vented to the atmosphere in two horizontal nozzles. These synchronized pulse jets create infrasonic tone burst in the frequency range of 0.25 Hz to 1.5 Hz. The system shown in Fig. 6.1 was developed to test the feasibility of using a portable infrasound generator for the calibration and tests of IMS receiver array stations. This development was reassuring in terms of the utility of this thesis work in that it transitioned basic engineering research into a tangible product, of potential use in IMS calibration applications.
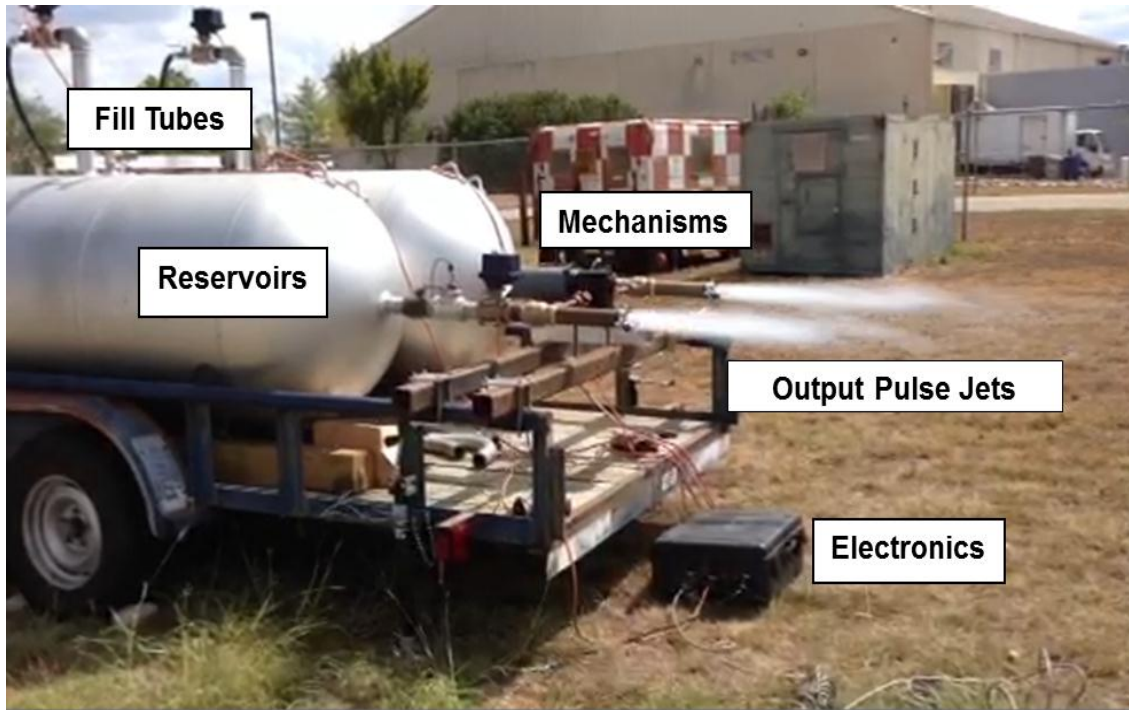
Figure 6.1: Large scale infrasound generator.

Chapter 7

Conclusions

A novel infrasound generator was developed and tested, and was physically explained through the development of a theoretical model for conceptually similar devices. This generator operated on the siren concept, but due to high, compressible flow velocities also possessed a dipole component, in contrast to prior sirens operating with laminar, incompressible flow. The generator was found to operate best in the horizontal configuration and was demonstrated out to a range of 32 meters at a frequency of 8 Hz with good signal to noise, using only moderate wind shielding, provided by cushions. The frequency range of the source was greater than 2 octaves, with a maximum generated frequency of 8 Hz and a minimum detected frequency of 1.25 Hz. SPL varied nonlinearly at low frequency, but reached a linear asymptote at the highest frequencies. Low frequency acoustic outputs were limited by the amount of compressed air in the reservoir. This is crucial for scaled up system design and calibration, as the system should be designed to have adequate compressed air to produce a desired signal length. This infrasound generator serves as a model for larger systems that are currently in development and testing. Combined with better wind noise protection techniques, it is possible that this or other larger scale sources could be used to calibrate an element (node) or a full array of an IMS station and could be effectively used in other areas of low frequency research. The model infrasound generator studied in the present thesis, shows

the feasibility of using modulated compressed air in conjunction with a ball valve siren, to create infrasound waves for calibration, testing, and research.

This experiment led to the development of a theoretical model that can be used to predict sound pressure level as a function of frequency, angle, and range. The theory utilizes the superposition of an acoustic monopole and dipole, baffled against a rigid half space, and was validated experimentally. The theoretical prediction of the sound pressure level matches the measured propagation curves, frequency response, and directivity well. It was found that the infrasound waves spread spherically. As frequency increases, the sound pressure level frequency dependence becomes linear. The sound pressure level is increased by as much as 6 dB when the jet nozzle is oriented horizontally rather than vertically. The sound pressure level is greatest on axis for a horizontal jet and decreases with increasing azimuthal angle, in a near-cardioid pattern, due to the superposition of monopole and dipole radiations. All of these effects are predicted by the theoretical model, which can be used to design and engineer sources operating on the siren principle that exert a strong, time-harmonic aerodynamic force onto the atmosphere.

In this work, it has been demonstrated that modulated compressed air vented into the atmosphere can serve as a feasible portable infrasound generator. When oriented vertically or horizontally, this infrasound generator can be modeled as the superposition of a monopole and a dipole. The directivity becomes increasingly "cardioid-like" with increasing frequency due to the increase in monopole source strength relative to the dipole. At the lowest frequencies for the horizontal orientation, the monopole component is dominated by the dipole component, but increases to comparable strength with

116

increasing frequency. This model matches experimental data to a high degree of accuracy and can be used to predict source levels and design new systems. The experiment provided useful experience in the development of a larger scale source to be used for calibration, testing, and research. The infrasound generator and accompanying theory described in this thesis, have successfully provided a novel means and model by which to create infrasonic waves with portable, non-resonant systems.

In addition to fitting a current need in the infrasound community, primarily for the calibration of IMS systems, the present work enables new areas of research to be explored in low frequency atmospheric acoustics. While other low frequency sources have been developed, it has been found that the present method of infrasound generation possesses unique advantages, due primarily to its simplicity and it's relatively small size, made possible by not using any resonant features.

Appendix A

Bruel & Kjaer Microphone Specifications

Bruel & Kjaer^{TM} Type 4144 1″ Microphone

	Sensitivity	Cartridge Capacitance	Frequency Range	Lower Limiting Frequency
Type 4144	114.6 mV/Pa	54.4 pF	2.6-8000 Hz	1.4 Hz

Table A1: Specifications for B&K Type 4144.

Bruel & Kjaer^{TM} Type 4193-L-004 ½″ Microphone

	Sensitivity	Cartridge Capacitance	Frequency Range	Lower Limiting Frequency
Type 4193-L-004	2.19 mV/Pa	19.2 pF	0.07-20000 Hz	0.07 Hz

Table A2: Specifications for B&K Type 4193-L-004.

Appendix B

G.R.A.S. Microphone Specifications

G.R.A.S. [TM] Type 40AZ ½″ Microphone #1

	Sensitivity	Cartridge Capacitance	Frequency Range	Lower Limiting Frequency
Type 40AZ	47.77 mV/Pa	20 pF	0.5-20000 Hz	-

Table B1: Specifications for G.R.A.S[TM] Type 40AZ #1.

G.R.A.S. [TM] Type 40AZ ½″ Microphone #2

	Sensitivity	Cartridge Capacitance	Frequency Range	Lower Limiting Frequency
Type 40AZ	56.78 mV/Pa	20 pF	0.5-20000 Hz	-

Table B2: Specifications for G.R.A.S[TM] Type 40AZ #2.
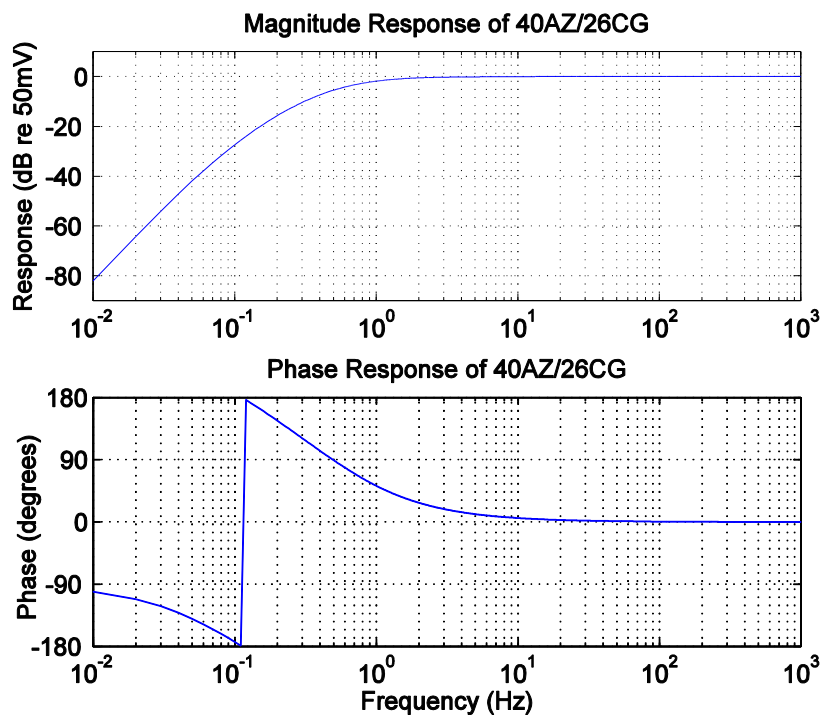
Figure B1: Magnitude and Phase response of 40AZ/26CG microphone/preamp combination.

119

Appendix C

PCB Piezotronics Pressure Sensor

PCB Model 102A02 ICP® Dynamic Pressure Sensor

	Sensitivity	Maximum Pressure	Discharge Time Constant	Rise Time
Model 102A02	7.3 mV/kPa	6900 kPa	≥ 1 sec	≤ 2 μsec

Table C1: Specifications for PCB ICP® Model 102A02.

Appendix D

Kavlico Pressure Sensor

Kavlico^{TM} P255 Pressure Sensor

	Null Pressure Voltage	Max Pressure Voltage	Pressure Range	Response Time
Model 102A02	0.50 Vdc	4.50 Vdc	0-200 PSIG	15 ms

Table D1: Specifications for Kavlico^{TM} P255.

Bibliography

1. L. G. Evers and H. W. Haak, "The characteristics of infrasound, its propagation and some early history," in *Infrasound Monitoring for Atmospheric Studies*, New York: Springer, 2009, Ch. 1, pp. 3-27.

2. H. E. Bass, et al., "Infrasound monitoring of atmospheric events," *Proceedings of the 25th Seismic Research Review—Nuclear Explosion Monitoring: Building the Knowledge Base*, 2003, pp. 577-586.

3. T. B. Gabrielson, "*In situ* calibration of atmospheric-infrasound sensors including the effects of wind-noise-reduction pipe systems," *The Journal of the Acoustical Society of America*, vol. 130, pp. 1154-1163, Sept., 2011.

4. E. von Muggenthaler, "Giraffe Helmholtz resonance," *Proceedings of Meetings on Acoustics*, Montreal, Canada, 2013.

5. K. B. Payne, W. R. Langbauer, Jr., and E. M. Thomas, "Infrasonic calls of the Asian elephant (Elephas maximus)," *Behavioral Ecology and Sociobiology*, vol. 18, pp.297-301, Feb. 1986.

6. H. von Helmholtz, *On the Sensations of Tone*, 4th ed. New York: Longmans, Green, and Company, 1912, pp. 11-12.

7. R. C. Jones, "A fifty horsepower siren," *The Journal of the Acoustical Society of America*, vol. 18, pp. 371-387, Oct., 1946.

8. C. H. Allen and I. Rudnick, "A powerful high frequency siren," *The Journal of the Acoustical Society of America*, vol. 19, pp. 857-865, Sept., 1947.

9. C. H. Allen and B. G. Watters, "Siren design for producing controlled wave forms at high intensities," *The Journal of the Acoustical Society of America*, vol. 31, no. 2, pp. 177-185, Feb., 1959.

10. J. M. Sabatier, "Acoustical characteristics of the mother of all speakers," *Sixth Internation Symposium on Long-Range Sound Propagation*, pp. 123-141, Dec., 1994.

11. K. Walker, M. Dzieciuch, M. Zumberge, and S. DeWolf, "A portable infrasonic sensor calibrator down to at least 8 Hz," *Proceedings of the 30th Monitoring Research Review*, Portsmouth, VA, 2008, pp. 902-911.

12. J. Park and J. Robertson, "A portable infrasound generator," *The Journal of the Acoustical Society of America*, vol. 125, pp. 148-151, April, 2009.

13. J. Park, M. Garcés, and B. Thigpen, "The rotary subwoofer: A controllable infrasound source," *The Journal of the Acoustical Society of America*, vol. 125, pp. 2006-2012, April, 2009.

14. K. T. Walker and M. A. H. Hedlin, "A review of wind-noise reduction methodologies," in *Infrasound Monitoring for Atmospheric Studies*, New York: Springer, 2009, Ch. 5, pp. 141-182.

15. A. Le Pichon, E. Blanc, and A. Hauchecorne, *Infrasound Monitoring for Atmospheric Studies*, New York: Springer, 2009.

16. J. R. Bowman, G. E. Baker, and M. Bahavar, "Ambient infrasound noise," *Geophysical research letters*, vol. 32, pp. 1-5, May, 2005.

17. F. B. Daniels, "Noise-reducing line microphone for frequencies below 1 cps," *The Journal of the Acoustical Society of America*, vol. 31, pp. 529-531, April, 1959.

18. B. Alcoverro and A. Le Pichon, "Design and optimization of a noise reduction system for infrasonic measurements using elements with low acoustic impedance," *The Journal of the Acoustical Society of America*, vol. 117, pp. 1717-1727, April, 2005.

19. M. A. Zumberge, J. Berger, M. A. H. Hedlin, E. Husmann, and S. Nooner, "An optical fiber infrasound sensor: A new lower limit on atmospheric pressure noise between 1 and 10 Hz," *The Journal of the Acoustical Society of America*, vol. 113, pp. 2474-2479, May, 2003.

20. F. D. Shields, "Low-frequency wind noise correlation in microphone arrays," *The Journal of the Acoustical Society of America*, vol. 117, pp. 3489-3496, June, 2005.

21. E. Herrin, G. G. Sorrells, P. Negraru, J. G. Swanson, P. Golden, C. Mulcahy, "Comparative evaluation of selected infrasound noise reduction methods," *Proceedings of the 23rd Seismic Research Review: Worldwide Monitoring of Nuclear Explosions*, Jackson Hole, WY, 2001, pp. 131-139.

22. M. A. H. Hedlin and R. Raspet, "Infrasonic wind-noise reduction by barriers and spatial filters," *The Journal of the Acoustical Society of America*, vol. 114, pp. 1379-1386, Sept., 2003.

23. From Wikipedia article: Ball valve.

24. Personal communication, A. Dacey Hussion of ARL:UT, Austin, May 2012.

25. M. J. Lighthill, "The Bakerian lecture, 1961. Sound generated aerodynamically," *Proceedings of the Royal Society of London. Series A. Mathematical and Physical Sciences*, vol. 267, pp. 147-182, May, 1962.

26. M. A. Theobald, "Experimental study of outdoor propagation of spherically spreading periodic acoustic waves of finite amplitude," M.S. thesis, Mech. Eng., University of Texas at Austin, Austin, TX, 1977.

27. J. D. Anderson, *Fundamentals of Aerodynamics*, 4th ed. New York: McGraw-Hill, 2007, pp. 485-629.

28. G. N. Abramovich, *The Theory of Turbulent Jets*, Cambridge, MA: MIT Press, 1963.

29. P. O. Witze, "Centerline velocity decay of compressible free jets," *AIAA Journal*, vol. 12, pp. 417-418, April, 1974.

30. J. C. Lau, "Effects of exit Mach number and temperature on mean-flow and turbulence characteristics in round jets," *Journal of Fluid Mechanics*, vol. 105, pp. 193-218, April, 1981.

31. J. C. Lau, P. J. Morris, and M. J. Fisher, "Measurements in subsonic and supersonic free jets using a laser velocimeter," *Journal of Fluid Mechanics*, vol. 93, pp. 1-27, July, 1979.

32. D. T. Blackstock, *Fundamentals of Physical Acoustics*, New York: John Wiley & Sons, 2000, Ch. 10, pp. 335-385.

33. Personal communication, P. J. Westervelt of Brown University, May 2013.

34. H. Lamb, *The Dynamic Theory of Sound*, London: Edward Arnold, 1910, pp. 240-241.

35. A. D. Pierce, *Acoustics: An Introduction to Its Physical Principles and Applications*, Melville, NY: Acoustical Society of America, 1989, pp. 167.

36. J. D. Anderson, *Modern Compressible Flow with Historical Perspective*, 3rd ed. New York: McGraw-Hill, 2003, pp. 216.

37. L. W. Lassiter, "Noise from intermittent jet engines and steady-flow jet engines with rough burning," National Advisory Committee for Aeronautics (subsequently NASA), Washington D.C., Rep. NACA-TN-2756, 1952.

38. S. K. Oleson, and K. U. Ingard, "Acoustic characteristics of model pulsed jets," *The Journal of the Acoustical Society of America*, vol. 29, pp. 1145-1146, Oct., 1957.

39. R. J. McQuillin, "The noise field of a pulse jet engine," M.S. thesis, Physics, Brown University, Providence, RI, 1959.

40. T. G. Muir, C. M. Slack, J. D. Gorhum, T. W. Hawkins, "Pneumatic infrasound source: Expanded model development and tests," *The Journal of the Acoustical Society of America*, vol. 134, Dec., 2013 (meeting abstract).

Note: It has come to the attention of the author that R. D. Costley, H. Diaz-Alvarez, M. H. McKenna, and A. M. Jordan have submitted a paper entitled, "Vibration and acoustic analysis of trussed railroad bridge under moving loads," to an archival journal (2014).

Vita

Justin Daniel Gorhum was born and raised in San Antonio, Texas where he attended Ronald Reagan High School. After graduating from High School in 2008, he enrolled in the University of Texas at Austin, majoring in aerospace engineering. In May 2012, he received a Bachelor of Science in Aerospace Engineering and enrolled in the graduate engineering program for mechanical engineering at the University of Texas the following fall. During the summer of 2011, the author participated in the Honors Scholar program at the Applied Research Laboratories, University of Texas at Austin, and worked there part time during the senior year of his undergraduate education. He continued working for the Applied Research Laboratories from that time until the completion of his Master's degree.

Permanent address: 3781 Beckwood

San Antonio, TX 78259

This thesis was typed by the author.